Modeling and Control of Unmanned Aerial Vehicle for Autonomous Navigation in Virtual Environments for Agriculture of Precision

Gabriel Oliveira Pimentel

Dissertation presented to the School of Technology and Management of Bragança to obtain the Master Degree in Electrical and Computer Engineering. Work developed under the Dual Degree Program between the Polytechnic Institute of Bragança (IPB) and the Federal Center for Technological Education of Minas Gerais (CEFET-MG).

Work oriented by:

Prof. PhD José Luís Sousa de Magalhães Lima

Prof. PhD Murillo Ferreira dos Santos

Bragança

2024

Modeling and Control of Unmanned Aerial Vehicle for Autonomous Navigation in Virtual Environments for Agriculture of Precision

Gabriel Oliveira Pimentel

Dissertation presented to the School of Technology and Management of Bragança to obtain the Master Degree in Electrical and Computer Engineering. Work developed under the Dual Degree Program between the Polytechnic Institute of Bragança (IPB) and the Federal Center for Technological Education of Minas Gerais (CEFET-MG).

Work oriented by:

Prof. PhD José Luís Sousa de Magalhães Lima

Prof. PhD Murillo Ferreira dos Santos

Bragança

2024

Dedication

I dedicate this work to my parents and my fiancée, who encouraged and supported my academic journey and helped make it possible for me to conclude this work. Without the help and encouragement of each one of you, this journey would not have been possible. In gratitude, I dedicate this dissertation to all of you.

Acknowledgement

For all their patience, help, and teachings during this journey, I would like to thank José Luís Sousa de Magalhães Lima and Murillo Ferreira dos Santos. Thank you for your guidance, which has been fundamental in enabling me to bring this work to a successful conclusion. Also, I would like to thank the National Council for Scientific and Technological Development (CNPq) for all support in the project.

I would like to thank my fiancée, Fernanda Rayol, who has been by my side throughout this journey. I am very grateful to her for her patience, understanding, support, and encouragement, and also for all the conversations we had, which have been helping me all the time, especially during the most difficult ones.

I would like to thank my friends Fernando Cosme, Filipe Lupatini, José Laert Portilho, and Werickson Fernandes, who have always been by my side, and Bairro Nobre 4.0 family, for all the support and moments we have spent together, for every moment of relaxation and encounters that have given me the energy to keep going throughout this journey.

I am deeply grateful to my parents, Márcio Guerra and Karla Oliveira, who taught me from an early age to value education and always seek more knowledge. I thank them for their encouragement, dedication, and all the efforts they made to the formation of me as a person. Thank you for everything you have done to make me who I am today. I would also like to express my gratitude to my sister, Marina Moreira, and my grandmother, Rizza Daniel, who have always been in my side.

Thanks to all the other members of my family and friends who have been by my side who have helped me grow and develop. Thank you for encouraging, helping and supporting me throughout my life.

Abstract

This works focuses on the modeling, control, and simulation of a over-actuated Unmanned Aerial Vehicle (UAV) prototype. This vehicle is a Hexacopter Tilt-Rotor (HTR) that 2 of the 6 actuators are independently tilted using servomotors, providing high maneuverability and reliability. This approach is predicted to maintain zero pitch throughout the trajectory and is expected to improve the aircraft's steering accuracy. This arrangement is particularly beneficial for Precision Agriculture (PA) applications where accurate monitoring and management of crops are critical. The enhanced maneuverability allows for precise navigation in complex vineyard environments, enabling the UAV to perform tasks such aerial imaging and crop health monitoring. The employed control topology consists of cascaded Proportional (P)-Proportional-Integral-Derivative (PID) controllers using the Successive Loop Closure (SLC) method on the five controlled Degrees of Freedoms (DoFs). Regarding the control allocation method, it is developed is an extension of Fast Control Allocation (FCA) technique. To validate this proposed approach, simulated results using Gazebo software and Robot Operating System (ROS) demonstrate that the aircraft achieves stability and maneuverability throughout different scenarios, achieving a maximum pitch of $\pm 1.5^{\circ}$, significantly improving PA practices. Furthermore, a comparison of the HTR with a traditional hexacopter validates the proposed approach.

Keywords: Unmanned Aerial Vehicle; Hexacopter; Over-Actuated UAV; Tilt-Rotor; Precision Agriculture

Resumo

Este trabalho tem como objetivo a modelagem, controle e simulação de um protótipo de Veículo Aéreo Não Tripulado (UAV) superatuado. Este veículo é um Hexacóptero Tilt-Rotor (HTR) em que 2 dos 6 atuadores são inclinados independentemente usando servomotores, proporcionando uma elevada manobrabilidade e estabilidade. Espera-se que esta abordagem mantenha uma arfagem em zero ao longo da trajetória e que melhore a precisão da direção da aeronave. Esta disposição é particularmente vantajosa para as aplicações da Agricultura de Precisão (PA), onde a monitorização e a gestão precisas das culturas são fundamentais. A capacidade de manobra melhorada permite uma navegação precisa em complexos campos de vinhas, permitindo que o UAV execute tarefas como imagens aéreas e o monitoramento do estado das culturas. A topologia de controle implementada consiste em controladores P-PID em cascata utilizando o método SLC nos cinco graus de liberdade (DoF) controlados. Relativamente ao método de alocação de controle, este é desenvolvido como uma extensão da técnica Alocação de Controle Rápida (FCA). Para validar a abordagem proposta, resultados simulados usando o *software* Gazebo e ROS demonstram que a aeronave alcança estabilidade e manobrabilidade em diferentes cenários, atingindo uma arfagem máxima de $\pm 1.5°$, melhorando significativamente as práticas de Agricultura de Precisão. Além disso, uma comparação do HTR com um hexacóptero tradicional valida a abordagem proposta.

Palavras-chave: Veículo Aéreo Não Tripulado; Hexacóptero; Superatuado; Tilt-Rotor; Agricultura da Precisão

Contents

List of Tables

List of Figures

Acronyms

AI Artificial Intelligence

CEFET-MG Federal Center for Technological Education of Minas Gerais

CEM Control Effectiveness Matrix

CG Center of Gravity

CNPq Council for Scientific and Technological Development

DoF Degrees of Freedom

FCA Fast Control Allocation

FTC Fault Tolerant Control

GPS Global Positioning System

HTR Hexacopter Tilt-Rotor

IoT Internet of Things

LOS Line of Sight

MGVRI Modified Green Red Vegetation index

ML Machine Learning

MPC Model Predictive Control

MSE Mean Squared Error

NDVI Normalized Difference Vegetation Index

NED North-East-Down

NN Neural Network

P Proportional

PA Precision Agriculture

PD Proportional-Derivative

PI Proportional-Integral

PID Proportional-Integral-Derivative

RCA Real Control Action

ROS Robot Operating System

SAN Soil Available Nutrients

SITL Software In The Loop

SLC Successive Loop Closure

SMC Sliding Mode Control

SP SetPoint

UAV Unmanned Aerial Vehicle

VCA Virtual Control Action

VRF Variable Rate Fertilisation

WP Waypoint

Chapter 1

Introduction

By definition, Unmanned Aerial Vehicle (UAV) is characterized by the absence of human presence on board its structure. In recent years, the use of UAVs is currently growing ([1]–[5]), boosted by their capacity to reach remote or dangerous areas, simplifying surveillance, capture high-resolution images, and the emergence of innovative computer technologies such as Artificial Intelligence (AI) and computer vision, mainly in the areas of surveillance, terrestrial mapping, and the military field [6].

Initially, inspired by radio-controlled model airplanes designed for operations in hard-to-reach areas, most UAV applications were originally motivated by military purposes. During wars, the use of UAVs expanded, with strategic reconnaissance becoming essential due to the rapid development of electronics and new technologies [7]. Due to their small size, high stealth, and lack of human presence, UAVs were more difficult to detect by enemy air defense systems and less susceptible to being hit by anti-aircraft systems. Therefore, the use of UAVs was interesting for operation in extreme conditions, allowing flights at lower altitudes with greater maneuverability to carry out challenging and dangerous tasks, such as surveillance, geographic reconnaissance, unmanned inspection, communications intercept, and mapping of enemy areas [8].

However, military use drove the increase in applications, resulting in its expansion into civilian use [9]. With technological advances in the civilian sector, UAVs, in particular with the miniaturization of their components, the evolution of navigation systems,

and the integration of sophisticated sensors, have been widely used for various purposes, such as aerial photography [10], power line inspection [11], [12], pollution monitoring [13], forest fire monitoring [14], rescue operations [15], disaster management [16], healthcare [17], traffic management [18], marine monitoring [19], and agricultural applications [20]. In other words, they are categorized into four major fields: environmental, security, communication, and monitoring applications [21].

Emerging trends, such as the full automation of UAVs, enabling large-scale autonomous operations and their integration with 5G networks, are making these vehicles increasingly integral to modern society [22]. By reducing operational risks and enhancing autonomous control, the UAV market has experienced continuous growth. According to a study published by the European Single Sky Air Traffic Management Research, the UAV sector is projected to reach an annual value of 10 billion euros by 2035 [23].

In this context, agriculture has emerged as one of the sectors that benefit the most from UAV technology [24]. With the increasing need to optimize agricultural and livestock production while minimizing waste and costs, PA has emerged as a key approach. This strategy aims to increase the efficiency of agricultural operations through precise monitoring and targeted intervention, enabling farmers to manage their crops more effectively and sustainably. Using advanced technologies, such as UAVs, to optimize agricultural production by performing a variety of tasks, including monitoring soil health, fertilizer application, and weather analysis [25], [26].

Regarding the UAV topologies, they are classified into three main categories: fixed wing (such as airplanes, which have high cruising speed and long autonomous operating capacity), rotary wing (such as helicopters and multi-rotors, which have high maneuverability), and hybrid (such as tiltrotors, balloons, and airships, which have high autonomy but are slower) [27]. Figure 1.1 provides a visual representation of these UAVs classifications:

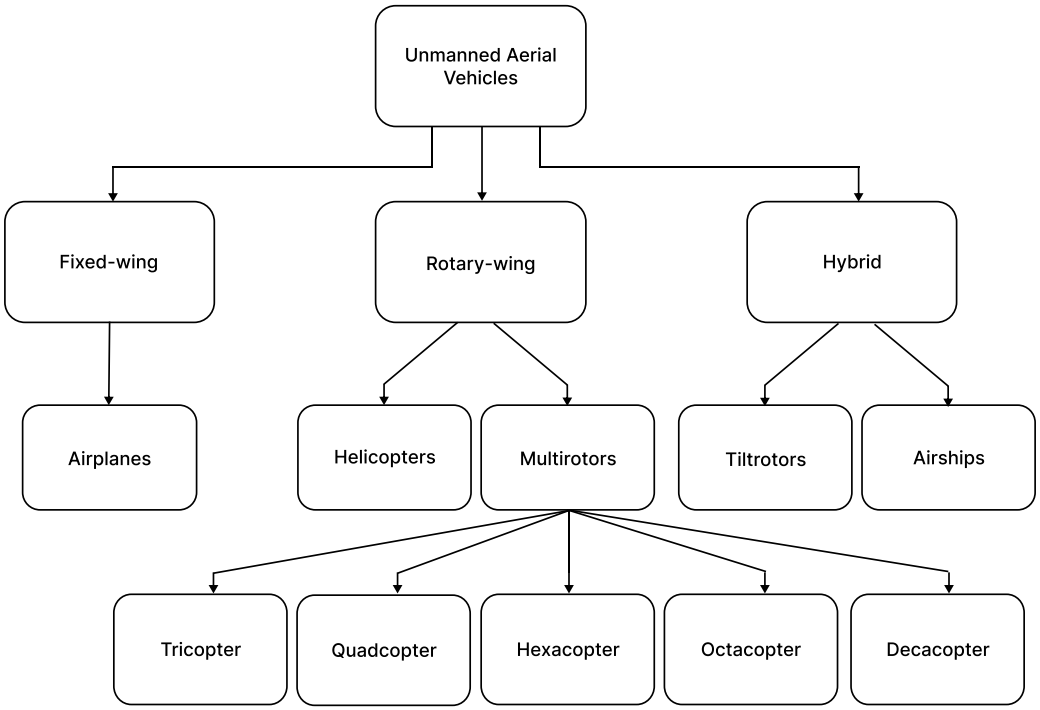

Figure 1.1: UAVs topologies

A notable topology among UAVs are tiltrotors. They harmonize rotary wing characteristics with fixed wings, providing the capacity for vertical takeoffs and landings. This gives them characteristics like helicopters, and fast and efficient horizontal flights, like airplanes. They are found in various designs, which differ according to the number and arrangement of rotors in their structure. The most common topologies include quadcopters with four rotors and hexacopters with six rotors. The diversity of existing tiltrotors offers a wide range of advantages in terms of performance, maneuverability, and operational efficiency [28].

UAVs have six DoF that influence their movements, including translations in the x, y, and z axes and rotations in the angles of roll (ϕ), pitch (θ), and yaw (ψ), which are used to describe the angular movements of the aircraft. For a clearer understanding, Figure 1.2 illustrates the respective angles:

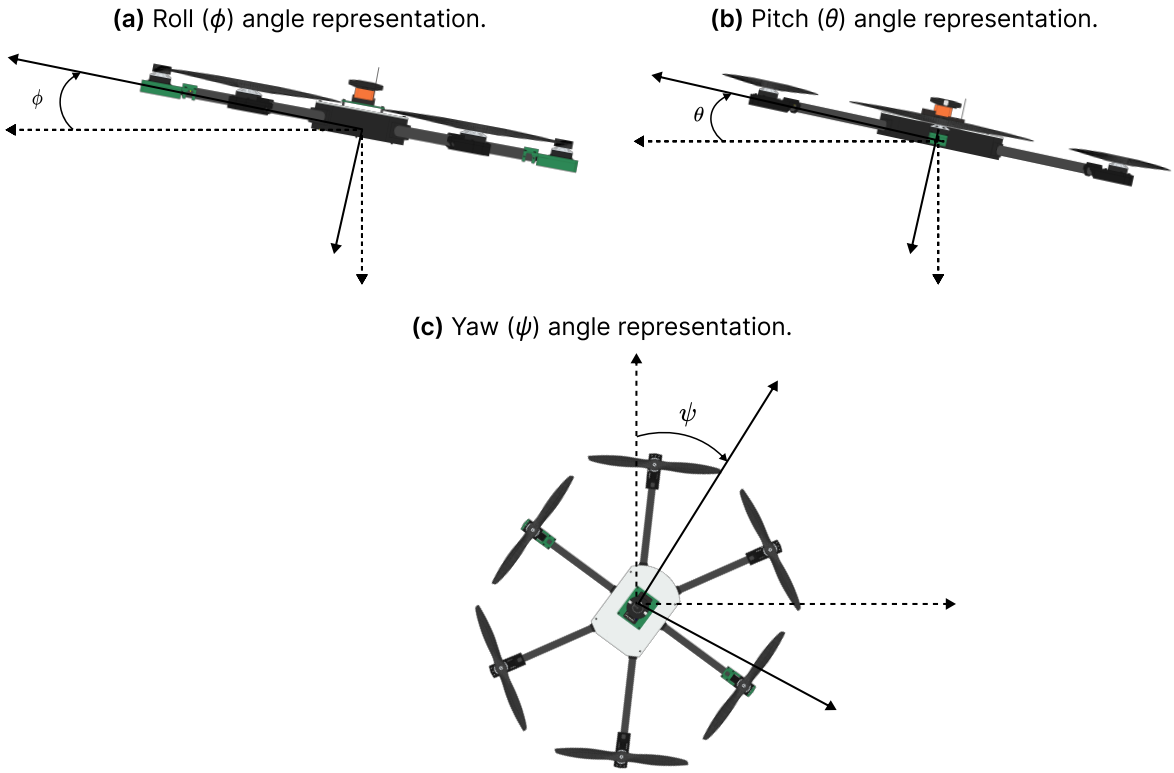

Figure 1.2: UAV state variables

As illustrated, the roll angle (Figure 1.2a) moves the vehicle side to the right or left. Pitch (Figure 1.2b) maneuvers move the UAV forward or backward. Yaw (Figure 1.2c) maneuvers change the UAV orientation without necessitating any translational movement of the vehicle.

In this context, the over-actuated HTR represents an advanced hybrid version of a hexacopter. Equipped with six motors, the HTR has a unique characteristic: two of its six actuators are independently tilted by the servomotors. This design provides faster flights and stability.

Figures 1.3a and 1.3b show the HTR over-actuated, with emphasis on the inclination of the 2 tiltrotors of the aircraft. Given this configuration, it has high maneuverability in forward dynamics considering the tilt of the motors, rather than pitching the aircraft

down/up. Moreover, the HTR has a high-speed capability for minor trajectory adjustments, and this configuration allows for faster yaw maneuvers if the tiltrotors are tilted in opposite directions:

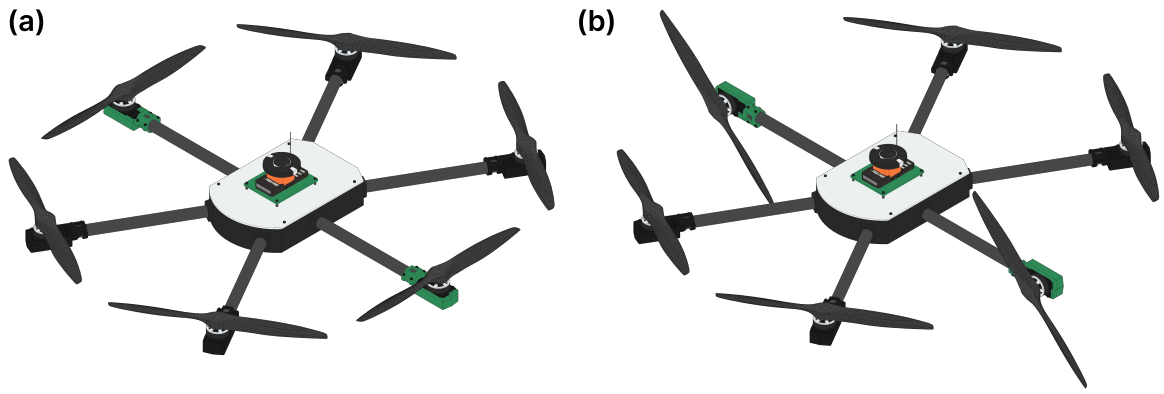

Figure 1.3: Illustration of the proposed HTR

In addition, by maintaining 90 degrees of pitch angle, the 2 tiltable motors are positioned horizontally, enabling efficient flight similar to a fixed-wing aircraft. In other words, the tilt-rotors allow the HTR to move forward or backward without the need to change the pitch angle, resulting in a more energy-efficient flight, considering the UAV expends less energy with drag forces.

Consequently, to ensure more effective flights, the manipulation of these DoFs is essential and can be achieved through control techniques, such as controlling the excitation of each actuator [29]. To achieve this objective, it is crucial to apply appropriate control strategies that ensure the aircraft's stability and control.

1.1 Motivation

This work is motivated by the increasing adoption of UAV in PA applications, where the demand for autonomous and precise systems is becoming increasingly critical [30],

[31]. Furthermore, the limited work on virtual simulations in this field highlights the importance of investigating these virtual environments. Achieving accuracy and efficiency is critical, requiring a robust control system capable of adapting to multiple conditions and being effectively embedded for extensive validation in virtual environments before real-world implementation.

To satisfy these demands, this work aims to contribute to advancing UAV technology by developing an over-actuated Hexacopter Tilt-Rotor that operates autonomously and effectively in virtual environments, using robust multilevel control to ensure reliable and sustainable results. This configuration enabling it to navigate efficiently in challenging PA scenarios, such as operating within plantations or over uneven terrains, while maintaining stability and accuracy. Also, this work is a continuation of the research previously presented in Pimentel et al. (2023) [32], resulted from an investigation project developed at Federal Center for Technological Education of Minas Gerais (CEFET-MG).

Furthermore, this work is under and significantly contributes to the international cooperation Project 442696/2023-0, titled "*Study of Cooperative and Autonomous Inspection in Plantations*", funded by CNPq. The objective of the project is to develop an innovative cooperative system involving robots and other autonomous agents to inspect fields using computer vision techniques, sensor integration, and intelligent cooperation.

1.2 Objectives

The main focus of this work is the modeling, control, and simulation of an over-actuated Hexacopter Tilt-Rotor within a simulated virtual environment using Gazebo software integrated with ROS. The developed HTR is an advanced hybrid version of a hexacopter, which has a unique characteristic: two of its six actuators are independently tilted by the servomotors, providing faster flights and stability in flight, as shown in Figure 1.3. This configuration allows high maneuverability in forward dynamics considering the tilt of the motors, and maintains zero pitch throughout the trajectory.

It is expected to ensure the autonomous and accurate execution of navigation tasks,

enabling the system to respond efficiently to various conditions and ensure successful integration into collaborative robotics scenarios. Furthermore, the specific objectives of this work are as follows:

- Implementation of the HTR in a simulated virtual environment in Gazebo software;
- Construction of a control system with P-PID multilevel topology;
- Apply an extended FCA control allocation method;
- Verification in simulations and comparative analysis between the HTR and the traditional hexacopter.

1.3 Methodology

The methodology adopted in this work was based on a set of objectives defined to achieve the proposed goals. The main steps included the following:

- **Research and literature review**: Research and reading of scientific articles, books, and other relevant materials in the field of mobile aerial robotics to establish a solid theoretical foundation in the UAV modeling, control, and simulation in virtual environments focused on PA;
- **Modeling of the HTR**: Obtain a representation of the HTR through a set of mathematical equations that describe the vehicle;
- **Controller modeling and tuning**: Modeling the P-PID controllers, considering the specified performance criteria;
- **Study and implementation in Gazebo**: Implementation of the HTR within a virtual environment using Gazebo;
- **Simulation results**: Perform simulations in Gazebo to evaluate the performance of the HTR in navigation scenarios and situations simulated in a PA environment.

1.4 Document Structure

Chapter 1 corresponds to the introduction, which outlines the foundational concepts necessary for a better understanding of the subject, including the various types and applications of UAVs. It also discusses the motivation, the methodology used, and the objectives to be achieved.

Chapter 2 presents the state of the art, including a literature review of the UAV's use in PA.

Chapter 3 presents the study of tools with the tools from the field of robotics used in the development of this work, such as ROS, virtual environments, and the PX4 Autopilot.

Chapter 4 details the kinematic and dynamic modeling of the HTR through mathematical equations. It also delineates the applied FCA technique, and the P-PID controller with the respective gains.

The simulation results obtained through the simulations conducted with the developed vehicle in Gazebo are presented in Chapter 5.

Finally, Chapter 6 addresses and discusses the conclusions reached in this work and suggests topics for possible future work.

Chapter 2

State of Art

This chapter provides context through a literature review of the main concepts addressed in this work. It also highlights recent projects that have employed UAVs across different contexts. Following this, the UAVs applications in agriculture are investigated in more detail, the main challenges and limitations associated with their use in this field are presented. Finally, recent works on over-actuated UAVs are discussed.

UAV has revolutionized various fields by providing innovative solutions to complex challenges. With the extensive expansion of technological resources, UAVs have emerged as crucial robotic tools used in diverse research fields, such as agriculture [33], infrastructure [34], logistics [35], and collaborative robotics [28].

Various UAV can be seen in the literature. As in the work presented by Yeom and Cho (2019), which discusses the UAV used for the detection and tracking of moving pedestrians, highlighting the potential of these vehicles in this type of mission. In their study, the experimental results show an average detection rate of 96.5%, highlighting the high accuracy in detecting and tracking targets, as well as confirming the efficiency of UAVs for people safety applications in areas with large crowds [36].

Xu, Li, Zhou, *et al.* (2022) dealt with UAV for automatic transmission line inspection, which overcomes the limitations of existing systems that adopt manual control and follow predefined paths, improving efficiency and reducing inspection costs by generating real-time guidance information. The experimental results, divided into four data sets,

demonstrate the effectiveness and robustness of the real-time motion planning strategy and the proposed system [37].

Similarly, the study presented by Calamoneri, Corò, and Mancini (2022) showed the use of a fleet of UAVs to support rescue operations after earthquakes and to guide rescue teams. Cooperation between UAVs allows the search for possible survivors to be faster and more effective. Simulations showed that the system works efficiently in the proposed scenarios. The main advantages of this model over current civil defense solutions include the elimination of the need for human operators and the ability of the UAVs to make decisions based on the information detected and prioritize critical locations, such as buildings at high risk of fire or health institutions [38].

The research by Olivatto, Inguaggiato, and Stanganini (2023) investigates the application of images obtained by UAVs for urban mapping and impact assessment in an irregular settlement in Brazil. Considering the limited financial context of some cities, where traditional remote sensing methods can be expensive, and with the regularization of irregular urban occupations in the country, which requires detailed and specific surveys. The study showed that the use of UAV images made it possible to create models that met the requirements of regularization and were effective in identifying the impacts on the environment and society, including deforestation, soil erosion, the irregular disposal of waste and failure to maintain basic infrastructures. The use of UAV proved to be an efficient and cost-effective alternative to traditional aerial surveys and high-resolution satellite images [39].

The study conducted by Gailler, Labazuy, Régis, *et al.* (2021) shows the use of UAVs for volcano monitoring, highlighting their importance for studying volcanoes and improving efficiency in monitoring volcanic activity. The integration of terrestrial and satellite measurements has been improved on an intermediate scale due to the measurements made by these vehicles. In addition to visible and infrared measurements, UAVs can perform geophysical measurements for more in-depth studies. The results of the comparison between simultaneous UAVs and terrestrial surveys are presented, demonstrating that low-altitude measurements are particularly relevant for accurate imaging of magnetic

anomalies and their variation over time in a volcanic context. The presented evidence validates the efficacy and feasibility of UAVs use for continuous volcano monitoring [40].

With this, these examples demonstrate the versatility and importance of UAVs in various fields, driven by technological advances and their ability to address complex challenges with efficiency and precision. The studies discussed highlight the adaptability of UAVs to tasks such as surveillance, inspection, disaster management, urban mapping, and environmental monitoring, showing their potential to revolutionize traditional methods in these areas. These insights are fundamental to understanding their transformative role in PAs, where the need for accurate, autonomous, and efficient systems is equally critical.

2.1 UAV in Precision Agriculture

Over the past few years, there have been significant remarkable advances in agriculture, most notably with the introduction of PA. This evolving field introduced innovative ways to improve crop productivity. It incorporates advanced technologies such as sensors and data analysis, allowing farmers to make more informed decisions and manage their land with greater accuracy [41]. Since its adoption, PA has shown considerable potential to revolutionize conventional farming practices, including crop monitoring and mapping.

Furthermore, emerging technologies such as the Internet of Things (IoT), AI, and Machine Learning (ML) have emerged as promising tools in the context of PA, providing significant improvements in efficiency and production. Various IoT-based systems have been developed, employing cloud computing, wireless sensor networks, big data analysis, and machine learning to perform intelligent agricultural practices [42]–[50]. These practices not only enhance productivity but also promote soil health, conserve water, and support biodiversity, ensuring the long-term sustainability of agricultural systems [51].

Despite the benefits of PA, it faces challenges in managing and analyzing the vast amount of data required for effective decision-making. In this context, UAVs serve as valuable tools for acquiring high-quality data efficiently, which can then be processed and analyzed to generate actionable insights. One promising approach to address these

challenges is the use of UAVs, which offers advantages such as low cost, efficiency, speed, and mobility for data collection and monitoring of crop conditions. Equipped with various sensors, including multi-spectral and thermal cameras, UAVs can capture detailed images of crops. These images are then processed to provide valuable information regarding crop health, growth, and yield, enabling the coverage of large areas quickly and accurately, reducing significantly the need for manual data collection and analysis, saving time and resources [52].

With the ability to quickly inspect large areas, UAVs monitor crops more accurately, regularly, and cost-effectively, providing high-quality data and enabling wasteful or unproductive practices to be identified and eliminated. These vehicles can fly at specific altitudes and angles, ensuring detailed and consistent images. Moreover, UAVs offers a continuous record of crop health over time, valuable for analysis, research, and even insurance claims in the event of losses due to disease or extreme weather conditions. Another key advantage is their capacity to access areas that are difficult to access by traditional methods, such as mountainous terrain, dense vegetation, or large fields, allowing comprehensive monitoring over the entire agriculture field [53].

By incorporating UAVs equipped with onboard computers and frequent communication with a ground station, producers have the advantage of receiving frequent updates and being instantly informed about the health of the crop within pre-defined limits. This allows them to identify areas that need intervention accurately. Consequently, the main areas of application for UAVs in agriculture are described as follows [54]:

- Aerial spraying and mapping;
- Water stress analysis;
- Irrigation management;
- Pest management;
- Vegetation health and growth monitoring;

- Yield estimation;
- Soil monitoring;
- Weed mapping and management.

Given this promising scenario, several studies have explored the use of UAVs in PA. Zou, Chen, Zhang, *et al.* (2021) explored an innovative solution to assess the density of weeds in agricultural fields using quadcopter images and a modified U-Net model. The research was conducted in an experimental marigold field, where images were captured at the seedling stage, allowing the identification of different weed species, such as green grass and yerba mate. The study focused on semantic segmentation of the images using convolutional neural networks, which demonstrated superior feature extraction capabilities compared to traditional methods based on manual definitions. With an accuracy of 93.5% and a determination coefficient of 0.94 compared to manual measurements, the study showed significant results in segmenting and mapping the density of the weeds, contributing to herbicide management and cost reduction in agriculture. However, the study also has limitations, such as data collection being limited to a single crop type and the need to diversify weed species to increase the robustness and adaptability of the model in different agricultural contexts [55].

In another study, Meng and Cheng (2020) explored the application of an octocopter for soil monitoring. The study integrates modified remote sensing data to accurately estimate Soil Available Nutrientss (SANs) at the field scale. However, the low spatial resolution of typical satellite imagery posed a challenge for accurate SAN estimation at the sub-field level, which is critical for effective Variable Rate Fertilisation (VRF). To address this, the researchers used multispectral imagery from UAVs to replace satellite data to improve spatial resolution. Moreover, their UAV improved the accuracy of SAN estimation at the subfield level. The results demonstrated the potential UAVs in soil monitoring, providing a more accurate tool to optimize fertilization strategies and support sustainable agricultural practices [56].

As reported by Kazemi and Ghanbari Parmehr (2022), the study investigates the use of quadcopter for monitoring rice crop growth by evaluating RGB vegetation indices as a cost-effective alternative to the more expensive Normalized Difference Vegetation Index (NDVI) derived from multispectral sensors. The study shows that UAVs, with their high spatial-temporal resolution, can effectively reduce monitoring costs while still providing valuable data. Among the RGB indices tested, the Modified Green Red Vegetation index (MGVRI) index demonstrated the strongest correlation with NDVI, indicating its potential for accurate crop monitoring and biomass prediction. However, other indices showed lower correlations and higher error rates, suggesting limitations in their use under certain conditions. Despite these challenges, the study concludes that RGB indices derived from UAV images can be a viable tool for crop management, particularly when multispectral data is unavailable, though their effectiveness may vary based on external factors such as lighting conditions [57].

In studies focusing on yield estimation with UAVs, two distinct approaches demonstrate the potential of technology to improve agricultural decision-making. First, Apolo-Apolo, Martínez-Guanter, Egea, *et al.* (2020) developed a system to automate image processing methodology for citrus yield estimation, employing quadcopter images and deep learning techniques. The results demonstrated the potential use of UAV for yield estimation [58]. In another study, Feng, Zhou, Vories, *et al.* (2020) equipped an UAV with infrared thermal cameras to estimate cotton yield by analyzing images from different stages of growth. The study concluded that images from the UAV are highly effective for estimating cotton yield, particularly when they are captured during critical growth stages such as flowering, which provide the most relevant data for accurate yield predictions [59].

The research detailed by Shi, Du, Liu, *et al.* (2024) investigated the efficacy of UAVs for pesticide application in tobacco pest management, focusing on how varying flight parameters affect spray performance. Conducting three field experiments at different stages of tobacco growth, from rosette to maturation, the researchers systematically assessed the effects of flight height, speed, and application volume on spray efficacy. The study identified optimal parameters for each growth stage, adjusting factors such as flight speed,

height, and liquid volume to maximize efficiency. During different stages of growth, these parameters were fine-tuned to improve pest control. The findings also showed that UAV spraying achieved better droplet deposition on both sides of the tobacco leaves compared to traditional methods, emphasizing the importance of tailoring UAV spraying parameters to specific growth stages for enhanced precision and efficiency [60].

In the work presented by Guo, Huang, Dong, *et al.* (2021), the use of a quadcopter equipped with hyperspectral sensors was explored to monitor wheat yellow rust at the field scale. The research focused on using hyperspectral images to analyze features such as vegetation indices and texture, aiming to develop regression models for monitoring disease progression at various infection stages. Different image resolutions were evaluated to understand their effect on the accuracy of disease detection. The study found that models based on vegetation indices were particularly effective during mid-infection stages, while texture-based models showed strong performance during both mid- and late-infection stages. The study results concluded that UAV hyperspectral images are highly effective in monitoring wheat yellow rust, enabling valuable insights for disease management and early detection [61].

Besides these applications, another agricultural use of UAVs is irrigation management. Risal, Niu, Landivar-Scott, *et al.* (2024) discussed the use of a quadcopter to enhance irrigation management in the Texas High Plains, a major cotton-producing region facing critical water shortages. They performed the tests In Lubbock, Texas, and the research aimed to improve irrigation scheduling by integrating high-resolution UAV images with soil moisture and canopy temperature sensors. The study found that the measurements were strongly correlated with cotton yield and fiber quality, revealing significant effects of water stress on crop growth. Specifically, the research demonstrated that quadcopter measurements could be effectively used to estimate crop water demand, with a regression model showing an accuracy value of up to 0.68. This approach could significantly improve irrigation efficiency by providing more accurate data, highlighting the potential of UAV technology to address water scarcity issues and optimize irrigation practices in water-limited regions [62].

For the analysis of water stress, Kumar, S, N, *et al.* (2020) investigated the use of a quadcopter to automate the monitoring of crop health, with a specific focus on water-stressed areas in maize fields. The study recognizes the current demand for more effective solutions, as agronomic inputs such as water, nutrients, and fertilizer are critical to crop health and yield, and traditional methods are labor-intensive and prone to inaccuracies. A framework utilizing convolutional neural networks was developed to differentiate between stressed and healthy areas in maize crops. The results demonstrated high precision in both the training and test datasets, showcasing the effectiveness of UAVs in enhancing the accuracy and efficiency of crop health monitoring. This approach highlights that the use of the quadcopter significantly increases the accuracy and efficiency of crop health monitoring, providing a valuable tool for farmers [63].

The study, outlined by Wang, Ma, Chen, *et al.* (2023), evaluates the potential of UAV for aerial spraying. The research investigated quadcopter spraying on fields with varying leaf area index values and operating parameters, showing that a higher index reduces chemical coverage. At a flight speed of 1.5m/s, the quadcopter achieved the best droplet penetration but a greater soil loss, while altitudes higher than 11.09 m and speeds higher than 2.5m/s degraded the overall deposition efficiency. In addition, increasing the flight speed resulted in a double of the drift distance. The results emphasize the need to consider operational parameters such as altitude and speed to optimize UAV applications [64].

In another study, Meinen and Robinson (2020) investigated the effectiveness of using quadcopter data for automated mapping of rill networks, demonstrating the quadcopter potential for monitoring field-scale erosion processes such as rill and gully erosion. The study showed that UAV data, captured in a single acquisition, offers a detailed and comprehensive view of field morphology, facilitating the mapping and monitoring of erosion with high accuracy. Two automated mapping techniques were evaluated, and both methods relied on handcrafted terrain properties for training, showcasing the quadcopter's capability to provide rich 3D data beyond simple transects. In general, the study underscores the UAVs significant role in advancing the automated mapping of rill erosion [65].

In addition, viticulture (a field of PA where monitoring vine health and yield is essential for vineyard management) has greatly benefited from adopting UAVs. Authors López-Granados, Torres-Sánchez, Jiménez-Brenes, *et al.* (2020) equipped a quadcopter model MD4-1000 with a digital camera was used to acquire high-resolution images from four vineyards, generating point clouds to analyze each vine and measure woody crop canopies. Two approaches were tested: the first aimed to detect canopy management by comparing vine dimensions, and the second focused on determining whether post-treatment data could identify the management operations. The results demonstrated the success of the first approach, where canopy management interventions were effectively detected. In the second approach, significant differences in vine dimensions were observed after the treatments, and shoot trimming was easily and accurately identified. Their study showed the capability of UAV technology combined with automated image analysis for precise monitoring [66].

Another significant study from Ferro, Sørensen, and Catania (2024) compared different computer vision methods for detecting vine canopies using multispectral images captured by a quadcopter. They showed that the multispectral image analysis technologies captured by UAVs represent an additional asset for the comprehensive monitoring and prediction of vineyard vegetation conditions [67]. Moreover, Pádua, Matese, Di Gennaro, *et al.* (2022) explores vineyard classification using the OBIA (Object-Based Image Analysis) technique on data obtained by two UAVs: a quadcopter and a hexacopter. The results presented that data acquired from different sensors are suitable to be used in the vineyard classification process [68].

2.2 Challenges and Limitations of UAVs in PA

UAVs have a significant potential for PA. However, several challenges and limitations must be addressed to maximize their potential. The study by Reddy Maddikunta, Hakak, Alazab, *et al.* (2021) [69] highlights some challenges:

- **Regulation**: Regulation is a major barrier, as many countries lack clear guidelines

for UAVs in agriculture, complicating the integration of this technology into the sector;

- **Network**: Network availability is crucial, as transferring data collected by UAVs to cloud platforms necessitates a strong and stable internet connection, which is not always available in rural areas;
- **Data storage**: Data storage is another important challenge due to the limited storage capacity of UAVs and the need for dependable internet connections for cloud-based solutions;
- **Security and privacy**: Security and privacy concerns are critical issues, as UAVs are susceptible to cyber-attacks, and there are privacy concerns when capturing images;
- **Energy efficiency**: Energy efficiency remains a limitation, as most UAVs have a limited flight time, typically under one hour, which may not be enough for covering large agricultural areas;
- **User acceptance**: User acceptance of UAV technology is a challenge due to the lack of a standardized workflow, high initial costs, and the necessity for qualified professionals to analyze the data;
- **Operational performance**: Operational performance is the restricted payload capacity of lightweight UAVs. This limitation constrains the capability of UAVs to transport on-board instrumentation such as digital, stereo vision, and thermal cameras, as well as an array of sensors including temperature and Global Positioning System (GPS).

Adverse meteorological conditions, such as storms, rain, and wind, present substantial operational challenges. The utilization of UAVs within the context of PA is made problematic due to undesirable deviations from pre-established trajectories. Climate conditions directly influence the operational duration, flight paths, and altitude of UAVs. Under such

adverse conditions, UAVs are unable to hover, perform measurements, acquire accurate data, or operate effectively in extreme environments.

Given these significant challenges, especially those related to operational performance, there is an increasing need to explore virtual environments for the development and testing of UAVs. Simulating UAV operations in controlled, virtual settings allows researchers to refine flight dynamics, optimize data collection processes, and evaluate potential scenarios without the limitations imposed by real-world factors. This approach mitigates risks, reduces costs, and enhances the overall reliability of UAVs before their deployment in practical agricultural settings.

2.3 UAVs Over-actuated

UAVs classified as over-actuated systems are defined by having more actuators than the independent DoFs required for their control. This redundancy enhances system flexibility, enabling the implementation of advanced control strategies that optimize performance and reliability allowing for improved maneuverability, fault tolerance, and energy efficiency [70]. These characteristics make over-actuated UAVs appropriate for applications which require high precision and adaptability in complex environments [71], such as PA scenarios.

They are found in various designs in the literature. Li, Wei, Chen, *et al.* (2024) presented a novel over-actuated tricopter with a compact and innovative design, featuring three rotating arms connected to the airframe via servo-driven mechanisms to generate vectored thrust. In this configuration, each arm incorporates a rotor and a pair of perpendicularly mounted servos, enabling precise control over the direction and magnitude of the thrust force. The study addresses challenges associated with non-paired propellers, such as propeller reactive torque, gyroscopic effects, and counter torque generated by the servos. A robust controller with a compensation feature is proposed, leveraging feedback and a Quadratic Programming approach. The efficacy of the proposed aircraft is validated through simulation experiments, demonstrating the system's effectiveness and potential [72].

Similarly, Wang, Zhu, and Zhang (2020) showed a novel over-actuated tilting tri-rotor UAV, where each rotor has two tilting DoFs, resulting in nine controllable variables. To address the challenges posed by the system's nonlinear and coupled dynamics, a new control allocation method was developed, leveraging reversible mapping to simplify the nonlinear control allocation problem into a linear one. Simulation experiments demonstrated the system's ability to track various spatial trajectories with different attitudes, highlighting its high maneuverability compared to conventional quadrotors. This work successfully validated the efficacy of the proposed design, establishing an over-actuated UAV with advanced control and trajectory-tracking capabilities [73].

Gavgani, Talaeizadeh, Heidarzadeh, *et al.* (2024) proposed a novel over-actuated quadrotor that incorporates four additional control inputs to manipulate the angles of the propeller axes, addressing the limitations of conventional designs and enabling full independent control across all six DoF. The study implemented a nonlinear Sliding Mode Control (SMC) to handle unmodeled dynamics, uncertainties, and disturbances. An optimization criterion was applied to minimize power consumption, leveraging the system's over-actuated nature. Simulation results in MATLAB demonstrated the controller's robustness against challenges such as actuator inaccuracies, servo delays, and wind disturbances. This innovative approach successfully achieved an over-actuated UAV capable of enhanced maneuverability and stability, setting the foundation for future experimental validation and practical applications [74].

Wang and Zhang (2022) proposed an over-actuated hybrid fixed-wing UAV with an adaptive fault-tolerant control allocation strategy. The strategy is structured into two key modules: an intermediate virtual control and a control allocation scheme. The control allocation module acts as a low-level controller, distributing virtual control signals among actuators while accounting for their positional and rate constraints. In the event of actuator faults, discrepancies arise between the virtual control signals generated by the allocation module and those desired by the high-level control. To address this, the adaptive SMC dynamically adjusts the high-level control parameters, generating additional

virtual control signals to mitigate the effects of faults and maintain system stability. Simulation results, comparing this method to nominal SMC, demonstrate its effectiveness and superiority under both single and concurrent actuator fault scenarios in this aircraft [75].

Enenakpogbe, Whidborne, and Lu (2024) introduced an over-actuated fixed-wing UAV vectored thrust with a full-envelope controller. The proposed control architecture is versatile, applicable to piloted, semi-automatic, and fully-automated flight modes. In this aircraft, the controller comprises a main inner-loop non-linear dynamic inversion controller for forward cruise flight and an outer-loop proportional-integral linear controller for hover/low-speed and position control. The control allocation employs a new architecture that addresses the non-linearity in the vectored thrust effector model. Simulation results demonstrate a stable over-actuated UAV, showing the controller's ability to manage forward transitions from hover to cruise, handle saturation, and manage actuator failures, proving its robustness and versatility [76].

HajiAbedini, Zargarbashi, Talaeizadeh, *et al.* (2021) showed a over-actuated quadrotor featuring variable dihedral angles to achieve horizontal velocity without horizontal displacement by adjusting the rotor angles. The design focuses on the impact of rotor angle changes on thrust requirements for hover and other maneuvers. Flight experiments demonstrated that the quadrotor maintained stable performance in both normal and fixed dihedral configurations, even in crosswind conditions. Additionally, the variable dihedral mechanism showed minimal vibration and performed well under maximum thrust, with no slipping observed. Experimental results shows that this design provides enhanced maneuverability and stability, making it a promising approach for advanced quadrotor flight control [77].

Zhou, Li, Wang, *et al.* (2021) proposed a over-actuated hexacopter design in which each rotor can rotate around the body, with six arms coupled by bevel gears and controlled by servo motors to enable tilting motion. This configuration allows for decoupled control of position and attitude, enhancing the system's flexibility. The design is validated through simulations with a PID position controller and a quaternion-based attitude controller. The

results confirm the hexacopter's ability to perform tilt-hovering at large angles and track complex trajectories, demonstrating superior maneuverability and flexibility compared to traditional hexacopter designs [78].

Unfortunately, considering over-actuated UAVs, there is a notable lack of research directly focused on their application to PA. Most studies on over-actuated UAVs focus on their general applications, while research on the use of UAVs in PA typically involves conventional configurations. Furthermore, over-actuated configurations are particularly advantageous for PA due to their enhanced maneuverability, increased payload capacities, and the ability to optimize tilt angles provides greater energy efficiency. However, some limitations must be considered, including challenges in hardware integration, which can lead to unpredictable performance in real-world conditions, a critical issue for PA. Additionally, the lack of energy optimization presents a significant limitation for operations requiring extended flight times over large fields [79].

Chapter 3

Study of Tools

This chapter aims to contextualize the main tools used in the development of this work, discussing recent projects that have employed these tools within the scope of this study. Section 3.1 provides an overview of current work that has implemented different controller topologies in UAVs. Following this, Section 3.2 presents definitions and concepts of the ROS to provide a basis for a better understanding of this work. Section 3.3 discusses virtual environments, detailing the main tools with an emphasis on Gazebo software, which has been selected for this work, as well as some recent projects that have made use of virtual environments in UAVs studies. Furthermore, recent projects that used virtual environments in the study of UAVs are discussed. Finally, Section 3.4 explores the PX4 controller, emphasizing the vehicle configurations supported by this powerful tool.

3.1 UAV Controller

Achieving an aircraft with appropriate stability and control characteristics is a fundamental step in ensuring its performance. To achieve this objective, specific requirements must be satisfied. The essential characteristics that the vehicle must provide to perform its functions safely and efficiently include the following:

- Sufficient controllability to maintain level flight and transition safely between different equilibrium conditions;
- Control forces must be within the permissible limits specified in the design, considering the entire flight envelope;
- The aircraft must be capable of stabilization throughout the flight path.

Several control techniques are currently recognized, including P, Proportional-Integral (PI), Proportional-Derivative (PD) and PID controllers. Among these approaches, the choice of the most appropriate technique depends on several factors, such as the characteristics of the aircraft, its complexity, the operating environment, and performance requirements. Although other alternatives are available, PID control is widely used due to its effectiveness, low computational cost, and continued relevance in the UAVs field [80]. To facilitate the comparison of different control strategies employed in UAV systems, Table 3.1 summarizes the key aspects of related works:

Table 3.1: Overview of UAV control techniques in related works

Reference	**UAV**	**Controller**	**Objective**
[81]	Quadcopter	PI	Trajectory Control
[82]	Quadcopter	Cascade PD	Trajectory Tracking
[83]	Hexacopter	PID	Spraying for Agriculture
[84]	Quadcopter	PID	Trajectory Tracking
[85]	Quadcopter	PID	Stability under Wind Forces
[86]	Quadcopter	SMC	Altitude and Yaw Tracking
[87]	Quadcopter	SMC	Attitude Control
[88]	Five-Rotor	Model Predictive Control (MPC)	Hybrid Control
[89]	Quadcopter	Fault Tolerant Control (FTC)	Fault-Tolerant Control
[90]	Hexacopter	Adaptive Neural Network (NN)	Altitude and Attitude Tracking
[91]	Quadcopter	Cascade P-PID	Altitude Control

Srey and Srang (2024) proposes a trajectory control system for a quadcopter, using a PI controller with a feed-forward design to control the simplified model. Simulations conducted in MATLAB/Simulink indicated the UAV accurately follows circular and square trajectories, with a steady-state error of fewer than 0.05 meters for the x and y axes in 5 seconds and less than 0.02 meters for the z-axis within 2.5 seconds. The controller performance remains consistent over different trajectories, and the estimated parameters stabilize near-constant values at steady-state [81].

Yaşar and Karaköse (2022) presented a comprehensive analysis of a quadcopter that is performed, showing the modeling, control, and simulation process. A simple cascade PD controller was applied to the quadcopter. Using MATLAB-Simulink, the study conducted two distinct simulation processes, the first simulation focused on trajectory tracking by integrating a direct Euler rate script, while the second aimed to achieve circular trajectory flight. The results show that the quadcopter accurately follows the desired trajectory with minimal delay, while the second simulation demonstrated even more consistent trajectory tracking [82].

Rajan, Velmurugan, N, *et al.* (2023) developed the control of a hexacopter sprayer for deforestation and pest control. In this study, a PID controller was implemented, and sensor performance was evaluated to ensure the proper hexacopter functioning. A comparison with traditional methods revealed that the hexacopter sprayer outperformed conventional approaches in both efficiency and effectiveness. The UAV covered more ground in less time and was able to access challenging areas, reducing the need for manual labor. The PID controller contributed to stable altitude maintenance and effective obstacle avoidance throughout the process [83].

Basri *et al.* (2023) investigated the quadcopter trajectory tracking using a PID controller. The study presents the mathematical modeling of the quadcopter using Newton-Euler equations. Then, a manually tuned PID controller is designed to ensure stable flight and effective operation. Finally, the quadcopter was tested on five distinct trajectories, with the results demonstrating that the controller consistently and accurately tracked the desired flight paths [84].

Additionally, Hong (2023) presented a simulation and analysis of the stability of a PID controller used in a quadcopter under varying wind forces. The study outlines the dynamic modeling of the quadcopter and the implementation of the PID control algorithm. Simulations conducted in MATLAB analyze the developed system, and the results show that, despite delays and deviations in the responses, the PID controller can still ensure flight stability in the presence of environmental interference [85].

Despite the popularity of classical controllers, the increased demands for higher accuracy and robustness in dynamic environments have stimulated the development of sophisticated control methods. Chiew, Lee, Lee, *et al.* (2021) applied a second-order SMC for altitude and yaw quadcopter tracking control and compared it to a traditional PID controller. Two types of input were tested: a slow rate input with a single SetPoint (SP) and a fast rate input with multiple SPs. Simulation results demonstrated that the SMC controller approach consistently outperformed the traditional PID across all performance metrics [86].

In another study, Pan, Shao, Xiong, *et al.* (2023) proposed a novel Adaptive SMC based on the linear extended state observer used for attitude control of a quadcopter system under external disturbances. In their study, an adaptive switching algorithm for changing the switching gain in real time is proposed. Then the disturbance estimation error can be compensated by the variable gain switching term in real time, therefore the robustness of the system can be further improved. The stability of the system is proved by Lyapunov theory, and the experimental results provide that the proposed control strategy is feasible and effective [87].

Moreover, Xi, Huang, Tian, *et al.* (2021) introduced a Model Predictive Control (MPC) method for a five-rotor tilt-rotor UAV with rotor/wing interference. A hybrid control framework integrating both rotor and fixed-wing controllers is introduced. In this approach, the control laws for the rotor and fixed-wing are distributed based on a predefined weight coefficient. Simulations conducted in MATLAB/Simulink demonstrated the effectiveness of the proposed method [88].

With respect to another control structure, Jung and Bang (2021) proposed a Fault Tolerant Control (FTC) strategy for a quadcopter, addressing actuator faults through a complete FTC design that incorporates fault detection and diagnosis. This control approach relies on model predictive control, applying successive confiscation to handle nonlinear systems by converting nonconvex functions into convex ones via linearization. Actuator faults are modeled as loss of effectiveness and estimated using a two-stage Kalman filter. The proposed method has been validated through nonlinear simulations under various actuator fault scenarios. Simulations show that the new control proposed can handle nonsevere faults, severe faults, and complete actuator failures, all without requiring controller switching, even in the presence of actuator saturation [89].

Furthermore, Al-Mahasneh, Anavatti, Ferdaus, *et al.* (2021) set up an adaptive Neural Network (NN) controller for altitude tracking and attitude stabilization of a hexacopter with uncertain dynamics. The design, simulation, and robustness of the controller against gust disturbances were analyzed. Furthermore, the controller performance was compared with a standard filtered PID controller across different control scenarios. The results showed that the adaptive NN controller demonstrated quick and highly accurate performance controlling altitude and attitude. Additionally, this controller outperformed the filtered PID in multiple scenarios, providing better adaptation capabilities and reduced overshoot [90]. Additionally, several other noteworthy studies are available, including [92]–[96].

Regarding another notable controller configuration, which is employed in this presented work, the cascade P-PID topology is depicted. This controller is implemented considering two cascade levels fed: one external and one internal. The external uses a P controller and the internal uses a PID controller, so the output of the external control action is the input of the internal cascade controller, refining the dynamic response to ensure precision and robustness in the control. Burggräf, Pérez Martínez, Roth, *et al.* (2019) presented a cascade P-PID implemented in a quadcopter designed for indoor and outdoor flights, aiming to enhance safety features in industrial applications. In this study, the control system is configured in an 'X' frame, and control was achieved using four input

commands from a radio controller. The results demonstrated that the approach controller implemented successfully provided the desired stability across all flight conditions. The quadcopter exhibited fast and stable reactions to external disturbances, proving effective in maintaining consistent performance both indoors and outdoors, regardless of environmental variations [91].

3.2 Robot Operating System

ROS is an open-source development platform that is widely recognized and adopted in the field of robotics. It is designed to provide common operating system services, offering hardware abstraction, low-level device control, the implementation of commonly used functions, message passing between processes, and package management [97].

ROS provides a robust set of tools and libraries that facilitate the acquisition, building, writing, and execution of code, creating a powerful development environment. Since its creation, ROS has been propelled by a collaborative global community of engineers, developers, and enthusiasts, whose contributions have promoted the constant evolution and adoption of robotic solutions across various sectors [98]. Its adaptability allows ROS to be utilized in a wide range of robotic applications, including industrial robots and UAV. The flexibility and scalability of ROS make it the preferred choice for both research projects and commercial applications in the robotics field.

The distributed architecture of ROS uses a graphical structure composed of nodes that communicate through topics and services. These nodes use an efficient messaging system for data transmission and reception. This communication model facilitates the integration and coordination of various components of a robotic system [99]. The essential elements of ROS include:

- **Packages**: Packages are the organization units of ROS. A package contains nodes, libraries, launch files, configuration files, and useful modules to provide useful functionality in an easy-to-consume way so that software can be easily reused;

- **Nodes**: Nodes represent individual processes that have a specific task in the overall system, such as robot control, localization, and path planning. The communication between these nodes is performed via topics and services;
- **Topics**: Topics are a transport system that sends messages from one node to another node. The nodes publish and/or subscribe to topics to send and/or receive these messages. A topic can only receive messages whose type is specified by the user;
- **Messages**: Messages are simply a data structure consisting of typed fields. Standard primitive types are supported, as are arrays of primitive types. Nodes communicate with each other by passing messages;
- **Services**: Services are based on the request/response model: request and response are performed, defined by a pair of message structures, one for the request and one for the response. A providing node offers a service under a name, and a client uses the service by sending the request message and awaiting the response.

Since its release, ROS 1 provided a robust foundation with a wide array of tools for robotic development. As a result of changes in robotics and the ROS community, ROS 2 has emerged as a significant advancement. ROS 2 is a rework of the framework, developed to offer better support, improve security, and ensure compatibility with new real-time technologies [100]. Both ROS 1 and ROS 2 have demonstrated their effectiveness and versatility in various applications. In the literature, there are several studies with ROS using UAVs [101]–[106].

3.3 Virtual Environments

Virtual environments are a useful tool and good practice in the process of developing robot designs and algorithms, allowing for extensive testing before deploying code on physical robotic systems. Due to the inherent complexity, expense, fragility, and limited availability of physical robots, it is common to initially evaluate theoretical methods within a simulator. These environments provide a safe and low-cost space for testing and validating algorithms [107].

Various simulators are available for testing in virtual environments, including commercial and open-source options. Commercial simulators such as X-Plane [108] and Microsoft Flight Simulator [109] are renowned for their high fidelity and realism, but their associated licensing costs can be prohibitive for many users. In contrast, widely-used free and open-source simulators such as WeBots [110], Unity [111], AirSim [112], and MORSE [113], provide robust and flexible simulation environments. These tools are frequently used in research due to their accessibility [114].

A widely used tool in the robotic community is Gazebo software, which is used for conducting Software In The Loop (SITL) simulations of UAVs [115]. Gazebo is an open-source simulator that is intrinsically integrated with ROS, offering a powerful tool for creating realistic scenarios to conduct flight simulations under different conditions. It enables the evaluation of control algorithms and testing of navigation systems. Its robustness and extensibility have contributed to its popularity, particularly in the educational field.

Several studies have demonstrated UAV simulation applications using Gazebo simulation. Zenkin, Berman, Pachkouski, *et al.* (2020) described a quadcopter simulation to monitor a large area. Three scenarios have been considered: detection of the source of the fire in the forest, detection of intruders in the restricted area, and detection of cars. Then, Gazebo with MAVLink (the communication protocol for UAVs and PX4 autopilot system) were used. The results the demonstrated the performance of the quadcopter in monitoring tasks. It was seen that the quadcopter could accurately follow the desired trajectory and quickly cover the area [116].

In contrast, Nair, Sareth, Bhavani, *et al.* (2022) provided a quadcopter simulation using ArduPilot flight controller and QGroundControl software. In this work, Gazebo was employed to demonstrate the concept and test the stability of the flight algorithm [117].

In another study, Megalingam, Prithvi, Kumar, *et al.* (2022) proposed a control algorithm using PID control, which was modeled to ensure stability and enable a quadcopter to hover at a desired point within the Gazebo and ROS environments [118]. Lastly, Xavier, Santos, and Givigi (2023) presents a SITL environment focused on multiple UAVs to validate cooperative control algorithms. The presented study features several control layers and is implemented using ROS 1, Gazebo software, and MATLAB/Simulink [119].

3.4 PX4 Autopilot

PX4 Autopilot is a widely used open-source autopilot platform for controlling UAVs, covering a wide range of vehicle types, from fixed-wing and multi-rotor aircraft to water vehicles and submarines. This platform has a complete ecosystem of tools, including flight controller boards compatible with various supported sensors, autopilot firmware for different vehicle types and configurations, and ground control software for operating UAVs [120].

Developed by a global community of engineers, computer scientists, and enthusiasts, PX4 is constantly adapting to new demands and integrating emerging technologies. The system enables the autonomous operation of unmanned vehicles, even under uncertain conditions such as environmental variations (e.g., wind and currents) or uncertainties related to the vehicle itself (e.g., mass, payload, and geometry) [121]. Figure 3.1 below provides a high-level overview of a typical PX4 system based around a flight controller, illustrating its core components and their interactions:

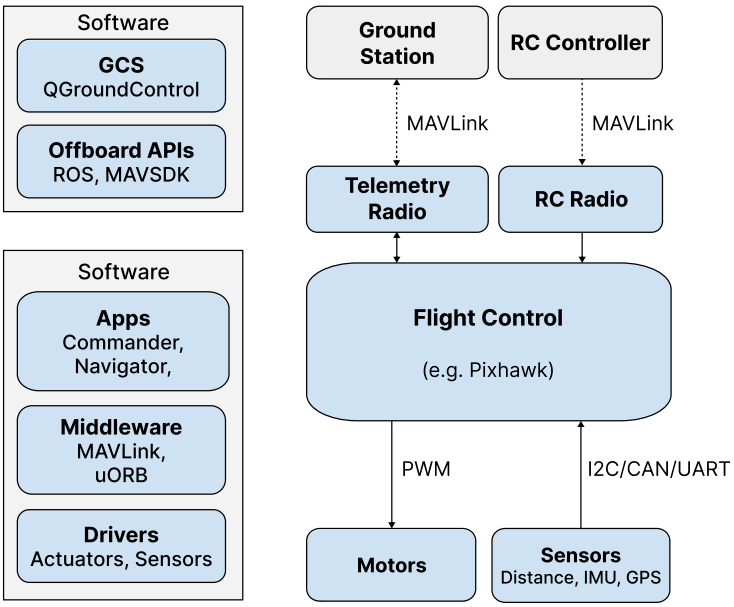

Figure 3.1: Overview of the PX4 system architecture (Adapted from PX4 site)

This flexible platform supports a wide variety of vehicle types, each optimized for specific airframe configurations. It includes specialized branches for different flight platforms: Multicopters such as quadcopters, hexacopters, and octocopters; fixed-wing aircraft including standard planes and flying wings; VTOL aircraft; and other vehicle types such as rovers and submarines. Figure 3.2 illustrates the different types of vehicles supported by PX4 Autopilot:

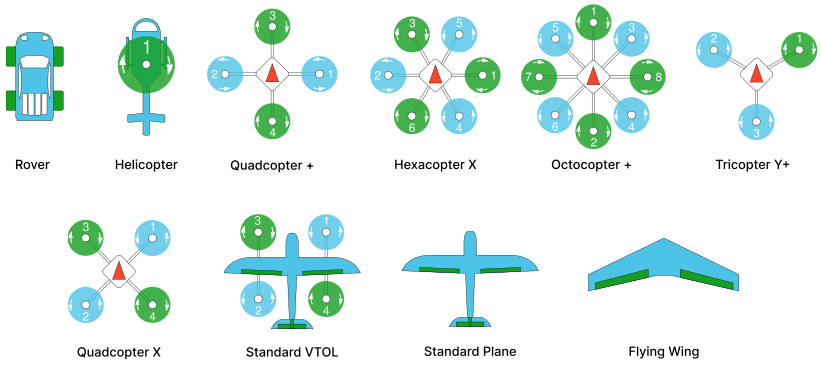

Figure 3.2: Vehicle supported by PX4 Autopilot (Adapted from PX4 site)

Several studies focused on PX4 vehicles are notable in the literature. Jing, Wang, Heredia-Juesas, *et al.* (2022) presented a design of a disturbance-observer-based nonlinear sliding mode surface controller using a simulated PX4 quadcopter. Comparisons of PID control strategies with the SMC were conducted under identical conditions. The simulations indicate that the SMC controller, incorporating a disturbance observer, enables precise and rapid adaptation of the UAV in uncertain dynamic environments [122].

In contrast, Gomez, Gomez, Rodas, *et al.* (2020) proposed an offline tuning procedure based on the multi-objective particle swarm optimization algorithm for the attitude and altitude control of a PX4-based UAV. The concept of Pareto dominance is employed to identify optimal values for the PID parameters by comparing step response characteristics, including overshoot, rise time, and root-mean-square error. Experimental results validated the proposed tuning procedure, using a quadcopter as a case study [123].

Chapter 4

Development

For the continuation of the work, the modeling process includes both the kinematic and dynamic aspects of the proposed HTR, which is presented in Section 4.1. Following this, Section 4.2 introduces the control allocation method used, an extended FCA, which reduces the complexity of managing nonlinearities in vehicle control. Section 4.3 details the implemented control structure, including the control loops developed for the HTR and specific control gains obtained. Finally, Section 4.4 presents the simulation configurations and provides a comprehensive explanation to clarify the overall functionality of the developed autonomous navigation algorithm.

4.1 Modeling of hexacopter

The first crucial step is to an accurate mathematical model of the proposed HTR for this work. This modeling process includes both the hexacopter kinematic and dynamic aspects, which serve as the foundation for understanding its flight behavior. This section aims to introduce the key elements necessary for the precise HTR representation, including equations of motion that govern its dynamics.

4.1.1 Coordinate frames

Different coordinate axes used by the HTR are essential for understanding the vehicle orientation and position relative to the ground and its own body frame [124]. There are several reasons for using different coordinate systems [125], including:

- Equations of motion based on Newton's laws are derived with respect to the fixed inertial frame of reference;
- Aerodynamic forces and torques are applied to the hexacopter body, which is described in the fixed frame of the vehicle;
- Sensors measure information with respect to the hexacopter body frame and others measure information with respect to the inertial frame;
- Mission requirements are based on the fixed inertial frame.

4.1.1.1 Inertial frame

The inertial coordinate frame, $\mathcal{F}^i$, is aligned to the Earth's fixed coordinate system, with its origin located at the ground control station [126]. As indicated in Figure 4.1, the vector $\boldsymbol{i}^{\boldsymbol{i}}$ points North, $\boldsymbol{j}^{\boldsymbol{i}}$ points East, and $\boldsymbol{k}^{\boldsymbol{i}}$ points toward the Earth's center. This coordinate system is known as North-East-Down (NED) [126].

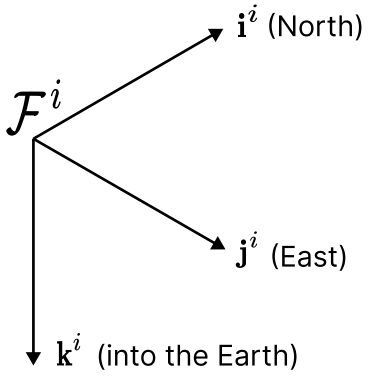

Figure 4.1: Inertial coordinate frame

4.1.1.2 Vehicle frame

The vehicle coordinate system, $\mathcal{F}^v$, is centered at the HTR center of mass, with its axes aligned to the axes of the inertial frame $\mathcal{F}^i$. In this way, the unit vector $\boldsymbol{i^v}$ points North, $\boldsymbol{j^v}$ points East, and $\boldsymbol{k^v}$ is directed toward the Earth's center, as depicted in Figure 4.2 [125]:

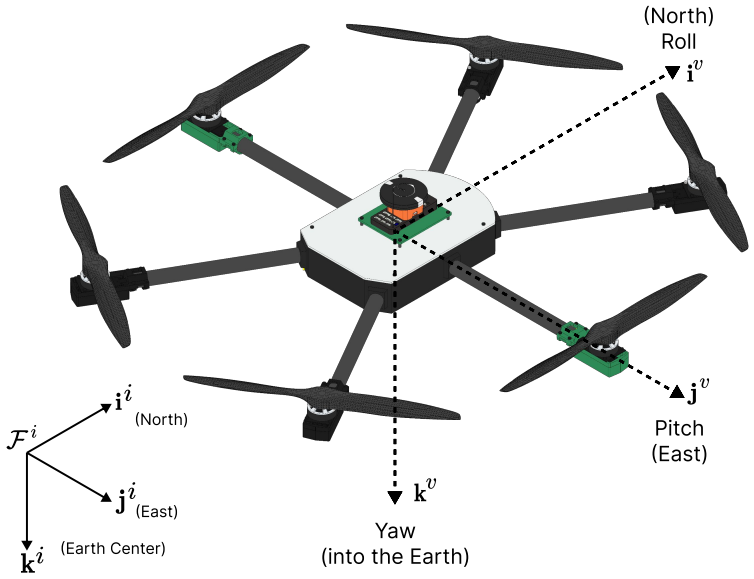

Figure 4.2: Coordinate frame $\mathcal{F}^v$

4.1.1.3 Vehicle 1 frame

The origin of the frame of the vehicle 1, $\mathcal{F}^{v1}$, coincides with the vehicle frame $\mathcal{F}^v$, at the HTR center of mass. However, $\mathcal{F}^{v1}$ is rotated positively around the $\boldsymbol{k^v}$ axis by a yaw angle (ψ) [125].

Consequently, in the absence of additional rotations, $\boldsymbol{i^{v1}}$ points forward, $\boldsymbol{j^{v1}}$ points to the right, and $\boldsymbol{k^{v1}}$ is aligned with $\boldsymbol{k^v}$, pointing toward the Earth, as illustrated in Figure 4.3:

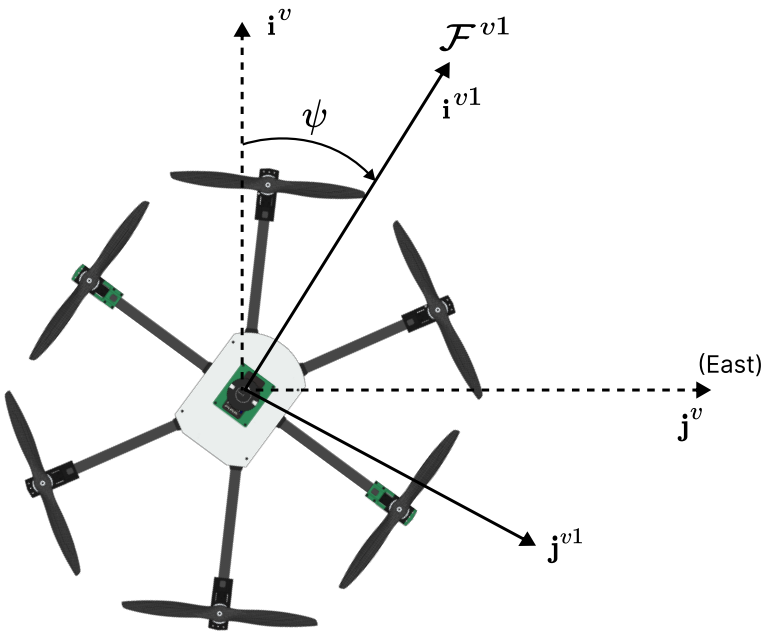

Figure 4.3: Coordinate frame $\mathcal{F}^{v1}$

The transformation from $\mathcal{F}^v$ to $\mathcal{F}^{v1}$ is given by:

$$\mathbf{p}^{v1} = \boldsymbol{R}_v^{v1}(\psi)\mathbf{p}^v, \tag{4.1}$$

where,

$$\boldsymbol{R}_v^{v1}(\psi) = \begin{pmatrix} \cos\psi & \sin\psi & 0 \\ -\sin\psi & \cos\psi & 0 \\ 0 & 0 & 1 \end{pmatrix}. \tag{4.2}$$

4.1.1.4 Vehicle 2 frame

The frame of the vehicle 2, $\mathcal{F}^{v2}$, is also centered at the HTR center of mass. This frame is derived by applying a right-handed rotation to the $\mathcal{F}^{v1}$ frame around the $\boldsymbol{j^{v1}}$ axis by a pitch angle (θ). Consequently, if the roll angle is zero, the vector $\boldsymbol{i^{v2}}$ points towards the HTR's nose, $\boldsymbol{j^{v2}}$ points to the vehicle's right side, and $\boldsymbol{k^{v2}}$ points to the ground [125].

The $\mathcal{F}^{v2}$ frame is shown in Figure 4.4:

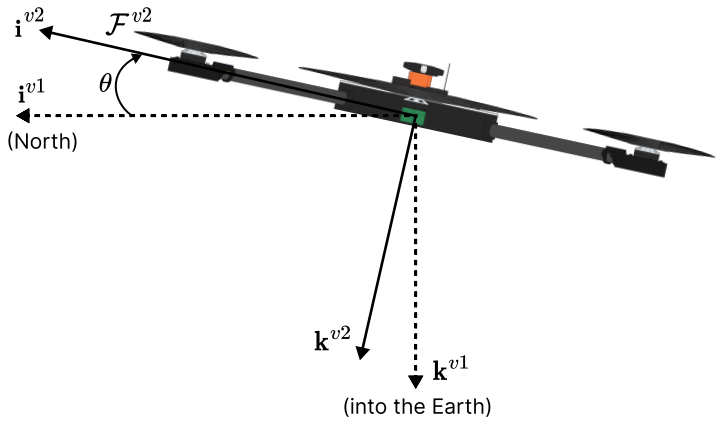

Figure 4.4: Coordinate frame $\mathcal{F}^{v2}$

The transformation from $\mathcal{F}^{v1}$ to $\mathcal{F}^{v2}$ is given by:

$$\mathbf{p}^{v2} = \boldsymbol{R}_{v1}^{v2}(\theta)\mathbf{p}^{v1}, \tag{4.3}$$

where,

$$\boldsymbol{R}_{v1}^{v2}(\theta) = \begin{pmatrix} \cos\theta & 0 & -\sin\theta \\ 0 & 1 & 0 \\ \sin\theta & 0 & \cos\theta \end{pmatrix}. \tag{4.4}$$

4.1.1.5 Body frame

The body-fixed frame, $\mathcal{F}^b$, is obtained by applying a right-handed rotation to the $\mathcal{F}^{v2}$ reference frame around the $\boldsymbol{i^{v2}}$ axis by a roll angle (ϕ). In this way, remains at the HTR center of mass, with $\boldsymbol{i^b}$ pointing towards the HTR's nose, $\boldsymbol{j^b}$ directed to the right side, and $\boldsymbol{k^b}$ pointing to the ground [125]. The $\mathcal{F}^b$ frame is illustrated in Figure 4.5:

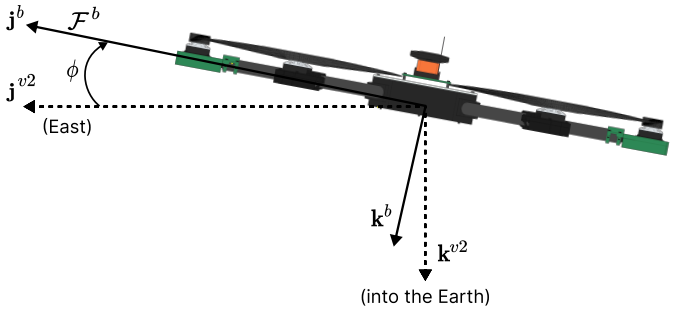

Figure 4.5: Coordinate frame $\mathcal{F}^b$

The transformation from $\mathcal{F}^{v2}$ to $\mathcal{F}^b$ is given by:

$$\mathbf{p}^b = \boldsymbol{R}^b_{v2}(\phi)\mathbf{p}^{v2}, \tag{4.5}$$

where,

$$\boldsymbol{R}^b_{v2}(\phi) = \begin{pmatrix} 1 & 0 & 0 \\ 0 & \cos\phi & \sin\phi \\ 0 & -\sin\phi & \cos\phi \end{pmatrix}. \tag{4.6}$$

Lastly, the transformation from the vehicle frame $\mathcal{F}^v$ to the body frame $\mathcal{F}^b$ can be described by:

$$\boldsymbol{R}^b_v(\phi,\theta,\psi) = \boldsymbol{R}^b_{v2}(\phi)\boldsymbol{R}^{v2}_{v1}(\theta)\boldsymbol{R}^{v1}_v(\psi), \tag{4.7}$$

$$\boldsymbol{R}^b_v(\phi,\theta,\psi) = \begin{pmatrix} c\theta c\psi & c\theta s\psi & -s\theta \\ s\phi s\theta c\psi - c\phi s\psi & s\phi s\theta s\psi + c\phi c\psi & s\phi c\theta \\ c\phi s\theta c\psi + s\phi s\psi & c\phi s\theta s\psi - s\phi c\psi - s\phi c\psi & c\phi c\theta \end{pmatrix}, \tag{4.8}$$

where, $c\phi = \cos\phi$ and $s\phi = \sin\phi$.

4.1.2 Equation of Coriolis

Based on the methodology presented by Stevens, Lewis, and Johnson [127], consider two coordinate frames: $\mathcal{F}^i$, representing the inertial frame, and $\mathcal{F}^b$, representing the HTR body frame. In this scenario, it is assumed that the vector $\mathbf{p}$ is moving within $\mathcal{F}^b$, while $\mathcal{F}^b$ simultaneously rotates and translates with respect to $\mathcal{F}^i$, as illustrated in Figure 4.6:

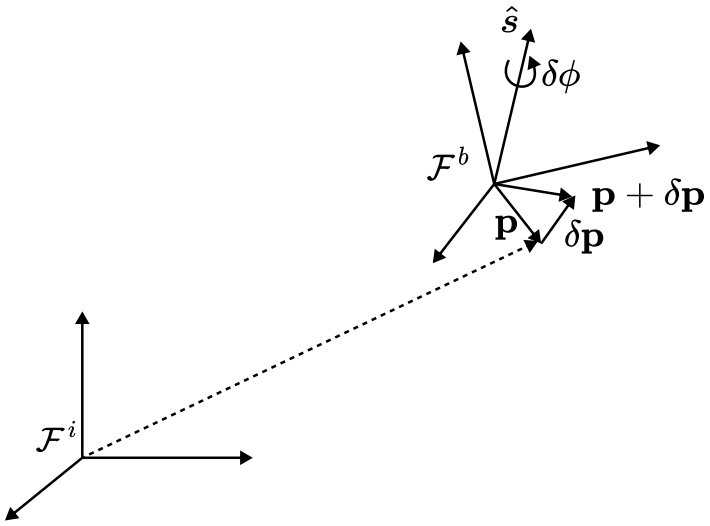

Figure 4.6: Scheme of the references to equation of Coriolis

The objective of the Coriolis equation is to determine the time derivative of the vector $\mathbf{p}$ with respect to the inertial frame $\mathcal{F}^i$. Therefore, first it is assumed that $\mathcal{F}^b$ is not rotating with respect to $\mathcal{F}^i$:

$$\frac{d}{dt_i}\mathbf{p} = \frac{d}{dt_b}\mathbf{p}. \tag{4.9}$$

Subsequently, assuming that the vector $\mathbf{p}$ is fixed in $\mathcal{F}^b$, which is rotating with respect to $\mathcal{F}^i$ and considering $\hat{s}$ as the instantaneous axis of rotation and $\delta\phi$ the rotation angle, the Equation can be expressed as:

$$\mathbf{p} + \delta\mathbf{p} = (1 - \cos(-\delta\phi))\hat{s}(\hat{s} \cdot \mathbf{p}) + \cos(-\delta\phi)\mathbf{p} - \sin(-\delta\phi)\hat{s} \times \mathbf{p}. \tag{4.10}$$

Adopting a small angles approximation and dividing both sides of the equation by δt:

$$\frac{\delta \mathbf{p}}{\delta t} \approx \frac{\delta \phi}{\delta t} \hat{s} \times \mathbf{p}. \tag{4.11}$$

Assuming $\delta t \to 0$ and defining the angular velocity of the body frame ($\mathcal{F}^b$) with respect to the inertial frame ($\mathcal{F}^i$) as $\omega_{b/i} \triangleq \hat{s}\dot{\phi}$:

$$\frac{d}{dt_i}\mathbf{p} = \omega_{b/i} \times \mathbf{p}. \tag{4.12}$$

Since the derivative is a linear operator, it is possible to merge Equations 4.11 and 4.12, to obtain Equation 4.13, known as the equation of Coriolis:

$$\frac{d}{dt_i}\mathbf{p} = \frac{d}{dt_b}\mathbf{p} + \omega_{b/i} \times \mathbf{p}. \tag{4.13}$$

4.1.3 Kinematic and dynamic modeling

Kinematic and dynamic behavior of a hexacopter can be described according to twelve state variables, as follows [125]:

p_n = hexacopter inertial position (north)along $\hat{\boldsymbol{i}}^{\boldsymbol{i}}$ in $\mathcal{F}^i$

p_e = hexacopter inertial position (east) along $\hat{\boldsymbol{j}}^{\boldsymbol{i}}$ in $\mathcal{F}^i$

h = hexacopter altitude measured along $-\hat{\boldsymbol{k}}^{\boldsymbol{i}}$ in $\mathcal{F}^i$

u = body frame velocity measured along $\hat{\boldsymbol{i}}^{\boldsymbol{b}}$ in $\mathcal{F}^b$

v = body frame velocity measured along $\hat{\boldsymbol{j}}^{\boldsymbol{b}}$ in $\mathcal{F}^b$

w = body frame velocity measured along $\hat{\boldsymbol{k}}^{\boldsymbol{b}}$ in $\mathcal{F}^b$

ϕ = roll angle defined with respect to $\mathcal{F}^{v2}$

θ = pitch angle defined with respect to $\mathcal{F}^{v1}$

ψ = yaw angle defined with respect to $\mathcal{F}^v$

p = roll rate measured along $\hat{\boldsymbol{i}}^b$ in $\mathcal{F}^b$

q = pitch rate measured along $\hat{\boldsymbol{j}}^b$ in $\mathcal{F}^b$

r = yaw rate measured along $\hat{\boldsymbol{k}}^b$ in $\mathcal{F}^b$

To better understand the kinematics and dynamics modeling equations is necessary to present their state variables. Figure 4.7 illustrates them on their respective axes:

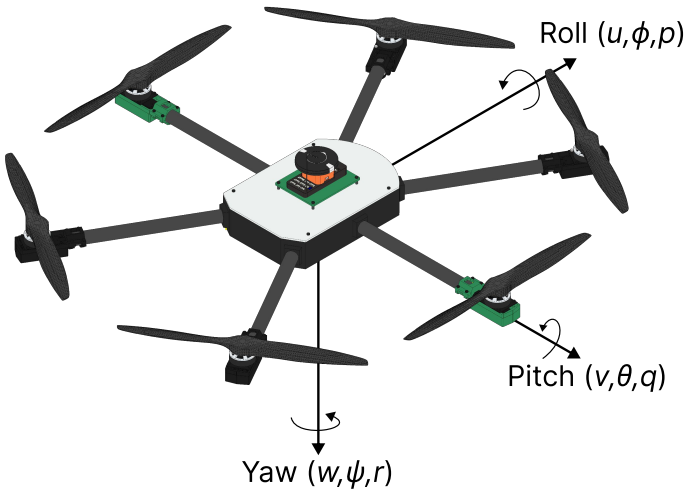

Figure 4.7: HTR with its state variables

4.1.3.1 Hexacopter Kinematics

The state variables p_n, p_e, and $-h$ are inertial frame quantities, whereas the velocities u, v, and w are body frame quantities [128]:

$$\frac{d}{dt}\begin{pmatrix} p_n \\ p_e \\ -h \end{pmatrix} = \boldsymbol{R}_v^b \begin{pmatrix} u \\ v \\ w \end{pmatrix} = (\boldsymbol{R}_v^b)^T \begin{pmatrix} u \\ v \\ w \end{pmatrix}, \tag{4.14}$$

$$\begin{pmatrix} \dot{p}_n \\ \dot{p}_e \\ -\dot{h} \end{pmatrix} = \begin{pmatrix} c\theta c\psi & s\phi s\theta c\psi - c\phi s\psi & c\phi s\theta c\psi + s\phi s\psi \\ c\theta s\psi & s\phi s\theta s\psi + c\phi c\psi & c\phi s\theta s\psi - s\phi c\psi \\ -s\theta & s\phi c\theta & c\phi c\theta \end{pmatrix} \begin{pmatrix} u \\ v \\ w \end{pmatrix}. \tag{4.15}$$

The relationship between the angles roll, pitch, and yaw (ϕ, θ, ψ) and their corresponding angular rates (p, q, r) must also be considered for frame transformations [125]. The angular rates are defined within the reference frame $\mathcal{F}^b$, while the roll angle is referenced in the frame $\mathcal{F}^{v2}$, the pitch angle in the frame $\mathcal{F}^{v1}$, and the yaw angle in the vehicle frame $\mathcal{F}^v$ [128].

Therefore, it is important to use rotation matrices, since the positions and speeds are in different frames. So:

$$\begin{pmatrix} p \\ q \\ r \end{pmatrix} = \begin{pmatrix} \dot{\phi} \\ 0 \\ 0 \end{pmatrix} + \boldsymbol{R}_{v2}^{b}(\phi) \begin{pmatrix} 0 \\ \dot{\theta} \\ 0 \end{pmatrix} + \boldsymbol{R}_{v2}^{b}(\phi)\boldsymbol{R}_{v1}^{v2}(\theta) \begin{pmatrix} 0 \\ 0 \\ \dot{\psi} \end{pmatrix}, \tag{4.16}$$

$$= \begin{pmatrix} \dot{\phi} \\ 0 \\ 0 \end{pmatrix} + \begin{pmatrix} 1 & 0 & 0 \\ 0 & c\phi & s\phi \\ 0 & -s\phi & c\phi \end{pmatrix} \begin{pmatrix} 0 \\ \dot{\theta} \\ 0 \end{pmatrix} + \begin{pmatrix} 1 & 0 & 0 \\ 0 & c\phi & s\phi \\ 0 & -s\phi & c\phi \end{pmatrix} \begin{pmatrix} c\theta & 0 & -s\theta \\ 0 & 1 & 0 \\ s\theta & 0 & c\theta \end{pmatrix} \begin{pmatrix} 0 \\ 0 \\ \dot{\psi} \end{pmatrix}, \tag{4.17}$$

$$= \begin{pmatrix} p \\ q \\ r \end{pmatrix} = \begin{pmatrix} 1 & 0 & -s\theta \\ 0 & c\phi & s\phi c\theta \\ 0 & -s\phi & c\phi c\theta \end{pmatrix}. \tag{4.18}$$

Manipulating the matrices:

$$= \begin{pmatrix} \dot{\phi} \\ \dot{\theta} \\ \dot{\psi} \end{pmatrix} = \begin{pmatrix} 1 & s\theta t\theta & c\phi t\theta \\ 0 & c\phi & -s\phi \\ 0 & s\phi/c\theta & c\phi/c\theta \end{pmatrix} \begin{pmatrix} p \\ q \\ r \end{pmatrix}, \tag{4.19}$$

where, $c\theta = \cos\theta$, $s\theta = \sin\theta$, and $t\theta = \tan\theta$.

4.1.3.2 Hexacopter Dynamics

The dynamic modeling of a hexacopter is made using translational and rotational movements, applying Newton's second law [125]. Taking v as the HTR velocity in the inertial frame $\mathcal{F}^i$. Applying Newton's law to translational motion yields:

$$\boldsymbol{f} = m\frac{d\boldsymbol{v}}{dt_i}, \tag{4.20}$$

where m is the HTR total mass, f is the total force applied to the vehicle (gravitational force, aerodynamic force, and engine propulsion force). From Equation 4.13:

$$\boldsymbol{f} = m\frac{dv}{dt_i} = m\left(\frac{d\mathbf{v}}{dt_b} + \boldsymbol{\omega}_{b/i} \times \mathbf{v}\right). \tag{4.21}$$

Given that the control force is measured and applied in the body frame $\mathcal{F}^b$, and considering that the angular velocity $\omega_{b/i}$ is also measured in the body frame, Equation 4.21 can be reformulated in the body reference frame. Here, $\mathbf{v}^b \triangleq (u, v, w)^T$, and $\omega^b_{b/i} \triangleq (p, q, r)^T$. Consequently, in the body frame, it can be expressed as follows [125]:

$$\begin{pmatrix} \dot{u} \\ \dot{v} \\ \dot{w} \end{pmatrix} = \begin{pmatrix} rv - qw \\ pw - ru \\ qu - pv \end{pmatrix} + \frac{1}{m}\begin{pmatrix} f_x \\ f_y \\ f_z \end{pmatrix}, \tag{4.22}$$

where, f_x, f_y and f_z are the resulting forces applied to the frame $\mathcal{F}^b$, in the $\hat{\boldsymbol{i}}^{\boldsymbol{b}}$, $\hat{\boldsymbol{j}}^{\boldsymbol{b}}$ and $\hat{\boldsymbol{k}}^{\boldsymbol{b}}$ axes, respectively.

However, it should be considered that gravity also acts on the hexacopter within the vehicle frame $\mathcal{F}^v$, at the center of mass. Therefore:

$$\boldsymbol{f}^{\boldsymbol{v}}_{\boldsymbol{g}} = \begin{pmatrix} 0 \\ 0 \\ mg \end{pmatrix}. \tag{4.23}$$

Since velocity $\mathbf{v}$ is expressed in the body frame $\mathcal{F}^b$, it should be transformed into the

body frame as described by:

$$\boldsymbol{f}_{\boldsymbol{b}}^{\boldsymbol{v}} = \boldsymbol{R}_{\boldsymbol{v}}^{\boldsymbol{b}} \begin{pmatrix} 0 \\ 0 \\ mg \end{pmatrix} = \begin{pmatrix} -mg\sin\theta \\ mg\cos\theta\sin\phi \\ mg\cos\theta\cos\phi \end{pmatrix}. \tag{4.24}$$

Therefore, taking into consideration the gravity acceleration ($g = 9.81 m/s^2$):

$$\begin{pmatrix} \dot{u} \\ \dot{v} \\ \dot{w} \end{pmatrix} = \begin{pmatrix} rv - qw \\ pw - ru \\ qu - pv \end{pmatrix} \begin{pmatrix} -g\sin\theta \\ g\cos\theta\sin\phi \\ g\cos\theta\cos\phi \end{pmatrix} + \frac{1}{m} \begin{pmatrix} 0 \\ 0 \\ -F \end{pmatrix}, \tag{4.25}$$

where, F is the UAV propulsion force.

For rotational motion, Newton's second law becomes:

$$\frac{d\mathbf{h}^b}{dt_i} = \mathbf{m}, \tag{4.26}$$

where, $\mathbf{h}^b \in \mathbb{R}^3$ represents the angular momentum of the body, and $\mathbf{m} \in \mathbb{R}^3$ denotes the sum of all applied torques. This expression is true for applied moments at the center of mass [125].

Applying the Coriolis equation provided in 4.13:

$$\frac{d\mathbf{h}}{dt_i} = \frac{d\mathbf{h}}{dt_b} + \boldsymbol{\omega}_{b/i} \times \mathbf{h} = \mathbf{m}. \tag{4.27}$$

In rigid bodies, angular momentum is defined as the product of the inertia matrix $\mathbf{J}$ and the angular velocity vector, represented as $\boldsymbol{h}^{\boldsymbol{b}} \triangleq \boldsymbol{J}\boldsymbol{\omega}_{\boldsymbol{b/i}}^{\boldsymbol{b}}$ [129]. The matrix $\mathbf{J}$ is expressed as follows:

$$\mathbf{J} = \begin{pmatrix} \int (y^2+z^2)dm & -\int xydm & -\int xzdm \\ -\int xydm & \int (x^2+z^2)dm & -\int yzdm \\ -\int xzdm & -\int yzdm & \int (x^2+y^2)dm \end{pmatrix}, \tag{4.28}$$

$$\triangleq \begin{pmatrix} J_x & -J_{xy} & -J_{xz} \\ -J_{xy} & J_y & -J_{yz} \\ -J_{xz} & -J_{yz} & J_z \end{pmatrix}. \tag{4.29}$$

The moments of inertia for the vehicle are calculated by considering a large sphere with mass M and radius R at the center of the vehicle's mass. Additionally, points masses of mass m represent the motors masses, at a distance l from the central sphere [125]. Thus, the HTR is symmetric about the coordinate axes, so the moments of inertia $J_{xz} = J_{xy} = J_{yz} = 0$. This implies that:

$$\mathbf{J} = \begin{pmatrix} J_x & 0 & 0 \\ 0 & J_y & 0 \\ 0 & 0 & J_z \end{pmatrix}. \tag{4.30}$$

Consequently, the moment of inertia of a sphere is described by $J = 2MR^2/5$. Thus:

$$J_x = \frac{2MR^2}{5} + 4\ell^2 m, \tag{4.31}$$

$$J_y = \frac{2MR^2}{5} + 4\ell^2 m, \tag{4.32}$$

$$J_z = \frac{2MR^2}{5} + 6\ell^2 m. \tag{4.33}$$

Therefore, considering $\mathbf{m}^b \triangleq (\tau_\phi, \tau_\theta, \tau_\psi)^T$, Equation 4.27 can be represented by:

$$\begin{pmatrix}\dot{p}\\ \dot{q}\\ \dot{r}\end{pmatrix} = \begin{pmatrix}\frac{1}{J_x} & 0 & 0\\ 0 & \frac{1}{J_y} & 0\\ 0 & 0 & \frac{1}{J_z}\end{pmatrix}\left[\begin{pmatrix}0 & r & -q\\ -r & 0 & p\\ q & -p & 0\end{pmatrix}\begin{pmatrix}J_x & 0 & 0\\ 0 & J_y & 0\\ 0 & 0 & J_z\end{pmatrix}\begin{pmatrix}p\\ q\\ r\end{pmatrix} + \begin{pmatrix}\tau_\phi\\ \tau_\theta\\ \tau_\psi\end{pmatrix}\right], \quad (4.34)$$

$$\begin{pmatrix}\dot{p}\\ \dot{q}\\ \dot{r}\end{pmatrix} = \begin{pmatrix}\frac{J_y-J_z}{J_x}qr\\ \frac{J_z-J_x}{J_y}pr\\ \frac{J_x-J_y}{J_z}pq\end{pmatrix} + \begin{pmatrix}\frac{1}{J_x}\tau_\phi\\ \frac{1}{J_y}\tau_\theta\\ \frac{1}{J_z}\tau_\psi\end{pmatrix}. \quad (4.35)$$

The six DoF model for the HTR kinematics and dynamics can be summarized as follows:

$$\begin{pmatrix}\dot{p}_n\\ \dot{p}_e\\ -\dot{h}\end{pmatrix} = \begin{pmatrix}c\theta c\psi & s\phi s\theta c\psi - c\phi s\psi & c\phi s\theta c\psi + s\phi s\psi\\ c\theta s\psi & s\phi s\theta s\psi + c\phi c\psi & c\phi s\theta s\psi - s\phi c\psi\\ -s\theta & s\phi c\theta & c\phi c\theta\end{pmatrix}\begin{pmatrix}u\\ v\\ w\end{pmatrix}, \quad (4.36)$$

$$\begin{pmatrix}\dot{u}\\ \dot{v}\\ \dot{w}\end{pmatrix} = \begin{pmatrix}rv - qw\\ pw - ru\\ qu - pv\end{pmatrix} + \begin{pmatrix}-g\sin\theta\\ g\cos\theta\sin\phi\\ g\cos\theta\cos\phi\end{pmatrix} + \frac{1}{m}\begin{pmatrix}0\\ 0\\ -F\end{pmatrix}, \quad (4.37)$$

$$\begin{pmatrix}\dot{\phi}\\ \dot{\theta}\\ \dot{\psi}\end{pmatrix} = \begin{pmatrix}1 & \sin\theta\tan\phi & \cos\theta\tan\phi\\ 0 & \cos\phi & -\sin\phi\\ 0 & \sin\phi/\cos\theta & \cos\phi/\cos\theta\end{pmatrix}\begin{pmatrix}p\\ q\\ r\end{pmatrix}, \quad (4.38)$$

$$\begin{pmatrix}\dot{p}\\ \dot{q}\\ \dot{r}\end{pmatrix} = \begin{pmatrix}\frac{J_y-J_z}{J_x}qr\\ \frac{J_z-J_x}{J_y}pr\\ \frac{J_x-J_y}{J_z}pq\end{pmatrix} + \begin{pmatrix}\frac{1}{J_x}\tau_\phi\\ \frac{1}{J_y}\tau_\theta\\ \frac{1}{J_z}\tau_\psi\end{pmatrix}. \quad (4.39)$$

4.1.4 Resultant forces

The resulting forces acting in the HTR are divided into: Propulsion Force (X_p^b, Y_p^b, Z_p^b), Aerodynamic Force (X_a^b, Y_a^b, Z_a^b), and Gravity Force (X_g^b, Y_g^b, Z_g^b). These forces are

expressed as:

$$\begin{pmatrix} X^b \\ Y^b \\ Z^b \end{pmatrix} = \begin{pmatrix} X_p^b \\ Y_p^b \\ Z_p^b \end{pmatrix} + \begin{pmatrix} X_a^b \\ Y_a^b \\ Z_a^b \end{pmatrix} + \begin{pmatrix} X_g^b \\ Y_g^b \\ Z_g^b \end{pmatrix}. \tag{4.40}$$

4.1.4.1 Propulsion force

The propulsion force generated by each propulsion motor is the thrust that normally acts in a fixed direction relative to the body frame [130]. As presented by Santos [129], the propulsion force can be considered directly proportional to the command applied to the motors ($\delta_{1...6}$), as described by:

$$F_* = k_1 \delta_*, \tag{4.41}$$

where F represents the force produced by each propulsion motor, $k_1 = 7.81$ is the propulsion constant, characteristic of each propulsion mechanism, and δ_* is the command signal for each motor.

Examining the configuration of each propulsion motor:

$$\begin{pmatrix} X_p^b \\ Y_p^b \\ Z_p^b \end{pmatrix} = \begin{pmatrix} k_1 \sin\gamma_1 & k_1 \sin\gamma_2 & 0 & 0 & 0 & 0 \\ 0 & 0 & 0 & 0 & 0 & 0 \\ k_1 \cos\gamma_1 & k_1 \cos\gamma_2 & k_1 & k_1 & k_1 & k_1 \end{pmatrix} \begin{pmatrix} \delta_1 \\ \delta_2 \\ \delta_3 \\ \delta_4 \\ \delta_5 \\ \delta_6 \end{pmatrix}. \tag{4.42}$$

Due to the hexacopter configuration, γ_* represents the inclination angle of each servomotor (0 degrees has direction $-\hat{\boldsymbol{k}}^{\boldsymbol{b}}$). In addition, lateral force is also not generated directly due to the HTR's constructive characteristics.

4.1.4.2 Aerodynamic force

Aerodynamic forces acting on the HTR body structure are described as the product of non-dimensional aerodynamic coefficients and dimensional quantities. These coefficients can be derived using analytical methods and are influenced by several parameters, including the geometric aspects of the vehicle, which determine a drag coefficient (C_D), the angle of attack (α), the sideslip angle (β), and the dynamic pressure ($\bar{q}$) [129].

This gives us:

$$X_a^{\omega} = \bar{q} S C_D, \tag{4.43}$$

where X_a^{ω} is the drag force in the wind reference $\mathcal{F}^{\omega}$ and S represents the surface area generating the drag.

The UAV configuration is a multirotor, not a fixed-wing aircraft. Consequently, the lateral aerodynamic and drag forces are negligible. Thus:

$$C_D = \sum_i C_{D_{E_i}} E_i, \tag{4.44}$$

where E are the aerodynamic states.

From this, the aerodynamic forces are calculated in the wind frame ($\mathcal{F}^{\omega}$). Therefore, it is necessary to transform to the vehicle body frame ($\mathcal{F}^{b}$), given by:

$$\begin{pmatrix} X_a^b \\ Y_a^b \\ Z_a^b \end{pmatrix} = -\boldsymbol{R}_{\boldsymbol{b}}^{\boldsymbol{\omega}} \begin{pmatrix} \bar{q} S C_D \\ 0 \\ 0 \end{pmatrix}, \tag{4.45}$$

$$\begin{pmatrix} X_a^b \\ Y_a^b \\ Z_a^b \end{pmatrix} = - \begin{pmatrix} \cos\alpha\cos\beta & \sin\beta & \sin\alpha\cos\beta \\ -\sin\beta\cos\alpha & \cos\beta & -\sin\alpha\sin\beta \\ -\sin\alpha & 0 & \cos\alpha \end{pmatrix} \begin{pmatrix} \bar{q} S C_D \\ 0 \\ 0 \end{pmatrix}. \tag{4.46}$$

4.1.4.3 Gravity force

The gravitational force exerted on the HTR due to Earth gravitational field is proportional to the HTR mass and acts on its center of mass [125].

This force acts directed along the $\boldsymbol{k^i}$ axis, and is proportional to the HTR mass multiplied by the gravity constant g, similar to Equation4.23. Therefore:

$$\begin{pmatrix} X_g^i \\ Y_g^i \\ Z_g^i \end{pmatrix} = \begin{pmatrix} 0 \\ 0 \\ mg \end{pmatrix}. \tag{4.47}$$

Transforming this force into the body frame $\mathcal{F}^b$ from Equation 4.24:

$$\begin{pmatrix} X_g^b \\ Y_g^b \\ Z_g^b \end{pmatrix} = \boldsymbol{R_v^b} \begin{pmatrix} 0 \\ 0 \\ mg \end{pmatrix}, \tag{4.48}$$

$$\begin{pmatrix} X_g^b \\ Y_g^b \\ Z_g^b \end{pmatrix} = \begin{pmatrix} -mg\sin\theta \\ mg\cos\theta\sin\phi \\ mg\cos\theta\sin\phi \end{pmatrix}. \tag{4.49}$$

After describing the resultant forces acting on the hexacopter, the governing equations can be summarized as follows:

$$\begin{pmatrix} X^b \\ Y^b \\ Z^b \end{pmatrix} = \begin{pmatrix} k_1\sin\gamma_1 & k_1\sin\gamma_2 & 0 & 0 & 0 & 0 \\ 0 & 0 & 0 & 0 & 0 & 0 \\ k_1\cos\gamma_1 & k_1\cos\gamma_2 & k_1 & k_1 & k_1 & k_1 \end{pmatrix} \begin{pmatrix} \delta_1 \\ \delta_2 \\ \delta_3 \\ \delta_4 \\ \delta_5 \\ \delta_6 \end{pmatrix} - \boldsymbol{R_b^\omega} \begin{pmatrix} \bar{q}SC_D \\ 0 \\ 0 \end{pmatrix} + \begin{pmatrix} -mgs\theta \\ mgc\theta s\phi \\ mgc\theta c\phi \end{pmatrix}. \tag{4.50}$$

4.1.5 Resultant torques

The resulting torques acting on the HTR are divided into: Propulsion Torque (L_p^b, M_p^b, N_p^b), Aerodynamic Torque (L_a^b, M_a^b, N_a^b) and Gravity Torque (L_g^b, M_g^b, N_g^b), which are expressed as follows:

$$\begin{pmatrix} L^b \\ M^b \\ N^b \end{pmatrix} = \begin{pmatrix} L_p^b \\ M_p^b \\ N_p^b \end{pmatrix} + \begin{pmatrix} L_a^b \\ M_a^b \\ N_a^b \end{pmatrix} + \begin{pmatrix} L_g^b \\ M_g^b \\ N_g^b \end{pmatrix}. \tag{4.51}$$

To better comprehend the torques produced by the HTR six operating propulsion motors, it is crucial to understand the directions of rotation of each motor. Then, the propulsion motors with their respective directions of rotation are shown in Figure 4.8:

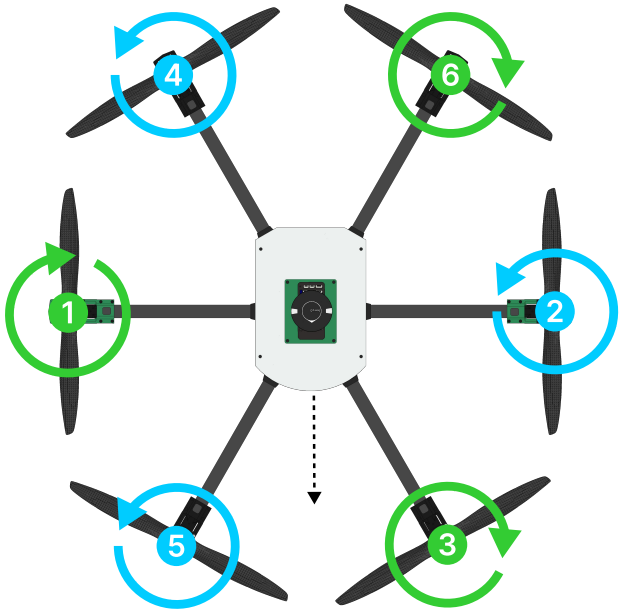

Figure 4.8: HTR with propulsion motors and respective rotation directions

Rotors 1, 3, and 6 (indicated in green spin) are in a clockwise direction, and rotors 2, 4, and 5 (indicated in blue spin) rotate in a counter-clockwise direction. Therefore, examining this configuration and order of each motor, the propulsion torques of the HTR rotors are given by:

$$\begin{pmatrix} L_p^b \\ M_p^b \\ N_p^b \end{pmatrix} = \begin{pmatrix} k_1 c\gamma_1 \ell - k_2 s\gamma_1 & -k_1 c\gamma_2 \ell + k_2 s\gamma_2 & k_1 \ell \frac{1}{2} & -k_1 \ell \frac{1}{2} & -k_1 \ell \frac{1}{2} & k_1 \ell \frac{1}{2} \\ 0 & 0 & k_1 \ell \frac{\sqrt{3}}{2} & -k_1 \ell \frac{\sqrt{3}}{2} & k_1 \ell \frac{\sqrt{3}}{2} & -k_1 \ell \frac{\sqrt{3}}{2} \\ -k_1 s\gamma_1 \ell - k_2 c\gamma_1 & k_1 s\gamma_2 \ell + k_2 c\gamma_2 & -k_2 & k_2 & k_2 & -k_2 \end{pmatrix} \begin{pmatrix} \delta_1 \\ \delta_2 \\ \delta_3 \\ \delta_4 \\ \delta_5 \\ \delta_6 \end{pmatrix}, \tag{4.52}$$

where, ℓ is the arm length between the respective propeller and the HTR Center of Gravity (CG), γ_* is the angle of inclination of each servomotor of the HTR, $k_2 = 0.00781$ is the propulsion reaction constant, and $s\gamma_j = \sin\gamma_j$ and $c\gamma_j = \cos\gamma_j$.

Because the hexacopter does not have support surfaces, the aerodynamic torques can be disregarded, as the HTR CG aligns with the aerodynamic center. Additionally, it is important to note that UAVs with a hexacopter configuration presents these forces as negligible [125].

Regarding the gravitational torque, as the gravitational force acts directly on the HTR CG, it does not produce any torque in the rigid body of the vehicle frame $\mathcal{F}^b$ [125].

4.1.6 Hexacopter Control Effectiveness Matrix

Considering the previously described forces and torques, the gravitational and aerodynamic forces are intrinsic to the HTR's characteristics. Therefore, the Virtual Control Action (VCA) are performed only by the propulsion forces and torques, which are directly associated with Real Control Action (RCA) [129]. Consequently, the hexacopter Control Effectiveness Matrix (CEM) is given by:

$$\begin{pmatrix} X_p^b \\ Z_p^b \\ L_p^b \\ M_p^b \\ N_p^b \end{pmatrix} = \begin{pmatrix} k_1 s\gamma_1 \delta_1 + k_1 s\gamma_2 \delta_2 \\ k_1 c\gamma_1 \delta_1 + k_1 c\gamma_2 \delta_2 + k_1(\delta_3 + \delta_4 + \delta_5 + \delta_6) \\ (k_1 c\gamma_1 \ell - k_2 s\gamma_1)\delta_1 + (-k_1 c\gamma_2 \ell + k_2 s\gamma_2)\delta_2 + k_1 \ell \frac{1}{2}(\delta_3 - \delta_4 - \delta_5 + \delta_6) \\ k_1 \ell \frac{\sqrt{3}}{2}(\delta_3 - \delta_4 + \delta_5 - \delta_6) \\ (-k_1 s\gamma_1 \ell - k_2 c\gamma_1)\delta_1 + (k_1 s\gamma_2 \ell + k_2 c\gamma_2)\delta_2 + k_2(-\delta_3 + \delta_4 + \delta_5 - \delta_6) \end{pmatrix}. \quad (4.53)$$

4.2 Extended Fast Control Allocation

A major challenge of nonlinear control strategies in unmanned systems is their high computational cost, which becomes particularly problematic for small, lightweight devices requiring real-time processing. The FCA method has emerged as a solution by reducing the complexity of nonlinear control through two parts: separation and mapping, allowing a more efficient and lightweight control allocation [129].

Generally, control allocation techniques are implemented through four primary methods: Direct Allocation, Pseudo-Inverse, Linear Programming, and Nonlinear Programming.

Direct Allocation methods demonstrate robustness by transforming continuous dynamic optimal control problems into a discrete form. This approach aims to find allocated parameters that preserve the direction of VCA, employing polynomial fitting techniques to derive the optimal solution over the specified interval. Various approaches, including the two-step method, are frequently used for polynomial fitting [131].

Pseudo-inverse methods, particularly those employing redistribution techniques, begin by solving the allocation problem without considering saturation constraints. Initially, control actions are assumed as unrestricted. If the solution exceeds actual control limits, the optimal vector is projected onto feasible boundaries. Subsequently, the unconstrained elements are recalculated using a reduced pseudo-inverse to minimize the difference between the desired and allocated control variables. This iterative process continues until a feasible solution is achieved [132].

Linear Programming focuses on minimizing the weighted error between the desired and estimated virtual control actions, transforming the problem into an optimization process with geometric or polyhedral constraints. This type of problem can be addressed using iterative numerical algorithms, such as the simplex method, through predefined cost functions [133]. In contrast, Nonlinear Programming guarantees a unique optimal solution if all weights in the cost function are strictly positive, employing slack variables to accommodate constraints [134].

In this context, this work uses an extension of the FCA technique, presented by Santos (2020) [129]. The choice of this technique is justified by its proven efficiency as a more optimized control allocation method. In this presented work, the FCA technique was adapted to incorporate the expanded configuration of the UAV, progressing from the original method for a Quadcopter Tilt-Rotor with four servomotors to a HTR with two servomotors. This adaptation alters the optimization process of the control allocation, ensuring efficient management of the additional DoFs maintaining the low computational cost.

The extended FCA technique divides the RCA into groups. This separation transforms the complex nonlinear problem into simpler linear subproblems. Then, mapping is applied to associate each virtual control action with its corresponding linear subproblem. This decomposition of the nonlinear control space into linear subspaces allows FCA providing a computationally efficient control allocation, including in resource-limited environments [129].

The stability of the FCA method was confirmed through previous rigorous analysis, demonstrating that the solutions converge and remain within acceptable ranges throughout the control allocation process. The FCA effectiveness is further evidenced by its ability to handle different system configurations, ensuring that the VCAs are accurately mapped to their corresponding linear subproblems. This approach guarantees robust and reliable system operation, even under challenging conditions with limited resources. The combination of stability, efficiency, and adaptability positions FCA as a promising solution for over-actuated systems.

Additionally, the objective of the FCA technique is to transform the nonlinear control allocation into a faster linear version, transforming VCA into RCA. So, the proposed extension is hereafter formulated. First, the nonlinear system is described by Equation 4.54:

$$\hat{\boldsymbol{\tau}} = \boldsymbol{M}(\boldsymbol{u}), \tag{4.54}$$

where $\boldsymbol{M}$ is the CEM presented in Equation 4.53, $\hat{\boldsymbol{\tau}}$ and $\boldsymbol{u}$ are the VCA and RCA vectors, respectively.

This control allocation method provides new linear spaces from a nonlinear space, allowing the nonlinear system to be broken into two different problems, as shown in Equation 4.55 and 4.56:

$$\hat{\boldsymbol{\tau}}_{\boldsymbol{a}} = \boldsymbol{M}_{\boldsymbol{a}}(\boldsymbol{u}_{\boldsymbol{b}})\boldsymbol{u}'_{\boldsymbol{a}}, \tag{4.55}$$

$$\hat{\boldsymbol{\tau}}_{\boldsymbol{b}} = \boldsymbol{M}_{\boldsymbol{b}}(\boldsymbol{u}_{\boldsymbol{a}})\boldsymbol{u}_{\boldsymbol{b}}, \tag{4.56}$$

where, $\boldsymbol{u}_{\boldsymbol{a}} \in \mathbb{R}^q$, with $q \in \mathbb{N}^*$ being a part of the n actuators of the system, $\boldsymbol{u}_{\boldsymbol{b}} \in \mathbb{R}^r$, with $r \in \mathbb{N}^*$ being the rest of the actuators, $\hat{\boldsymbol{\tau}}_{\boldsymbol{a}} \in \mathbb{R}^{ma}$, $\hat{\boldsymbol{\tau}}_{\boldsymbol{b}} \in \mathbb{R}^{mb}$ with $m \in \mathbb{N}^*$ being the number of DoFs in RCA, $\boldsymbol{M}_{\boldsymbol{a}}(\boldsymbol{u}_{\boldsymbol{a}}) \in \mathbb{R}^{ma \times q}$ and $\boldsymbol{M}_{\boldsymbol{b}}(\boldsymbol{u}_{\boldsymbol{b}}) \in \mathbb{R}^{mb \times r}$.

To apply the FCA technique to the HTR and minimize the linearization process between nonlinear and linear expressions, the extended approach consists of separating these terms into distinct groups, fully superposed: nonlinear terms in $\boldsymbol{u}_{\boldsymbol{a}}$, and linear terms in $\boldsymbol{u}_{\boldsymbol{b}}$. These terms are represented by $\sin\gamma_i$ and δ_i, respectively. From this, Equation 4.57 is obtained:

$$\boldsymbol{u}'_{\boldsymbol{a}} \in \mathbb{R}^3 = (\sin(\gamma_1), \sin(\gamma_2), 1)^T, \tag{4.57}$$

In this formulation, the value 1 is responsible for the sum of all terms related to cos. This choice consolidates and allows nonlinearities to be represented as internal constants.

The advantage of this method consists in acting as a normalization factor. Also, since $\boldsymbol{u_a}$ is derived from the system, it allows adjustments to be made so that the value can deviate from 1 when necessary.

This normalization method allows the entire vector $\boldsymbol{u_a^{'}}$ to be adjusted to ensure that the final term remains equal to 1. Equation 4.58 demonstrates how this adaptation facilitates the use of RCA to operate the aircraft servomotors with genuine control signals:

$$\boldsymbol{u_a} \in \mathbb{R}^2 = (\sin^{-}(\gamma_1), \sin^{-}(\gamma_2))^T. \tag{4.58}$$

For the second group of RCA, the linear terms (δ_i) representing the thruster rotations are organized by Equation 4.59:

$$\boldsymbol{u_b} \in \mathbb{R}^6 = (\delta_1, \delta_2, \delta_3, \delta_4, \delta_5, \delta_6)^T. \tag{4.59}$$

The next step in the system's design is the selection of two groups of VCA: $\boldsymbol{\tau_a}$ and $\boldsymbol{\tau_b}$. For this purpose, the configuration of the total VCA superposition between the two sets was adopted [135]. Consequently, $\boldsymbol{M_a(u_a)} \in \mathbb{R}^{2\times6}$ and $\boldsymbol{M_b(u_b)} \in \mathbb{R}^{5\times6}$ are described by the Equations 4.60 and 4.61:

$$\hat{\boldsymbol{\tau}}_{\boldsymbol{a}} = (X_p^b, N_p^b)^T, \tag{4.60}$$

$$\hat{\boldsymbol{\tau}}_{\boldsymbol{b}} = (X_p^b, Z_p^b, L_p^b, M_p^b, N_p^b)^T. \tag{4.61}$$

The choice of terms X_p^b and N_p^b for the first VCA subgroup is justified by their role in stabilizing the vehicle orientation, given that they are directly controlled by the action set $\boldsymbol{u_a}$. Subsequently, the remaining virtual variables are allocated to the group $\boldsymbol{u_b}$. Equations 4.62 and 4.63 show the corresponding subgroups:

$$\overbrace{\begin{pmatrix} X_p^b \\ N_p^b \end{pmatrix}}^{\hat{\boldsymbol{\tau}}_b} = \overbrace{\begin{pmatrix} k_1\delta_1 & k_1\delta_2 & 0 \\ -k_1 l\delta_1 & k_1 l\delta_2 & -k_2\delta_3 + k_2\delta_4 + k_2\delta_5 - k_2\delta_6 - k_2 c\gamma_1\delta_1 + k_2 c\gamma_2\delta_2 \end{pmatrix}}^{\boldsymbol{M_a(u_a^-, u_b)}} \begin{pmatrix} s\gamma_1 \\ s\gamma_2 \\ 1 \end{pmatrix}, \quad (4.62)$$

$$\overbrace{\begin{pmatrix} X_p^b \\ Z_p^b \\ L_p^b \\ M_p^b \\ N_p^b \end{pmatrix}}^{\hat{\boldsymbol{\tau}}_a} = \overbrace{\begin{pmatrix} k_1 s\gamma_1 & k_1 s\gamma_2 & 0 & 0 & 0 & 0 \\ k_1 c\gamma_1 & k_1 c\gamma_2 & k_1 & k_1 & k_1 & k_1 \\ k_1 c\gamma_1 l - k_2 s\gamma_1 & -k_1 c\gamma_2 l + k_2 s\gamma_2 & k_1 l\frac{1}{2} & -k_1 l\frac{1}{2} & -k_1 l\frac{1}{2} & k_1 l\frac{1}{2} \\ 0 & 0 & k_1 l\frac{\sqrt{3}}{2} & -k_1 l\frac{\sqrt{3}}{2} & k_1 l\frac{\sqrt{3}}{2} & -k_1 l\frac{\sqrt{3}}{2} \\ -k_1 s\gamma_1 l - k_2 c\gamma_1 & +k_1 s\gamma_2 l + k_2 c\gamma_2 & -k_2 & k_2 & k_2 & -k_2 \end{pmatrix}}^{\boldsymbol{M_b(u_a)}} \overbrace{\begin{pmatrix} \delta_1 \\ \delta_2 \\ \delta_3 \\ \delta_4 \\ \delta_5 \\ \delta_6 \end{pmatrix}}^{\boldsymbol{u_b}}. \quad (4.63)$$

4.3 Control structure

For a successful UAVs development, several steps are crucial, such as comparing mathematical modeling and the real system, as well as the implementation of control methods to ensure stability and safety in extreme operating situations, including mechanical failures. This allows the vehicle to operate smoothly and harmoniously, and for this, it is important to use the control technique to operate in an agile and structured procedure [136].

The next step, after accurately modeling the hexacopter and defining the control allocation method to be used, is to determine the controller's structure. This leads to the introduction of the PID controller, a widely used control algorithm that satisfies essential requirements such as stability, good transient response, steady-state performance, and robustness to noise and disturbances. It consists of three components: P, I, and D.

This arrangement allows the control action to minimize error through the proportional component, eliminate steady-state error through the integral component, and improve system stability by predicting future error through the derivative component [137], [138].

From this widely recognized configuration, several control techniques have been developed for UAV applications, as described in Section 3.1. Among these approaches, the choice of the most appropriate technique depends on several factors, such as the aircraft characteristics, its complexity, the operating environment, and performance requirements.

A notable controller configuration, which is employed in this presented work, is the cascade P-PID topology, chosen due to its ability to refine the dynamic response by leveraging the strengths of the integral and derivative components, which improve both precision and stability. This controller combines different controllers in a hierarchical structure to achieve more refined control. This configuration allows for faster and more precise responses compared to a standalone PID, offering greater flexibility in adjusting parameters to meet the demands of different system components.

Due to its ability to provide more precise control over key variables, the cascade configuration was employed in this presented work. Figure 4.9 shows the control structure schematically:

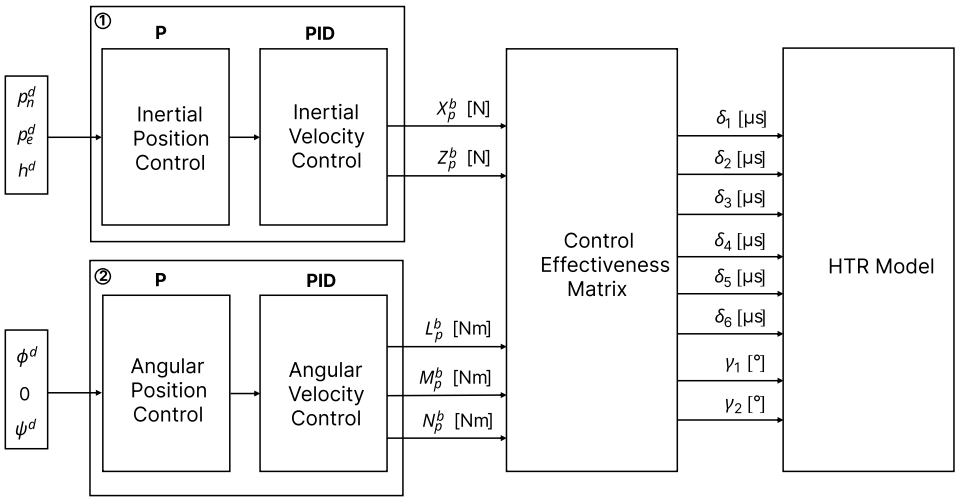

Figure 4.9: HTR overall control structure

Considering the figure, the upper-level control structure includes position and velocity inertial controllers and was implemented using two levels of cascaded closed-loop control: an external and an internal level. The external level includes a P controller for inertial position, while the internal level consists of a PID controller for inertial velocity. This results in a cascaded P-PID configuration.

The external controller is responsible for maintaining the inertial position, specifically controlling altitude (h) and north and east position (p_n) and (p_e), respectively. The P controller was adopted for its capability to fast response to changes and its efficiency, while the PID controller was adopted for its easy implementation. Figure 4.10 details the structure of these control loops:

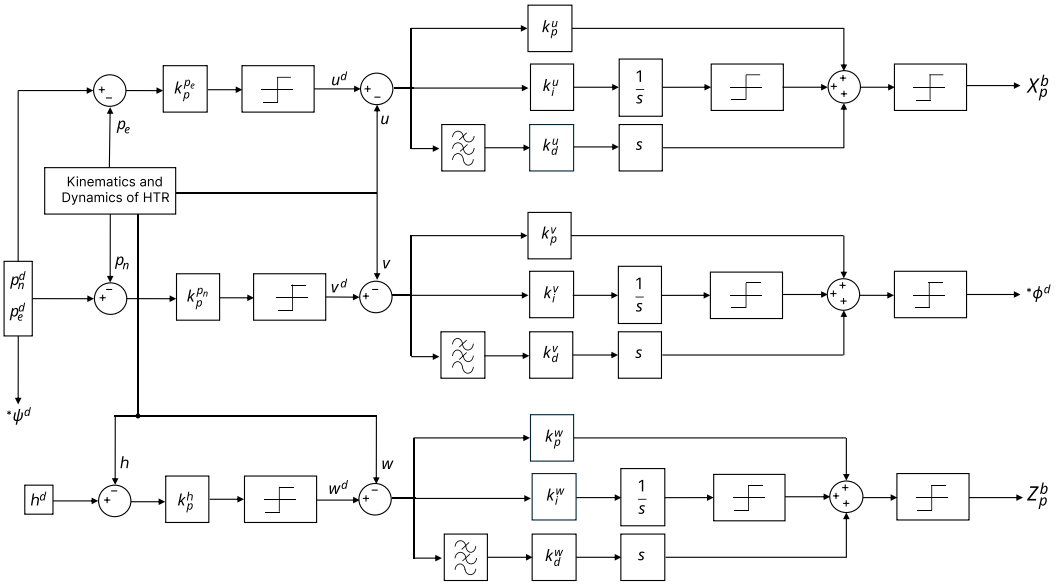

Figure 4.10: HTR high-level control structure

As illustrated, the P controller is used to control the inertial position, and its output is the input to the subsequent PID controller, which manages the inertial velocity. Two outputs of this control level, X_p^b and Z_p^b, represent the required forces to be applied to the CEM to generate the control actions.

In addition, the roll and yaw SP are generated based on the position east (p_e) and north (p_n) through the Line of Sight (LOS) method. According to Kingston and Beard

(2007), this approach ensures the HTR follows the desired trajectory by calculating the appropriate orientation (ϕ^d and ψ^d) to align the aircraft with the target path [139]. Using lateral and longitudinal positions, the HTR ensures precise path following.

Since direct lateral force control is unavailable in this configuration, lateral motion is indirectly achieved by generating a roll SP. At the same time, the desired heading (yaw SP) is derived from east and north positions SPs, ensuring correct orientation throughout the aircraft movement.

At the lower level, the angular position and velocity controllers are illustrated, which perform a fundamental function in the control of angular stability through roll (ϕ), pitch (θ), and yaw (ψ) angles. Similarly to the upper level, two cascaded loops are implemented: an external and an internal loop. The external loop represents angular position control using an P controller, while the internal loop performs angular velocity control employing an PID controller. Figure 4.11 provides a detailed block diagram of these control loops:

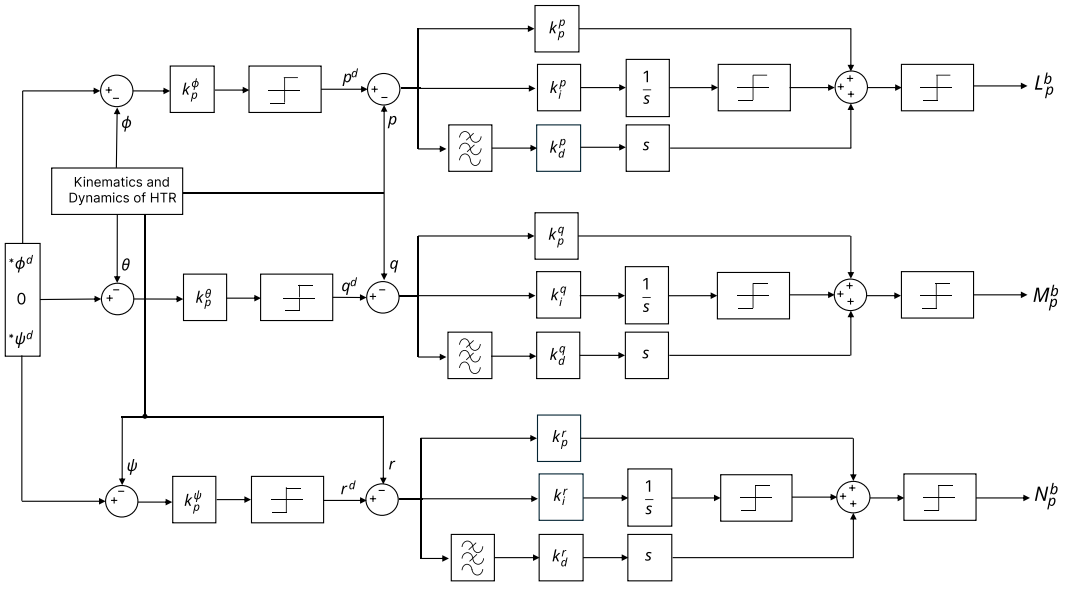

Figure 4.11: HTR low-level control structure

The outputs from the angular velocity control level, L_p^b, M_p^b, and N_p^b, represent the desired roll, pitch, and yaw torques in the body-fixed frame, which are then used in the HTR CEM to generate appropriate control actions. Moreover, it is important to note that

the pitch SP is set to zero due to the unique hexacopter arrangement, where servomotors are responsible for tilting to compensate for pitch movements, ensuring stability and precision in the control system.

The controller tuning was performed based on the linear model using the methodology proposed by Beard and McLain (2012) [125] and Santos, Honório, Moreira, *et al.* (2021) [71], ensuring a robust technique for the system performance. Accordingly, Table 4.1 summarizes the P-PID controller gains. These values, designed and optimized based on the discussed methodology, offer an effective solution for all 5 aircraft controlled DoFs.

Table 4.1: P-PID controller gains obtained for HTR

Variable	**P**		
p_n	$k_p^n = 0.949$		
p_e	$k_p^e = 0.949$		
h	$k_p^h = 2.000$		
ϕ	$k_p^\phi = 5.500$		
θ	$k_p^\theta = 6.500$		
ψ	$k_p^\psi = 5.270$		
	P	**I**	**D**
u	$k_p^u = 3.000$	$k_i^u = 0.440$	$k_d^u = 0.100$
v	$k_p^v = 3.000$	$k_i^v = 0.440$	$k_d^v = 0.100$
w	$k_p^w = 4.000$	$k_i^w = 2.000$	$k_d^w = 0.100$
p	$k_p^p = 0.138$	$k_i^p = 0.181$	$k_d^p = 0.002$
q	$k_p^q = 0.142$	$k_i^q = 0.189$	$k_d^q = 0.003$
r	$k_p^r = 0.181$	$k_i^r = 0.186$	$k_d^r = 0.003$

4.4 System architecture

For this proposed work, an algorithm was developed and implemented in Python using the tools presented previously: PX4 Autopilot, Gazebo software, and ROS 1 Noetic. These

tools provide together a versatile virtual environment for validating the control algorithm and applying the extended FCA approach.

Communication between the Gazebo simulator, the HTR, ROS, and the PX4 Autopilot control system is conducted through the MAVLink protocol. MAVLink, a lightweight messaging protocol, facilitates communication between the UAV and the control systems by using a hybrid standard that combines both publish-subscribe and point-to-point communication methods [140]. MAVROS serves as a bridge between ROS and MAVLink, enabling the integration and efficient exchange of sensor data and control commands among these components. Figure 4.12 illustrates the communication architecture:

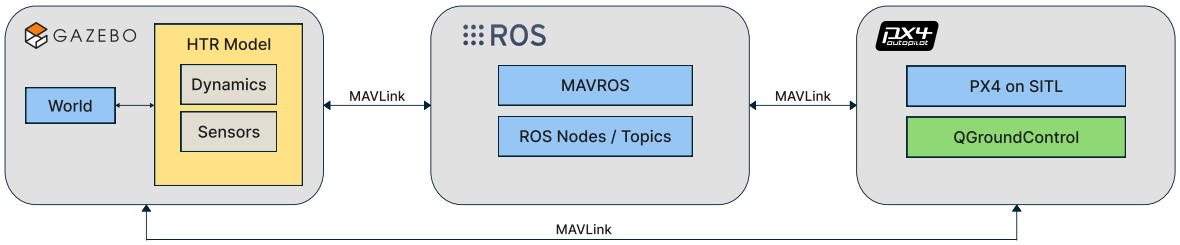

Figure 4.12: Representation of the communication architecture used

This communication architecture was selected for its flexibility and efficiency, facilitating the rapid development and testing of control algorithms in a virtual environment before real-world implementation. Additionally, the modularity of ROS and Gazebo enabled easy integration of over-actuation functionalities into the PX4 base code.

Based on this understanding, the first step of the system architecture involves generating Waypoint (WP), which represents the coordinate of interest that the HTR will follow. These points are obtained using QGroundControl, a widely used mission planning software compatible with the PX4 Autopilot. These WPs are defined in alignment with the mission goals, which, in this context, pertain to PA applications such as monitoring a vineyard to collect environmental data. The purpose of this stage is to provide a sequence of strategic positions to ensure complete coverage of the area of interest.

Once the WP have been defined, the algorithm begins processing by uploading the missions to the HTR. Using MAVROS as a direct communication layer between PX4 and HTR implemented in Gazebo world, the WP are transmitted to the vehicle via MAVLink protocol. This process ensures that the hexacopter flight controller is correctly configured and synchronized with the planned mission points.

Subsequently, the aircraft loads all WP, processes, and stores data, which can be accessed via topics such as */mission/* to read, validate, and clear the WP. Following this, the TAKE_OFF command is sent to the HTR, which generates the position SP and initiates the pre-flight check procedure. After successfully completing the pre-flight checks, the hexacopter activates the thrusters and takes off to a predetermined altitude. From there, the position and velocity SP are dynamically adjusted as the vehicle approaches each WPs.

Throughout the mission execution, PX4 continuously executes the control actions, as described in Section 4.3, to maintain trajectory, altitude, and stability in real time during the mission. Meanwhile, the RCAs are monitored in real time to ensure that the HTR is operating correctly. In addition, variables are constantly monitored in topics, such as */local_position/pose*, which provides the vehicle position and orientation, */local_position/velocity_local*, which monitors velocity, and */imu/data*, which monitors the hexacopter attitude variables.

Once all WPs have been covered, the HTR begins landing, using the LAND command or, alternatively, the RETURN TO LAUNCH (RTL) command to return to its home position. In the contrary case, the aircraft continues the mission by processing the next WPs until all points have been visited, and the mission is concluded.

Figure 4.13 illustrates the architecture of ROS used in this work, highlighting the primary topics and nodes used during the mission:

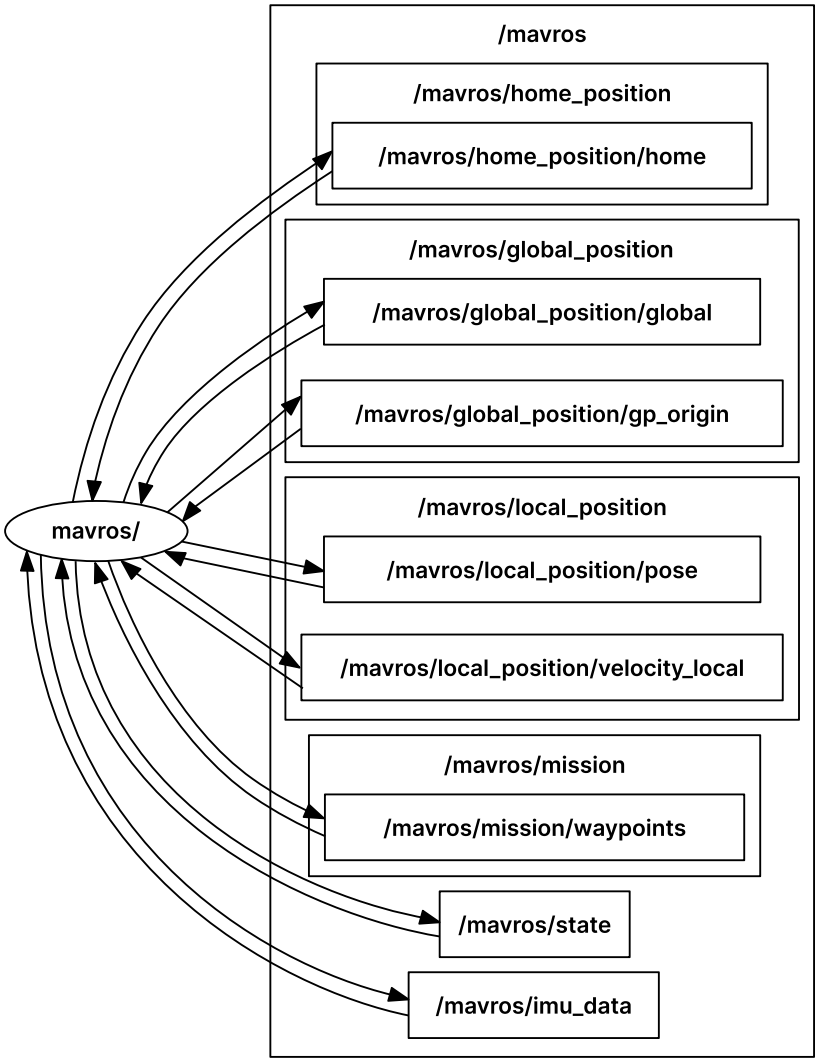

Figure 4.13: Representation of the ROS topics and nodes used

To ensure an effective analysis, this assessment was performed in a simulated environment within the Gazebo software. The simulation was implemented using SITL, a useful methodology and good practice for developing robots and algorithms before deploying code on physical robotic systems. The use of Gazebo software allows for the replication of the described HTR with its respective dynamic characteristics and the desired scenarios, with multiple object models and libraries.

Furthermore, to simulate the HTR's performance, the dynamics of an existing PX4

model, the Typhoon H480, were adapted to the Gazebo environment. This hexacopter model was selected due to its compatibility with PX4, allowing physical and visual modifications (such as collisions, visuals, sensors, and actuators) that enabled the tiltrotors implementation of the modeled HTR configuration. This approach allowed for the simulation of the HTR dynamic characteristics and to modify the control parameters and flight algorithms. Figure 4.14 shows the HTR with the implemented tiltrotors from two perspectives:

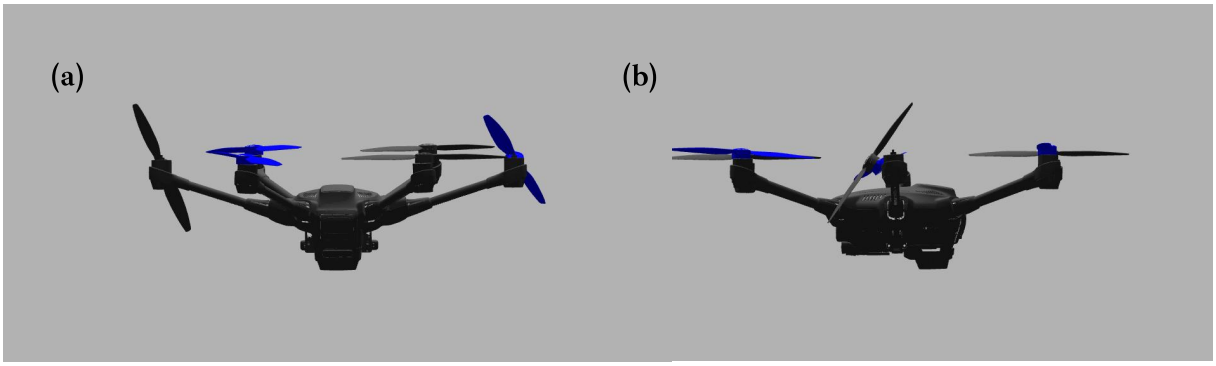

Figure 4.14: Hexacopter used in Gazebo

Table 4.2 presents the parameters used in the simulations conducted with the HTR's flight dynamics:

Table 4.2: HTR parameters used in Gazebo

Parameter	**Description**	**Value**	**Units**
m	Mass	1.5	kg
g	Gravity	9.81	m/s^2
d	Motor to mass center distance	0.25	m
k_1	Propulsion force produced	7.81	N
k_2	Propulsion reaction constant	0.00781	N
J_x	Moment of inertia	0.0411	kgm^2
J_y	Moment of inertia	0.0478	kgm^2
J_z	Moment of inertia	0.0599	kgm^2

It is also important to mention that the simulation was performed using an 11th generation 2.40GHz Intel(R) Core i5-1135G7 device with 16 GB of RAM, a 64-bit Ubuntu 20.04 operating system and ROS 1 Noetic, and an Intel(R) Iris(R) Xe Graphics.

Chapter 5

Results

This chapter aims to present the results obtained from simulations and analyze the HTR's controllers responses in association with the FCA control allocation method. To validate the developed aircraft, three scenarios were conducted:

- **First scenario (Section 5.1)**: examines the response of the HTR following a linear trajectory in an open field to evaluate the effectiveness of the implemented controllers;
- **Second scenario (Section 5.2)**: demonstrates the HTR response in a vineyard, assessing its performance in a PA environment;
- **Third scenario (Section 5.3)**: evaluates the HTR in the vineyard, following a different flight path to cover the plantation using an alternative trajectory.

It is notable to mention that in all scenarios, the vehicle begins with a yaw angle of 89°, where 0° is aligned to the North.

To provide a more precise measure of the HTR trajectory, Mean Squared Error (MSE) was applied to quantifying and comparing differences between the presented and desired responses, providing insights regarding the accuracy and stability of the aircraft. The MSE is given by Equation 5.1:

$$MSE = \frac{1}{n}\sum_{i=1}^{n}(y_i - \hat{y}_i)^2. \tag{5.1}$$

In addition, to further validate the response of the HTR, it is compared with the Typhoon H480 hexacopter, chosen due to its compatibility with the PX4 Autopilot. The Typhoon H480 is simulated using its original dynamic parameters in Gazebo software, allowing for a direct comparison. From this point forward, this hexacopter will be referred to as the "traditional hexacopter" to simplify references.

The purpose of this comparison is to evaluate the effectiveness of the control strategies implemented for the HTR as well as the performance of the extended FCA method in contrast to the traditional control approaches used in the reference hexacopter.

5.1 Scenario 1 - Open field 1

For the first scenario, a linear path was generated, assuming the takeoff of the HTR, a straight-line flight (approximately 35 meters), and landing. This flight was conducted at the Polytechnic Institute of Bragança coordinates (41.796080°N, −6.767043°W), Portugal. Figure 5.1 provides an aerial view:

Figure 5.1: HTR flight path in open field

This location was selected for its safe and controlled environment, ensuring ideal conditions for the HTR operation and guaranteeing an accurate assessment of the control system's performance throughout the mission before its deployment in the PA application. The open field is near a vineyard (indicated by a red "X").

Figure 5.2 illustrates this location implemented in Gazebo world, using real-world coordinates:

Figure 5.2: HTR flight path in Gazebo

The altitude variable (h), linear velocity (V_x), and attitude angles (ϕ, θ, and ψ) are analyzed to validate the stability and precision of the proposed system. Additionally, the performance of the actuators is evaluated, including the control signals sent to the six motors and the two tiltrotors.

Figure 5.3 shows the five controlled responses: altitude (h), linear velocity (V_x), roll (ϕ), pitch (θ), and yaw (ψ), respectively:

It is noted that the aircraft successfully reached the desired altitude dynamics. The HTR starts from a static position, and after taking off, it ascends to the desired altitude. Around $t = 10s$, the HTR initiates linear movement, and towards $t = 18s$, the velocity decreases as the landing process begins. Then, the landing is gradual, with a slightly longer duration to ensure enhanced safety. No overshoots were perceived.

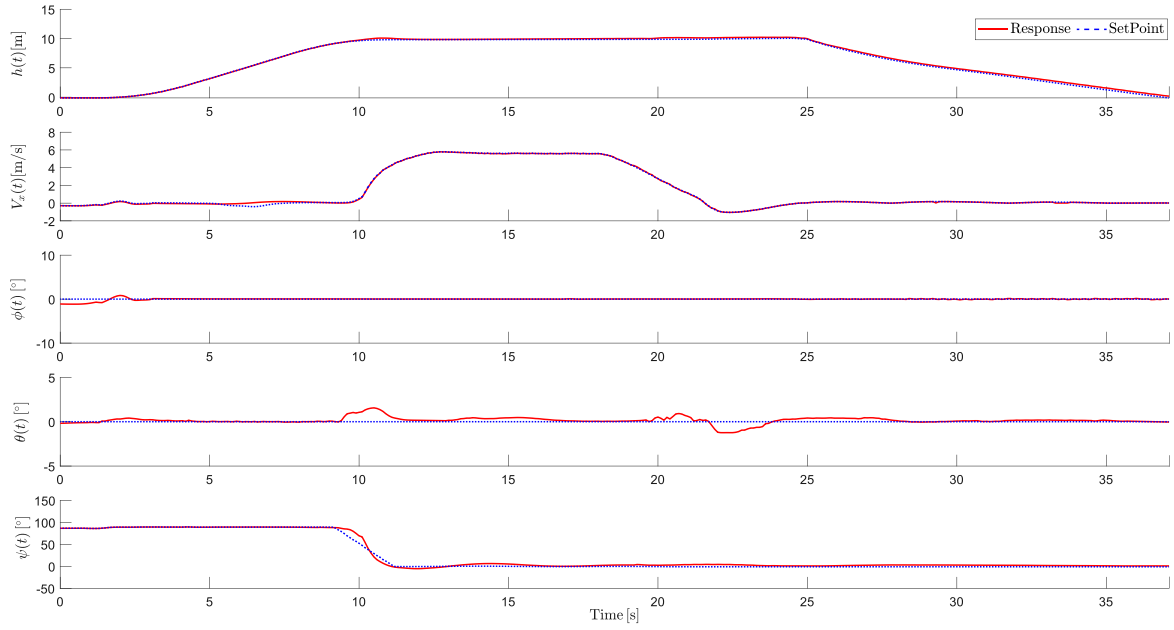

Figure 5.3: Controlled responses of altitude (h), velocity (V_x), roll (ϕ), pitch (θ) and yaw (ψ)

Furthermore, roll and yaw angles exhibited minimal variations, consistent with the planned trajectory conditions. Minor control fluctuations were observed at the beginning of the roll response, which is related to the soil effect. However, the system maintained stability and quickly corrected minor disturbances. It is also important to highlight that the pitch response remained close to zero, with minor oscillations due to control actions, showing maximum deviations of $\pm 1.2°$. It's explained by the servomotors tilting angles when forward displacements are done.

Figure 5.4 shows the RCA responses of the vehicle during the simulation:

The motors exhibited the expected response throughout the simulated trajectory. Minor oscillations were observed when the aircraft reached the desired altitude during takeoff and when approaching the waypoint before landing. In addition, during the tiltrotor adjustments, motor oscillations were observed because tilting the motors 1 and 2 slightly reduces the total lift, requiring the remaining RCA to compensate. In response, the other motors temporarily increased their thrust to balance the lift loss.

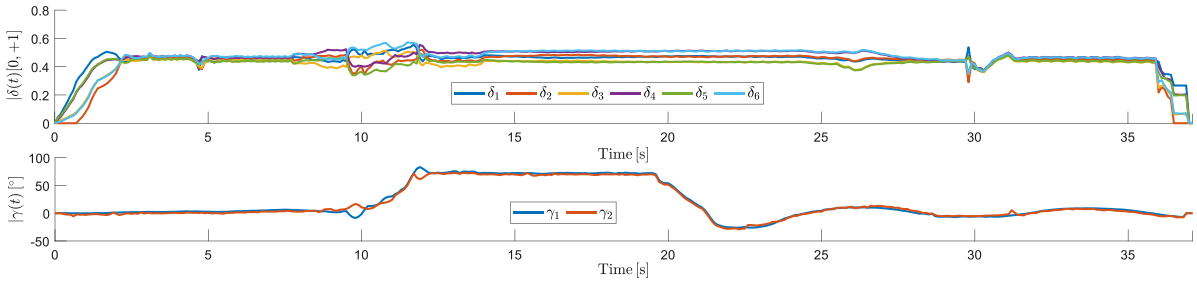

Figure 5.4: RCAs of HTR: Responses from thrust motors (δ_i) and servomotors (γ_i)

It is also notable that during yaw maneuvers, the tilt directions were opposite. After reaching an altitude of 10 meters, they tilted to approximately 70° and maintained this angle during the linear movement. Upon reaching the landing point, a negative tilt angle was applied to decelerate the HTR, ensuring a controlled reduction in velocity. Subsequently, the tiltrotors gradually retracted to their neutral positions, allowing a smooth landing.

Figure 5.5 illustrates the trajectory of the aircraft in a three-dimensional graphic:

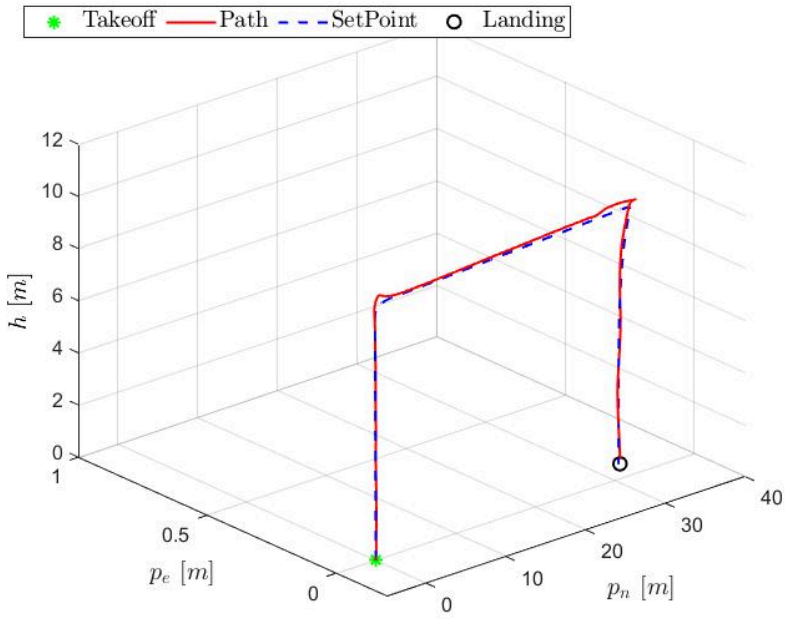

Figure 5.5: HTR three-dimensional path

As observed, the aircraft followed the planned path with precision. The HTR executed both takeoff and landing as expected, validating the effectiveness of the implemented control system. For this, the trajectory metrics are presented in Table 5.1, taking MSE into account:

Table 5.1: MSE obtained for inertial controlled response from Figure 5.5

Variable	p_n	p_e	h
MSE	0.01923	0.0085	0.0294

To validate the responses of the HTR in this scenario, Figure 5.6 shows the comparative responses for the proposed HTR and the traditional hexacopter:

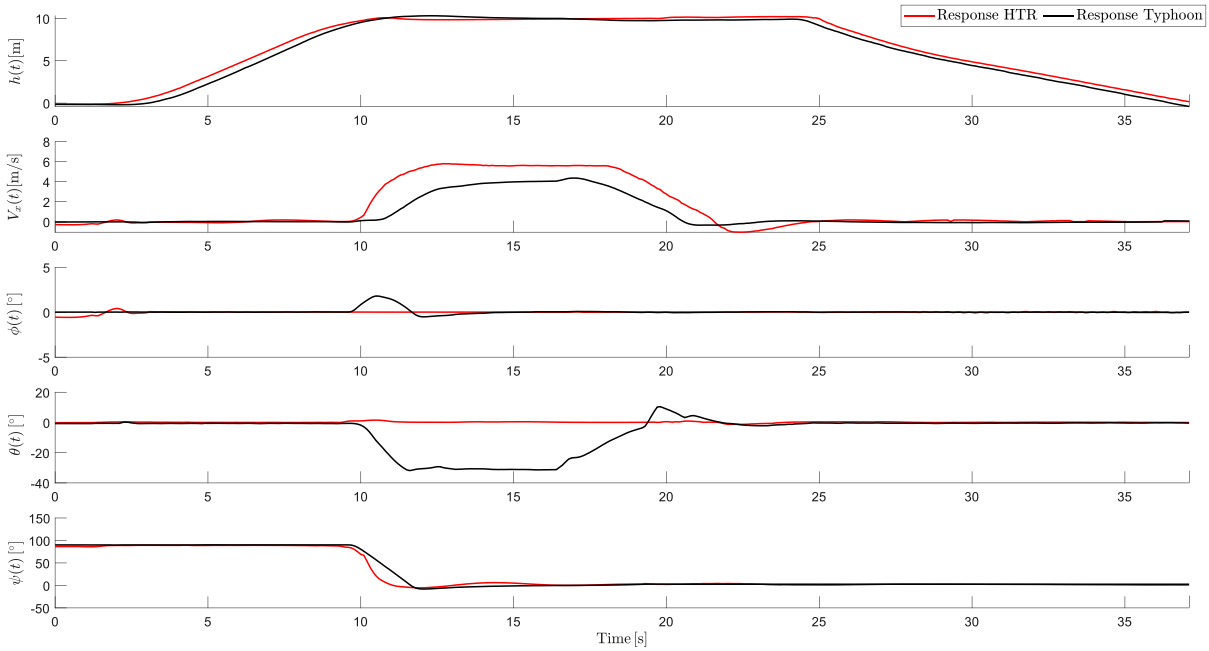

Figure 5.6: Comparative responses between HTR and traditional hexacopter

As evident, the comparison highlights several key performance differences between the two aircraft. In terms of altitude, both vehicles demonstrated stable performance during takeoff, linear movement, and landing, with minimal oscillations. The mean altitude of

the HTR in the linear movement was 10.0102m, compared to 9.9472m for the traditional one.

Additionally, the proposed HTR achieved a higher maximum linear velocity (5.6m/s) compared to the traditional one (4.3m/s), a difference of 32.97%. This result emphasizes the efficiency of the HTR in covering distances, maintaining 0 degrees of pitch throughout the trajectory, with angles of $\pm 1.2°$. In contrast, the traditional hexacopter relied on forward pitching (around $-31°$) to generate linear movement.

Regarding yaw control, the HTR exhibited a faster yaw response compared to the traditional model, enhancing its agility in maneuvers. This improved response time allows for more efficient displacements in this scenario compared to conventional aircraft.

Figure 5.7 illustrates the trajectory of both aircraft in a three-dimensional graphic for a better comparison of the flight paths taken by both aircraft:

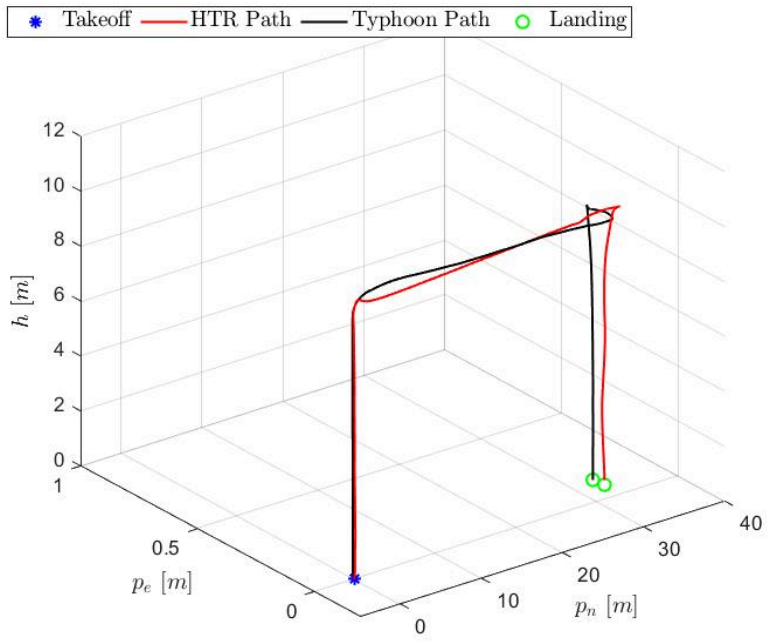

Figure 5.7: HTR and traditional hexacopter three-dimensional path

This comparison also demonstrates the superior performance of the HTR, which completed the flight path with greater stability. However, due to its higher velocity, the

aircraft slightly overshot the landing point. In contrast, the traditional hexacopter exhibited a lateral deviation to the left before landing, which may be attributed to pitch adjustments to generate linear velocity.

5.2 Scenario 2 - Open field 2

For this scenario, a trajectory was generated for PA applications focused on monitoring a vineyard at an altitude of 5 meters. This flight was conducted at the Polytechnic Institute of Bragança coordinates (41.796420°N, −6.767929°W), Portugal. Figure 5.1 provides an aerial view:

Figure 5.8: HTR second flight path in open field

This location was selected to provide a real-world agricultural environment, enabling accurate measurement of the control system performance across the vineyard. Figure 5.9 shows an aerial view of this area within the Gazebo world:

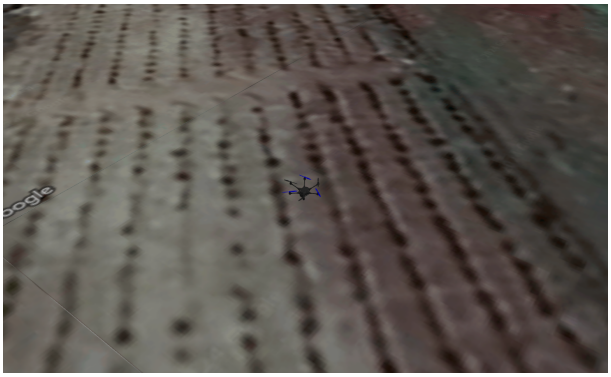

Figure 5.9: HTR second flight path in Gazebo world

To validate the HTR performance in this scenario, the altitude variable (h), linear velocity (V_x), and attitude angles (ϕ, θ, and ψ) are analyzed. Figure 5.10 shows the five controlled responses: altitude (h), linear velocity (V_x), roll (ϕ), pitch (θ), and yaw (ψ), respectively, across the flight path over the vineyard.

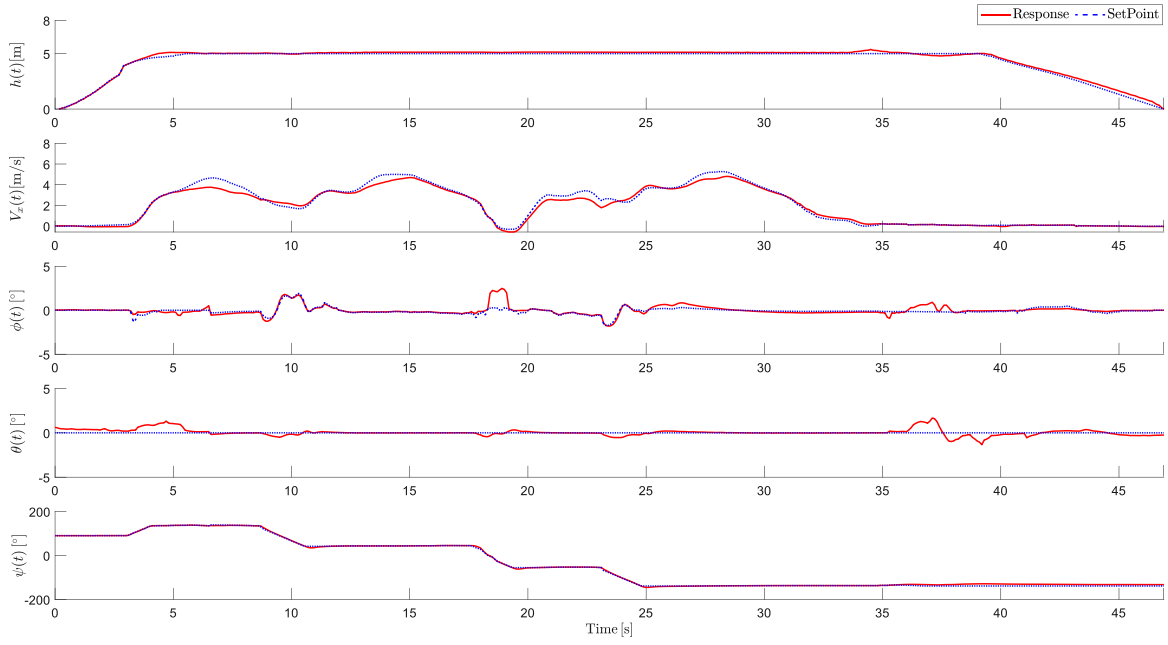

Figure 5.10: Controlled responses of altitude (h), velocity (V_x), roll (ϕ), pitch (θ) and yaw (ψ)

It is observed that the aircraft successfully achieves the target altitude after takeoff. The HTR starts from a static position, and after taking off, it ascends to the desired altitude, maintaining a heading of 89°. Between $t = 3s$ and $t = 5s$, the HTR initiates its first turn, as evidenced by changes in roll and yaw. During this maneuver, a small pitch oscillation is observed, showing a maximum deviation of 1.1°, which enables the aircraft to adjust its trajectory and achieve the desired velocity.

Between $t = 13s$ and $t = 16s$, the aircraft performs another turn, resulting in changes in roll and yaw angles. As the HTR orientation shifts more drastically during this interval compared to the earlier interval, the variations in roll are particularly pronounced. Despite this, the pitch deviation remains minimal, staying less than 0.5°. This indicates that the HTR successfully maintained a nearly zero pitch.

In the next interval, between $t = 18s$ and $t = 20s$, the HTR slightly exceeds the linear velocity SP, demonstrating the aircraft quick response. The other control variables remain close to their respective SP, indicating steady and reliable performance.

In the next interval, between $t = 18s$ and $t = 20s$, the HTR experienced a more significant adjustment in roll, reaching an angle of 2.3° to execute a turn, requiring a higher roll angle to maintain the desired trajectory. Despite this momentary increase in roll, the control system quickly stabilized the aircraft.

Between $t = 23s$ and $t = 25s$, the aircraft executes another turn, again with pronounced deviations in roll. However, both yaw and pitch remain close to their respective SPs, maintaining vehicle stability, with the pitch staying near zero degrees.

Finally, after $t = 35s$, the landing procedure begins as the aircraft reaches the landing point. During this phase, more significant corrections in the aircraft orientation are observed, although all variables remain within acceptable limits. Notably, the pitch varies between 1.6° and $-1.3°$ to adjust the deceleration of the aircraft as it approaches the landing point.

Figure 5.11 shows the RCA responses of the vehicle during the simulation:

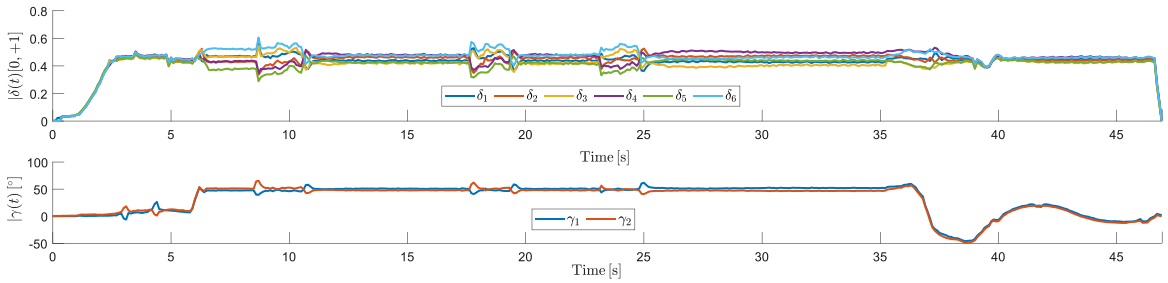

Figure 5.11: RCAs of HTR: Responses from thrust motors (δ_i) and servomotors (γ_i)

As observed, the motors exhibited the expected responses throughout the simulated flight. Minor oscillations can be observed at both the takeoff and landing points; other notable variations occur during turn movements and tiltrotors adjustments. In addition, motor oscillations were noted during tiltrotor adjustments. This occurs because tilting the motors 1 and 2 slightly reduces the total lift, requiring the remaining RCA to compensate. In response, the other motors temporarily increased their thrust to balance the loss of lift. Other small differences can be observed at both the takeoff and landing points.

Additionally, the tiltrotor responses are notable. During the straight-line segments, they tilted approximately 45°, maintaining this angle during linear movement. In addition, some variations occurred at specific intervals, particularly during yaw maneuvers, where opposing tilt orientations were observed.

After $t = 35s$, a significant adjustment occurred. Upon reaching the landing point, the servomotors tilted $-36°$ to decelerate the HTR, ensuring a controlled reduction in velocity. Following this, the tiltrotors gradually retracted to their neutral position, allowing a soft landing.

Figure 5.12 presents the three-dimensional trajectory of the aircraft, providing a comprehensive view of the path:

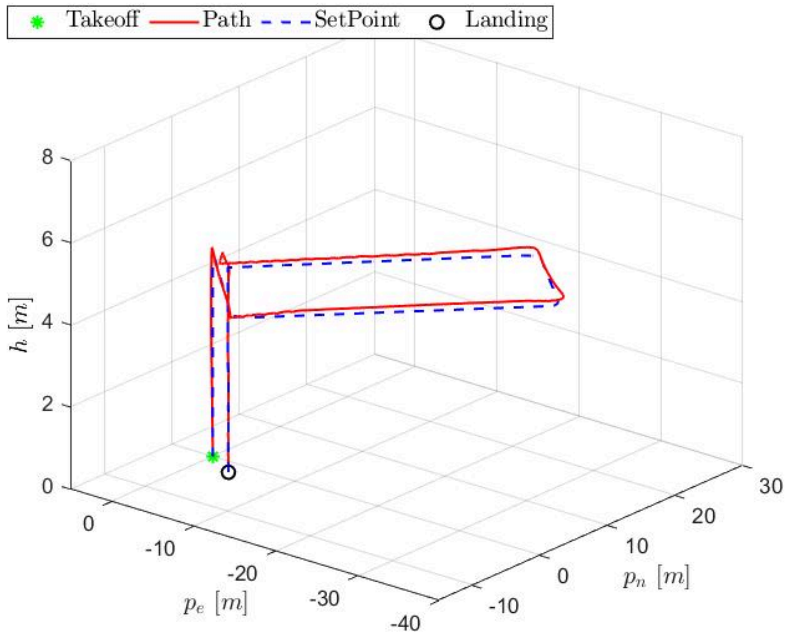

Figure 5.12: HTR three-dimensional path

As shown, the HTR successfully executed the takeoff and landing as expected and performed both linear and curve movements with accuracy. To confirm this, trajectory variables (p_n, p_e, h) are presented in Table 5.2, taking MSE into account:

Table 5.2: MSE obtained for inertial controlled response from Figure 5.12

Variable	p_n	p_e	h
MSE	0.0786	0.0793	0.0212

To validate the responses of the HTR in the second scenario, Figure 5.13 shows the comparative responses for both aircraft:

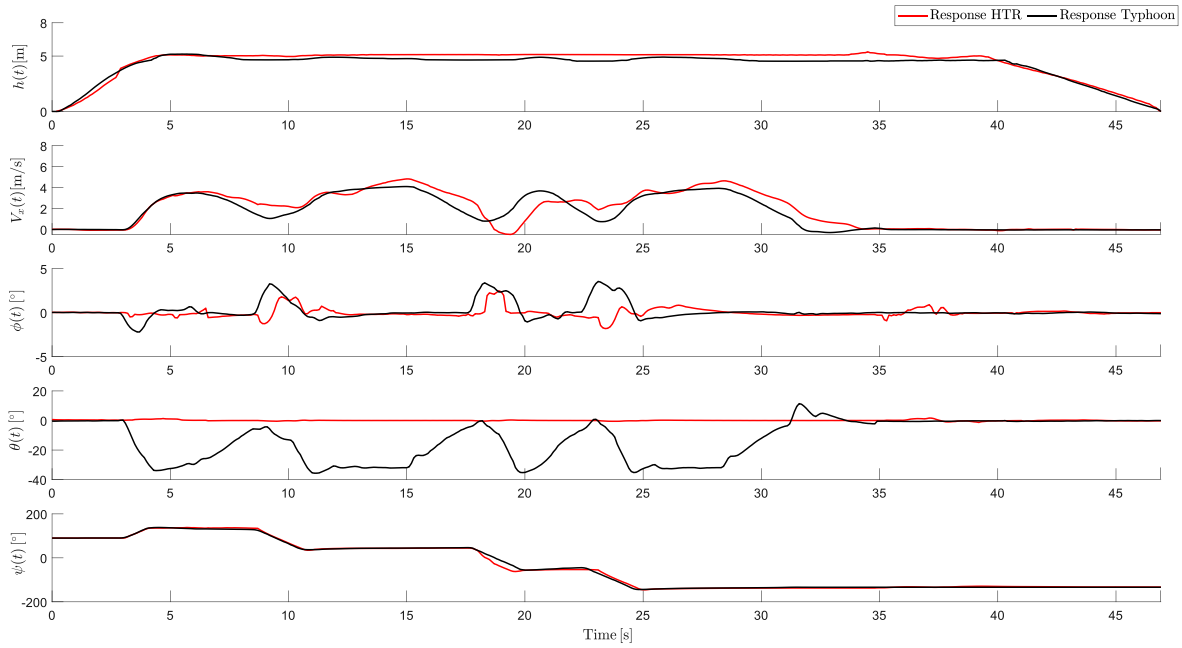

Figure 5.13: Comparative responses between HTR and traditional hexacopter

Several important points can be noted from this comparison. In terms of altitude, both vehicles demonstrated stable performance during takeoff, linear movement, and landing, with minimal oscillations. During straight line movement, the HTR responds closely to the SP, maintaining an altitude mean of 5.1043m. In contrast, the traditional hexacopter stabilizes at around 4.7m, with variations down to 4.3m and an altitude mean of 4.7320m.

Regarding the linear velocity, the proposed HTR achieved a higher maximum linear velocity throughout the trajectory (4.8340m/s) compared to the traditional hexacopter (4.1030m/s). This is particularly evident in the second graph, where it is observed a difference of 17.77% in the linear velocity.

In addition, the traditional hexacopter higher roll angles, with oscillations between 4° and −2.4°. In terms of pitch, the traditional hexacopter relied on forward pitching (around −33°) to generate linear movement. In contrast, the HTR maintained its pitch angle near zero throughout the flight. In yaw, both systems demonstrated similar responses throughout the flight.

Figure 5.7 illustrates the trajectory of both aircraft in a three-dimensional graphic to highlight each trajectory:

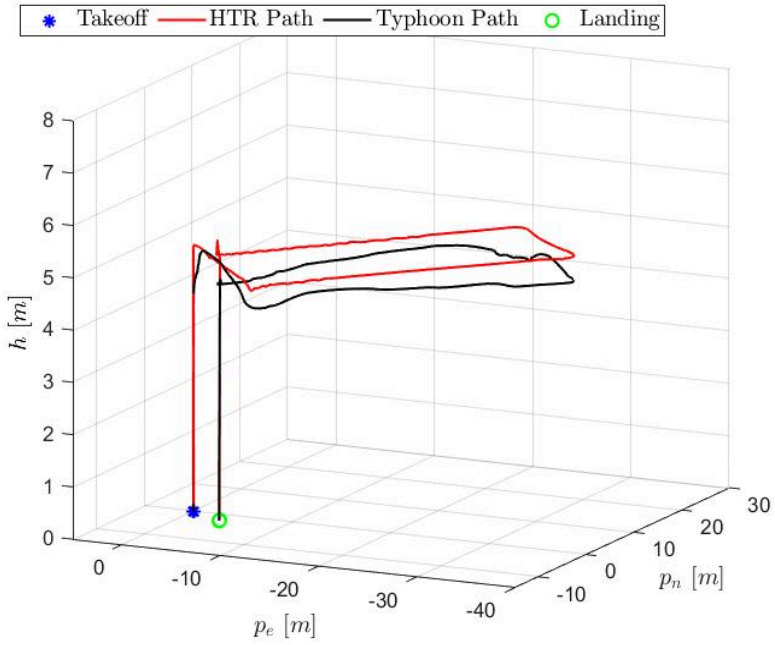

Figure 5.14: HTR and traditional hexacopter three-dimensional path

This demonstrates that the HTR achieves a more linear flight with minimal oscillations. In contrast, the traditional hexacopter consistently flew below the desired altitude throughout the flight and exhibited more oscillations during turn intervals.

5.3 Scenario 3 - Open field 3

For the third scenario, a more complex trajectory was generated to operate similar to the previous scenario, with more coverage of the area. This flight was conducted using the same coordinates as Scenario 2 (41.796420°N, −6.767929°W). Figure 5.15 provides an aerial view:

Figure 5.15: HTR third flight path in open field

This location was chosen to simulate the practical use of the HTR in a real-world PA scenario, where precise navigation over crops is crucial for efficient operations such as disease detection. Figure 5.9 shows this area in Gazebo world.

In this scenario, the investigation focuses on the same essential variables: altitude (h), linear velocity (V_x), and the attitude angles (ϕ, θ, and ψ), which are essential for assessing the aircraft response. Figure 5.16 shows the responses of these variables:

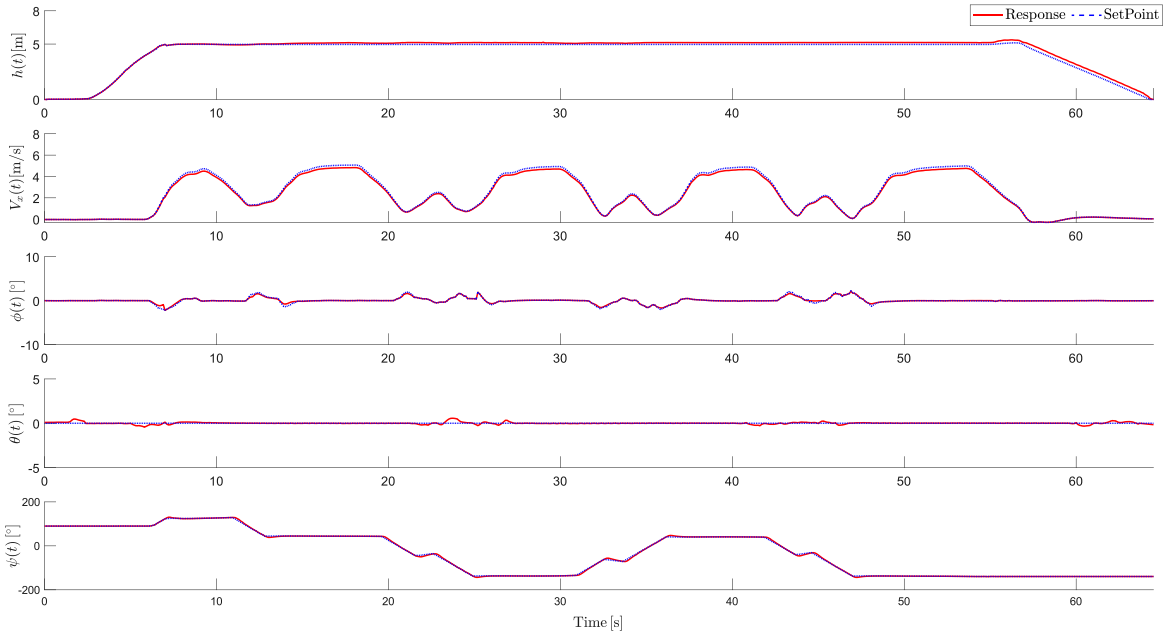

Figure 5.16: Controlled responses of altitude (h), velocity (V_x), roll (ϕ), pitch (θ) and yaw (ψ)

The graphics showed that the HTR demonstrated a response closely aligned with the SPs, with altitude stabilized at the desired value, indicating its capability to maintain precise navigation covering this area.

During the entire flight, the linear velocity followed the SP with minor oscillations due to controller corrections to adjusting other dynamic variables. These deviations are expected, given the characteristics of the coupled variables within the system.

Regarding attitude variables, the HTR was subjected to more changes in roll and yaw due to the curves present in the flight path, leading to increased fluctuations in these variables. The roll angles remained relatively low and close to the SP, indicating the HTR ability to perform maneuvers without significant deviations. In contrast, the pitch remained close to zero, which aligns with the expected performance since the tiltrotors are responsible for this control function. Also, yaw had more changes due to the HTR's nose adjustments, required to follow the trajectory, confirming the efficiency of the system

in maintaining the correct heading throughout the flight.

As a result, Figure 5.17 illustrates the RCA responses of the aircraft along the flight path:

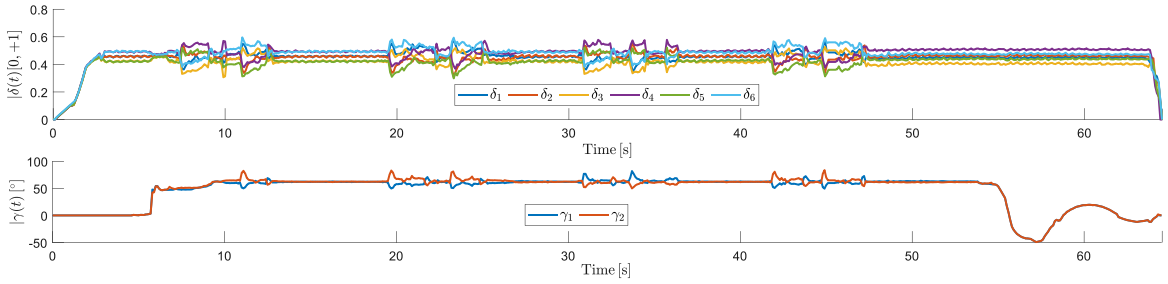

Figure 5.17: RCAs of HTR: Response from thrust motors (δ_i) and servomotors (γ_i)

This figure illustrates that the propulsion motors demonstrated the expected responses throughout the flight, with notable variations occurring during turn movements and tiltrotors adjustments. This occurs because tilting the motors 1 and 2 slightly decreases the total lift, necessitating the remaining RCA to compensate. The other motors temporarily increased their thrust to balance the lift loss. Other small differences can be observed in both the takeoff and landing points. Throughout the flight, the six motors operated at an average of 54.39% of their maximum rotation capacity, ensuring stable performance during demanding maneuvers.

During straight-line segments, the tiltrotors maintain an angle of approximately 56° to keep the HTR with zero pitch for forward movement. In addition, during yaw maneuvers, opposing tilt angles were observed for the servomotors 1 and 2, enabling controlled orientation adjustments of the HTR without compromising system stability. Throughout takeoff, the tiltrotors begin in a neutral position and progressively increase their angles to achieve the desired velocity. Upon landing, the tiltrotors gradually transitioned to negative angles, effectively reducing the HTR velocity as it approached the landing point.

Figure 5.18 presents the HTR trajectory in a three-dimensional graphic to provide a clearer understanding of the aircraft response:

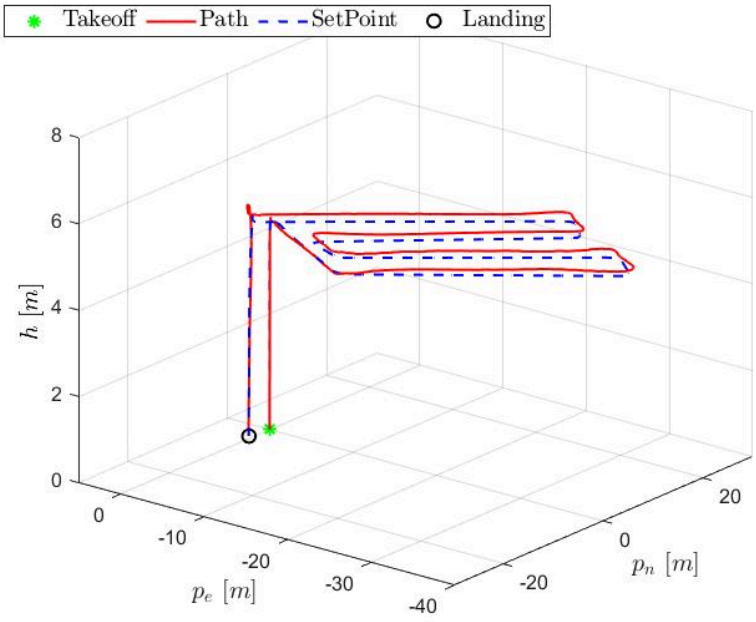

Figure 5.18: HTR three-dimensional path

As illustrated, the HTR followed the designated path with high precision. Also, the HTR successfully executed the takeoff and landing stages, demonstrating accurate performance during both linear and curve movements. To confirm this, trajectory variables (p_n, p_e, h) are presented in Table 5.3, taking MSE into account:

Table 5.3: MSE obtained for inertial controlled response from Figure 5.18

Variable	p_n	p_e	h
MSE	0.0389	0.0536	0.0275

To validate the responses of the HTR in the scenario, Figure 5.19 illustrates the comparative responses for both aircraft:

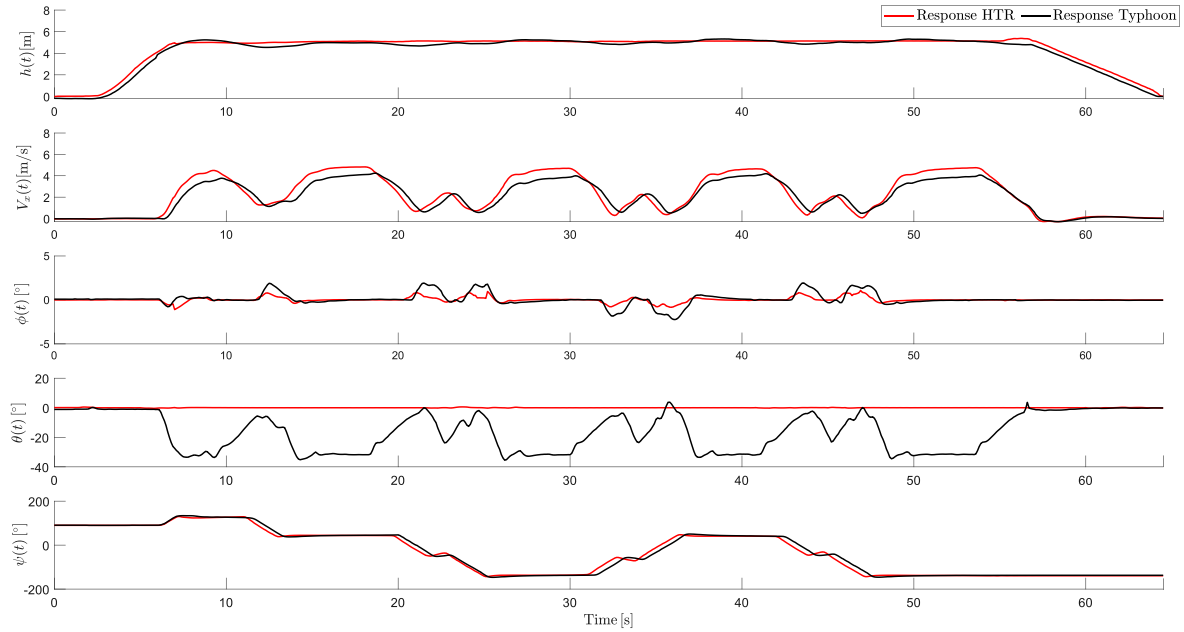

Figure 5.19: Comparative responses between HTR and traditional hexacopter

Several key points can be discussed from this comparison between the two hexacopters. In terms of altitude, both vehicles demonstrated stable performance during takeoff, linear movement, and landing, with minimal oscillations. The mean altitude of the HTR in linear movement was 5.1038m. In contrast, the traditional hexacopter showed more variations, reaching a peak of 5.3227m and 4.5419m, with an altitude mean of 5.0080m.

Regarding the linear velocity, the proposed HTR achieved a higher maximum linear velocity throughout the trajectory (4.8293m/s) compared to the traditional hexacopter (4.2431m/s). This is evident in the second graph, where it is observed a difference of 13.82% in the linear velocity.

In terms of attitude, the HTR exhibited a higher roll angle during the first orientation adjustment at $t = 6s$. In contrast, in the following instants, the traditional hexacopter displayed higher roll angles. The difference in pitch is particularly notable due to the HTR efficiency in covering distances, maintaining 0 degrees of pitch throughout the trajectory, with angles of $\pm 0.5°$. In contrast, the traditional hexacopter relied on forward pitching

(around $-30°$) to generate linear movement. In terms of yaw, both hexacopters performed similar responses in this scenario.

Figure 5.20 illustrates the flight paths of both aircraft in a three-dimensional graph, allowing a clearer illustration of the performance comparison:

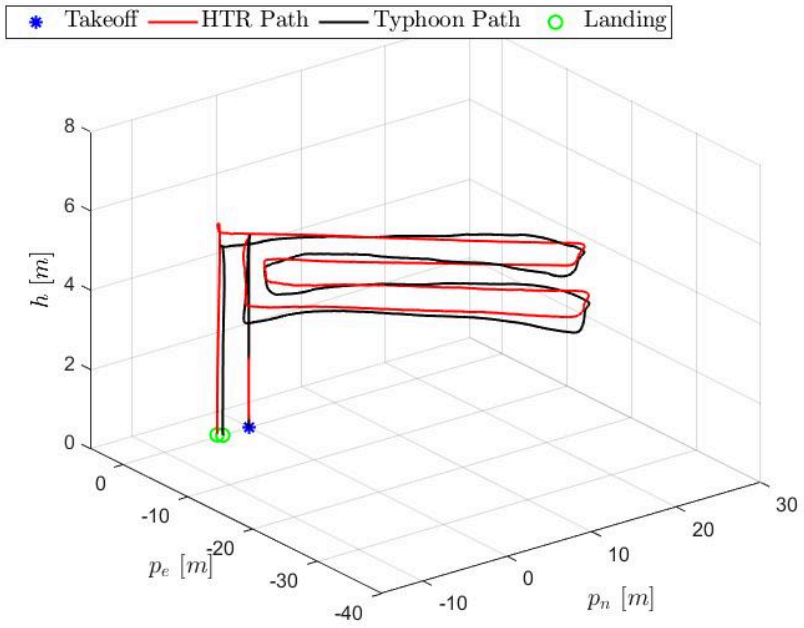

Figure 5.20: HTR and traditional hexacopter three-dimensional path

This analysis indicates that the HTR achieved a more linear flight path, with only a slight overshoot during landing. In contrast, the traditional hexacopter presents more oscillations, particularly during the turn movements. Additionally, a minor difference in the landing points between the two aircraft can be observed.

This comparison highlights the superior performance of the HTR, which completed the flight path with greater stability. These results validated the control implemented on the HTR and demonstrated its ability to keep zero pitch and high efficiency, showcasing its capability to manage complex trajectories, and suggest that this vehicle could serve as an excellent alternative for PA applications.

Chapter 6

Conclusions and Future Works

This chapter presents the conclusions obtained from this work. The main conclusions are focused on the performance of the proposed HTR configuration, emphasizing its behavior in simulated environments and the effectiveness of the implemented control system. Additionally, the potential application of the HTR in PA is evaluated. Furthermore, future work that can be achieved with this developed system is presented, and the academic contributions made during this investigation are highlighted.

6.1 Conclusions

This work was divided into six main stages:

- Kinematic and dynamic modeling of the proposed HTR;
- Implementation of the HTR in simulated virtual environment in Gazebo;
- Development and integration with ROS;
- Design, tuning, and implementation of the control loops;
- Development of the extended version of FCA technique;
- Experimental simulations for vehicle validations.

In the first stage, the kinematic and dynamic modeling of the HTR was successfully completed. This was a crucial step for the implementation of the vehicle in the virtual simulation environment of Gazebo. These simulations in different scenarios were essential to validate the proposed vehicle performance, especially in PA scenarios.

Additionally, the integration with the ROS proved to be a crucial factor in ensuring the system's scalability and providing a modular and efficient environment. This integration facilitated communication between sensors and controllers and autonomous navigation algorithms, ensuring functional interactions within the system.

The control loops designed with the proposed topology were also effective in maintaining stability and maneuverability across the proposed scenarios. The extended version of the FCA control allocation technique demonstrated promising results to allocate the VCA to the RCA in a more optimized form. This provided better performance compared to the traditional configuration.

The experimental simulations demonstrated that a stable and functional HTR efficiently followed the proposed trajectories, proving to be a promising innovative approach for areas such as PA. With the growing demand for automated solutions and collaborative robots for complex tasks, the HTR offers a highly adaptable platform. The modular architecture of the aircraft allows the integration of computer vision techniques, enabling detailed crop monitoring, disease detection, and highly efficient harvest optimization.

However, it is important to highlight that this modeled HTR has a limitation of the use of nonlinear control allocation, which was strictly designed for the use of FCA.

6.2 Future Works

For future work, following the successful implementation of the control method and the application of the control allocation technique, several promising avenues for future research emerge. Approaches such as the development and integration of new control methodologies, including fault-tolerant control strategies, to increase system robustness in the event of faults.

Another potential direction is the physical construction and implementation of the HTR in real-world PA open-field tests, in cooperation with other collaborative robots, to perform crop monitoring and pest detection missions with computer vision. In addition, another approach is to explore alternative control allocation techniques, and investigating the performance of the HTR with a more varied set of subsystems could further optimize its efficiency and versatility.

6.3 Academic contributions

The following are the main contributions resulting from my research work during my master's degree. Three articles were developed, one of which was accepted and presented at a relevant event in this work area:

> **Pimentel, G. O.**, Santos, M.F., and Lima, J. L., "Autonomous Navigation of Unmanned Aerial Vehicle in Software in the Loop", *4th Symposium of Applied Science for Young Researchers - SASYR*. Bragança, Instituto Politécnico, 2024.

The second paper has been submitted to a international journal and was accepted:

> **Pimentel, G. O.**, Santos, M.F., and Lima, J. L., "An Over-Actuated Hexacopter Tilt-Rotor UAV Prototype for Agriculture of Precision: Modeling and Control", *Sensors*, 2024.

Lastly, a third paper, not directly related to the main focus of this work, was also accepted and presented:

> **Pimentel, G. O.**, Dessanti, A. L., and Teixeira, J. P., "A Comparative Analysis of MATLAB and Python Neural Networks for Diabetes Prediction", *OL2A 2024 - International Conference on Optimization, Learning Algorithms and Applications*, 2024.

Bibliography

[1] M. Hanzla, S. Ali, and A. Jalal, "Smart traffic monitoring through drone images via yolov5 and kalman filter," in *2024 5th International Conference on Advancements in Computational Sciences (ICACS)*, IEEE, 2024, pp. 1–8.

[2] H. Huang and A. V. Savkin, "Path planning for a solar-powered uav inspecting mountain sites for safety and rescue," *Energies*, vol. 14, no. 7, 2021, ISSN: 1996-1073. DOI: 10.3390/en14071968.

[3] A. Dhruva, R. J. L. Hartley, T. A. N. Redpath, H. J. C. Estarija, D. Cajes, and P. D. Massam, "Effective uav photogrammetry for forest management: New insights on side overlap and flight parameters," *Forests*, vol. 15, no. 12, 2024, ISSN: 1999-4907. DOI: 10.3390/f15122135.

[4] Y. Cao, F. Qi, Y. Jing, *et al.*, "Mission chain driven unmanned aerial vehicle swarms cooperation for the search and rescue of outdoor injured human targets," *Drones*, vol. 6, no. 6, 2022, ISSN: 2504-446X. DOI: 10.3390/drones6060138.

[5] A. Salam, M. Mohamed, R. Yong, and J. Ye, "A robust decision-making model for medical supplies via selecting appropriate unmanned aerial vehicle," *Neutrosophic Systems with Applications*, vol. 18, pp. 14–30, 2024.

[6] F. P. Leme, "Sistema embarcado para controle de plataforma de dois eixos utilizada em veiculos aereos nao tripulados," *UNICAMP*, 2017.

[7] P. Matyas and N. Mate, "Brief history of uav development," *Repulestudomanyi Kozlemenyek*, vol. 31, no. 1, pp. 155–166, 2019.

[8] P. K. Garg, *Unmanned aerial vehicles: An introduction*. Mercury Learning and Information, 2021.

[9] S. L. H. Cavallaro, "Modelagem, simulação e controle de vant do tipo quadricóptero," *USP*, 2019.

[10] R. Evers and P. Masters, "The application of low-altitude near-infrared aerial photography for detecting clandestine burials using a uav and low-cost unmodified digital camera," *Forensic science international*, vol. 289, pp. 408–418, 2018.

[11] G. S. Berger, A. O. Júnior, J. Braun, *et al.*, "Sensorial testbed for high-voltage tower inspection with uavs," in *ROBOT2022: Fifth Iberian Robotics Conference*, D. Tardioli, V. Matellán, G. Heredia, M. F. Silva, and L. Marques, Eds., Cham: Springer International Publishing, 2023, pp. 353–364, ISBN: 978-3-031-21062-4.

[12] V. M. Leal Lopes, L. M. Honório, M. F. Santos, *et al.*, "Design of an over-actuated hexacopter tilt-rotor for landing and coupling in power transmission lines," 6, vol. 7, 2023. DOI: 10.3390/drones7060341.

[13] G. M. Bolla, M. Casagrande, A. Comazzetto, *et al.*, "Aria: Air pollutants monitoring using uavs," in *2018 5th IEEE International Workshop on Metrology for AeroSpace (MetroAeroSpace)*, 2018, pp. 225–229. DOI: 10.1109/MetroAeroSpace.2018.8453584.

[14] K. Nihei, N. Kai, Y. Maruyama, *et al.*, "Forest fire surveillance using live video streaming from uav via multiple lte networks," in *2022 IEEE 19th Annual Consumer Communications Networking Conference (CCNC)*, 2022, pp. 465–468. DOI: 10.1109/CCNC49033.2022.9700621.

[15] J. Dong, K. Ota, and M. Dong, "Uav-based real-time survivor detection system in post-disaster search and rescue operations," *IEEE Journal on Miniaturization for Air and Space Systems*, vol. 2, no. 4, pp. 209–219, 2021.

[16] T. Noguchi and Y. Komiya, "Persistent cooperative monitoring system of disaster areas using uav networks," in *2019 IEEE SmartWorld, Ubiquitous Intelligence Computing, Advanced Trusted Computing, Scalable Computing Communications, Cloud Big Data Computing, Internet of People and Smart City Innovation (SmartWorld/SCALCOM/UIC/ATC/CBDCom/IOP/SCI)*, 2019, pp. 1595–1600. DOI: 10.1109/SmartWorld-UIC-ATC-SCALCOM-IOP-SCI.2019.00285.

[17] B. Hiebert, E. Nouvet, V. Jeyabalan, and L. Donelle, "The application of drones in healthcare and health-related services in north america: A scoping review," *Drones*, vol. 4, no. 3, p. 30, 2020.

[18] F. Outay, H. A. Mengash, and M. Adnan, "Applications of unmanned aerial vehicle (uav) in road safety, traffic and highway infrastructure management: Recent advances and challenges," *Transportation research part A: policy and practice*, vol. 141, pp. 116–129, 2020.

[19] Z. Yang, X. Yu, S. Dedman, *et al.*, "Uav remote sensing applications in marine monitoring: Knowledge visualization and review," *Science of The Total Environment*, vol. 838, p. 155 939, 2022.

[20] D. Popescu, F. Stoican, G. Stamatescu, L. Ichim, and C. Dragana, "Advanced uav–wsn system for intelligent monitoring in precision agriculture," *Sensors*, vol. 20, no. 3, p. 817, 2020.

[21] R. Chaurasia and V. Mohindru, "Unmanned aerial vehicle (uav): A comprehensive survey," *Unmanned Aerial Vehicles for Internet of Things (IoT) Concepts, Techniques, and Applications*, pp. 1–27, 2021.

[22] O. Sami Oubbati, M. Atiquzzaman, T. Ahamed Ahanger, and A. Ibrahim, "Softwarization of uav networks: A survey of applications and future trends," *IEEE Access*, vol. 8, pp. 98 073–98 125, 2020. DOI: 10.1109/ACCESS.2020.2994494.

[23] S. Michaelides-Mateou, "Challenges and trends in the aviation industry: Integrating uavs in non-segregated airspace," *Unmanned Aerial Vehicles Applications: Challenges and Trends*, pp. 377–409, 2023.

[24] A. Monteiro, S. Santos, and P. Gonçalves, "Precision agriculture for crop and livestock farming—brief review," *Animals*, vol. 11, no. 8, 2021, ISSN: 2076-2615. DOI: 10.3390/ani11082345.

[25] M. F. Aslan, A. Durdu, K. Sabanci, E. Ropelewska, and S. S. Gültekin, "A comprehensive survey of the recent studies with uav for precision agriculture in open fields and greenhouses," *Applied Sciences*, vol. 12, no. 3, 2022, ISSN: 2076-3417. DOI: 10.3390/app12031047.

[26] G. Messina and G. Modica, "Applications of uav thermal imagery in precision agriculture: State of the art and future research outlook," *Remote Sensing*, vol. 12, no. 9, 2020, ISSN: 2072-4292. DOI: 10.3390/rs12091491.

[27] M. F. Silva, A. C. Ribeiro, M. F. Santos, *et al.*, "Design of angular PID controllers for quadcopters built with low cost equipment," in *20th International Conference on System Theory, Control and Computing (ICSTCC)*, 2016, pp. 216–221. DOI: 10.1109/ICSTCC.2016.7790668.

[28] N. T. Hegde, V. I. George, and C. G. Nayak, "Modelling and transition flight control of vertical take-off and landing unmanned tri-tilting rotor aerial vehicle," in *2019 3rd International conference on Electronics, Communication and Aerospace Technology (ICECA)*, 2019, pp. 590–594. DOI: 10.1109/ICECA.2019.8821804.

[29] F. Mascagna Bittencourt Lima, "Controle de estabilização de voo de vants quadrirrotores: Modelagem, controle, simulação e prototipagem," *Unesp.br*, 2020.

[30] H. Zhang, L. Wang, T. Tian, and J. Yin, "A review of unmanned aerial vehicle low-altitude remote sensing (uav-lars) use in agricultural monitoring in china," *Remote Sensing*, vol. 13, no. 6, 2021, ISSN: 2072-4292. DOI: 10.3390/rs13061221.

[31] X. Liu, S. W. Chen, G. V. Nardari, *et al.*, "Challenges and opportunities for autonomous micro-uavs in precision agriculture," *IEEE Micro*, vol. 42, no. 1, pp. 61–68, 2022.

[32] G. O. Pimentel, M. F. Dos Santos, L. de Mello Honório, P. Mercorelli, M. F. Da Silva, and A. P. G. M. Moreira, "Design, modeling and control of an over-actuated hexacopter tilt-rotor," in *2023 24th International Carpathian Control Conference (ICCC)*, IEEE, 2023, pp. 315–320.

[33] R. I. Mukhamediev, K. Yakunin, M. Aubakirov, *et al.*, "Coverage path planning optimization of heterogeneous uavs group for precision agriculture," *IEEE Access*, vol. 11, pp. 5789–5803, 2023.

[34] P. Aela, H.-L. Chi, A. Fares, T. Zayed, and M. Kim, "Uav-based studies in railway infrastructure monitoring," *Automation in Construction*, vol. 167, p. 105 714, 2024.

[35] H.-W. Lee and C.-S. Lee, "Research on logistics of intelligent unmanned aerial vehicle integration system," *Journal of Industrial Information Integration*, vol. 36, p. 100 534, 2023.

[36] S. Yeom and I.-J. Cho, "Detection and tracking of moving pedestrians with a small unmanned aerial vehicle," *Applied Sciences*, vol. 9, no. 16, p. 3359, 2019.

[37] C. Xu, Q. Li, Q. Zhou, S. Zhang, D. Yu, and Y. Ma, "Power line-guided automatic electric transmission line inspection system," *IEEE Transactions on Instrumentation and Measurement*, vol. 71, pp. 1–18, 2022. DOI: 10.1109/TIM.2022.3169555.

[38] T. Calamoneri, F. Corò, and S. Mancini, "A realistic model to support rescue operations after an earthquake via uavs," *IEEE Access*, vol. 10, pp. 6109–6125, 2022. DOI: 10.1109/ACCESS.2022.3141216.

[39] T. F. Olivatto, F. F. Inguaggiato, and F. N. Stanganini, "Urban mapping and impacts assessment in a brazilian irregular settlement using uav-based imaging," *Remote Sensing Applications: Society and Environment*, vol. 29, p. 100 911, 2023.

[40] L. Gailler, P. Labazuy, E. Régis, *et al.*, "Validation of a new uav magnetic prospecting tool for volcano monitoring and geohazard assessment," *Remote Sensing*, vol. 13, no. 5, p. 894, 2021.

[41] N. Delavarpour, C. Koparan, J. Nowatzki, S. Bajwa, and X. Sun, "A technical study on uav characteristics for precision agriculture applications and associated practical challenges," *Remote Sensing*, vol. 13, no. 6, p. 1204, 2021.

[42] K. Phasinam, T. Kassanuk, P. P. Shinde, *et al.*, "Application of iot and cloud computing in automation of agriculture irrigation," *Journal of Food Quality*, vol. 2022, no. 1, p. 8 285 969, 2022.

[43] J. Lloret, S. Sendra, L. Garcia, and J. M. Jimenez, "A wireless sensor network deployment for soil moisture monitoring in precision agriculture," *Sensors*, vol. 21, no. 21, p. 7243, 2021.

[44] W. Arrubla-Hoyos, A. Ojeda-Beltrán, A. Solano-Barliza, *et al.*, "Precision agriculture and sensor systems applications in colombia through 5g networks," *Sensors*, vol. 22, no. 19, p. 7295, 2022.

[45] P. Sanjeevi, S. Prasanna, B. Siva Kumar, G. Gunasekaran, I. Alagiri, and R. Vijay Anand, "Precision agriculture and farming using internet of things based on wireless sensor network," *Transactions on Emerging Telecommunications Technologies*, vol. 31, no. 12, e3978, 2020.

[46] C. E. Hachimi, S. Belaqziz, S. Khabba, B. Sebbar, D. Dhiba, and A. Chehbouni, "Smart weather data management based on artificial intelligence and big data analytics for precision agriculture," *Agriculture*, vol. 13, no. 1, 2023, ISSN: 2077-0472. DOI: 10.3390/agriculture13010095.

[47] S. A. Lokhande, "Effective use of big data in precision agriculture," in *2021 International Conference on Emerging Smart Computing and Informatics (ESCI)*, 2021, pp. 312–316. DOI: 10.1109/ESCI50559.2021.9396813.

[48] M. Dakshayini and B. Balaji Prabhu, "An effective big data and blockchain (bd-bc) based decision support model for sustainable agriculture system," in *EAI International Conference on Big Data Innovation for Sustainable Cognitive Computing: BDCC 2018*, Springer, 2020, pp. 77–86.

[49] R. Sharma, S. S. Kamble, A. Gunasekaran, V. Kumar, and A. Kumar, "A systematic literature review on machine learning applications for sustainable agriculture supply chain performance," *Computers Operations Research*, vol. 119, p. 104 926, 2020, ISSN: 0305-0548. DOI: https://doi.org/10.1016/j.cor.2020.104926.

[50] A. Gümüşçü, M. E. Tenekeci, and A. V. Bilgili, "Estimation of wheat planting date using machine learning algorithms based on available climate data," *Sustainable Computing: Informatics and Systems*, vol. 28, p. 100 308, 2020.

[51] E. Raji, T. I. Ijomah, and O. G. Eyieyien, "Improving agricultural practices and productivity through extension services and innovative training programs," *International Journal of Applied Research in Social Sciences*, vol. 6, no. 7, pp. 1297–1309, 2024.

[52] Z. Zhang and L. Zhu, "A review on unmanned aerial vehicle remote sensing: Platforms, sensors, data processing methods, and applications," *Drones*, vol. 7, no. 6, 2023, ISSN: 2504-446X. DOI: 10.3390/drones7060398.

[53] L. Kouadio, M. El Jarroudi, Z. Belabess, *et al.*, "A review on uav-based applications for plant disease detection and monitoring," *Remote Sensing*, vol. 15, no. 17, 2023, ISSN: 2072-4292. DOI: 10.3390/rs15174273.

[54] F. Toscano, C. Fiorentino, N. Capece, *et al.*, "Unmanned aerial vehicle for precision agriculture: A review," *IEEE Access*, 2024.

[55] K. Zou, X. Chen, F. Zhang, H. Zhou, and C. Zhang, "A field weed density evaluation method based on uav imaging and modified u-net," *Remote Sensing*, vol. 13, no. 2, 2021, ISSN: 2072-4292. DOI: 10.3390/rs13020310.

[56] J. Meng and Z. Cheng, "Improving the estimation of soil-available nutrients at the sub-field scale using time-series uav observations," *Remote Sensing Letters*, vol. 11, no. 8, pp. 739–747, 2020. DOI: 10.1080/2150704X.2020.1763498.

[57] F. Kazemi and E. Ghanbari Parmehr, "Evaluation of rgb vegetation indices derived from uav images for rice crop growth monitoring," *ISPRS Annals of the Photogrammetry, Remote Sensing and Spatial Information Sciences*, vol. X-4/W1-2022, pp. 385–390, 2023. DOI: 10.5194/isprs-annals-X-4-W1-2022-385-2023.

[58] O. Apolo-Apolo, J. Martínez-Guanter, G. Egea, P. Raja, and M. Pérez-Ruiz, "Deep learning techniques for estimation of the yield and size of citrus fruits using a uav," *European Journal of Agronomy*, vol. 115, p. 126 030, 2020, ISSN: 1161-0301. DOI: https://doi.org/10.1016/j.eja.2020.126030.

[59] A. Feng, J. Zhou, E. D. Vories, K. A. Sudduth, and M. Zhang, "Yield estimation in cotton using uav-based multi-sensor imagery," *Biosystems Engineering*, vol. 193, pp. 101–114, 2020, ISSN: 1537-5110. DOI: https://doi.org/10.1016/j.biosystemseng.2020.02.014.

[60] X. Shi, Y. Du, X. Liu, *et al.*, "Optimizing uav spray parameters to improve precise control of tobacco pests at different growth stages," *Pest Management Science*, 2024.

[61] A. Guo, W. Huang, Y. Dong, *et al.*, "Wheat yellow rust detection using uav-based hyperspectral technology," *Remote Sensing*, vol. 13, no. 1, 2021, ISSN: 2072-4292. DOI: 10.3390/rs13010123.

[62] A. Risal, H. Niu, J. L. Landivar-Scott, *et al.*, "Improving irrigation management of cotton with small unmanned aerial vehicle (uav) in texas high plains," *Water*, vol. 16, no. 9, 2024, ISSN: 2073-4441. DOI: 10.3390/w16091300.

[63] A. Kumar, S. S, T. N, *et al.*, "Identification of water-stressed area in maize crop using uav based remote sensing," in *2020 IEEE India Geoscience and Remote*

Sensing Symposium (InGARSS), 2020, pp. 146–149. DOI: 10.1109/InGARSS48198.2020.9358930.

[64] J. Wang, C. Ma, P. Chen, *et al.*, "Evaluation of aerial spraying application of multi-rotor unmanned aerial vehicle for areca catechu protection," *Frontiers in Plant Science*, vol. 14, p. 1 093 912, 2023.

[65] B. U. Meinen and D. T. Robinson, "Mapping erosion and deposition in an agricultural landscape: Optimization of uav image acquisition schemes for sfm-mvs," *Remote Sensing of Environment*, vol. 239, p. 111 666, 2020.

[66] F. López-Granados, J. Torres-Sánchez, F. M. Jiménez-Brenes, *et al.*, "Monitoring vineyard canopy management operations using uav-acquired photogrammetric point clouds," *Remote Sensing*, vol. 12, no. 14, 2020, ISSN: 2072-4292. DOI: 10.3390/rs12142331. [Online]. Available: https://www.mdpi.com/2072-4292/12/14/2331.

[67] M. V. Ferro, C. G. Sørensen, and P. Catania, "Comparison of different computer vision methods for vineyard canopy detection using uav multispectral images," *Computers and Electronics in Agriculture*, vol. 225, p. 109 277, 2024, ISSN: 0168-1699. DOI: https://doi.org/10.1016/j.compag.2024.109277. [Online]. Available: https://www.sciencedirect.com/science/article/pii/S0168169924006689.

[68] L. Pádua, A. Matese, S. F. Di Gennaro, R. Morais, E. Peres, and J. J. Sousa, "Vineyard classification using obia on uav-based rgb and multispectral data: A case study in different wine regions," *Computers and Electronics in Agriculture*, vol. 196, p. 106 905, 2022, ISSN: 0168-1699. DOI: https://doi.org/10.1016/j.compag.2022.106905. [Online]. Available: https://www.sciencedirect.com/science/article/pii/S0168169922002228.

[69] P. K. Reddy Maddikunta, S. Hakak, M. Alazab, *et al.*, "Unmanned aerial vehicles in smart agriculture: Applications, requirements, and challenges," *IEEE Sensors Journal*, vol. 21, no. 16, pp. 17 608–17 619, 2021. DOI: 10.1109/JSEN.2021.3049471.

[70] S. YI, "Modeling and control of an over-actuated quadrotor manipulator with four tiltable rotors," *Okayama University*, 2022.

[71] M. F. Santos, L. M. Honório, A. P. G. M. Moreira, M. F. Silva, and V. F. Vidal, "Fast real-time control allocation applied to over-actuated quadrotor tilt-rotor," *Journal of Intelligent & Robotic Systems*, 2021, ISSN: 1573-0409. DOI: https://doi.org/10.1007/s10846-021-01411-4.

[72] X. Li, J. Wei, W. Chen, *et al.*, "A novel overactuated tricopter unmanned aerial vehicle: Modeling, control and validation," in *2024 43rd Chinese Control Conference (CCC)*, 2024, pp. 4784–4789. DOI: 10.23919/CCC63176.2024.10661662.

[73] Y. Wang, Z. Zhu, and Y. Zhang, "Modeling and control of a novel over-actuated tri-rotor uav," in *2020 International Conference on Unmanned Aircraft Systems (ICUAS)*, 2020, pp. 329–338. DOI: 10.1109/ICUAS48674.2020.9213976.

[74] A. K. Gavgani, A. Talaeizadeh, S. Heidarzadeh, A. Alasty, and H. Nejat Pishkenari, "Dynamic modeling and sliding mode control of an over-actuated quadrotor with variable hedral angle of propeller axes," in *2024 2nd International Conference on Unmanned Vehicle Systems-Oman (UVS)*, 2024, pp. 1–6. DOI: 10.1109/UVS59630.2024.10467169.

[75] B. Wang and Y. Zhang, "Adaptive fault-tolerant control allocation of an over-actuated hybrid fixed-wing uav," in *AIAA SCITECH 2022 Forum*, 2022, p. 2079.

[76] E. Enenakpogbe, J. F. Whidborne, and L. Lu, "Control of an over-actuated fixed-wing vectored thrust evtol," in *2024 UKACC 14th International Conference on Control (CONTROL)*, 2024, pp. 315–316. DOI: 10.1109/CONTROL60310.2024.10531934.

[77] M. HajiAbedini, F. Zargarbashi, A. Talaeizadeh, H. N. Pishkenari, and A. Alasty, "Design and implementation of a novel over-actuated quadrotor with variable dihedral angle," in *2021 9th RSI International Conference on Robotics and Mechatronics (ICRoM)*, 2021, pp. 391–398. DOI: 10.1109/ICRoM54204.2021.9663479.

[78] H. Zhou, B. Li, D. Wang, and L. Ma, "Design, modeling and control of a novel over-actuated hexacopter with tiltable rotors," in *2021 IEEE 16th Conference on Industrial Electronics and Applications (ICIEA)*, 2021, pp. 1079–1084. DOI: 10.1109/ICIEA51954.2021.9516039.

[79] R. Bagadiaa, "Exploratory design and control of an over-actuated drone," M.S. thesis, EECS Department, University of California, Berkeley, Aug. 2023. [Online]. Available: http://www2.eecs.berkeley.edu/Pubs/TechRpts/2023/EECS-2023-217.html.

[80] Z. Ge, F. Liu, and L. Meng, "Adaptive pid control for second order nonlinear systems," in *2020 Chinese Control And Decision Conference (CCDC)*, 2020, pp. 2926–2931. DOI: 10.1109/CCDC49329.2020.9164463.

[81] S. Srey and S. Srang, "Adaptive controller based on estimated parameters for quadcopter trajectory tracking.," *International Journal of Robotics & Control Systems*, vol. 4, no. 2, 2024.

[82] S. N. Yaşar and E. Karaköse, "Trajectory control of quadcopter in matlab simulation environment," in *2022 International Conference on Decision Aid Sciences and Applications (DASA)*, 2022, pp. 1127–1131. DOI: 10.1109/DASA54658.2022.9765119.

[83] M. N. Rajan, G. Velmurugan, N. B. N, and A. V, "Design and testing of a hexacopter sprayer for controlled deforestation and pest control," in *2023 4th International Conference on Smart Electronics and Communication (ICOSEC)*, 2023, pp. 50–56. DOI: 10.1109/ICOSEC58147.2023.10276107.

[84] M. A. M. Basri *et al.*, "Trajectory tracking of a quadcopter uav using pid controller," *ELEKTRIKA-Journal of Electrical Engineering*, vol. 22, no. 2, pp. 14–21, 2023.

[85] K. Hong, "Simulation and analysis of stability of uav control system based on pid control under different wind forces," in *Journal of Physics: Conference Series*, IOP Publishing, vol. 2649, 2023, p. 012 011.

[86] T. H. Chiew, H.-E. Lee, Y. K. Lee, K. M. Chang, J. J. Ong, and K. S. Eu, "Second order sliding mode controller for altitude and yaw control of quadcopter," in *2021 11th IEEE International Conference on Control System, Computing and Engineering (ICCSCE)*, IEEE, 2021, pp. 97–102.

[87] J. Pan, B. Shao, J. Xiong, and Q. Zhang, "Attitude control of quadrotor uavs based on adaptive sliding mode," *International Journal of Control, Automation and Systems*, vol. 21, no. 8, pp. 2698–2707, 2023.

[88] Y. Xi, H. Huang, Z. Tian, and G. He, "Design of transition mode attitude controller for a tilt-rotor uav based on mpc method," in *2021 40th Chinese Control Conference (CCC)*, 2021, pp. 7797–7802. DOI: 10.23919/CCC52363.2021.9549971.

[89] W. Jung and H. Bang, "Fault and failure tolerant model predictive control of quadrotor uav," *International Journal of Aeronautical and Space Sciences*, vol. 22, pp. 663–675, 2021.

[90] A. J. Al-Mahasneh, S. G. Anavatti, M. Ferdaus, and M. A. Garratt, "Adaptive neural altitude control and attitude stabilization of a hexacopter with uncertain dynamics," in *2019 IEEE International Conference on Industry 4.0, Artificial Intelligence, and Communications Technology (IAICT)*, IEEE, 2019, pp. 44–49.

[91] P. Burggräf, A. R. Pérez Martínez, H. Roth, and J. Wagner, "Quadrotors in factory applications: Design and implementation of the quadrotor's p-pid cascade control system: Modeling and implementation," *SN Applied Sciences*, vol. 1, no. 7, p. 722, 2019.

[92] N. P. Nguyen, N. X. Mung, H. L. N. N. Thanh, T. T. Huynh, N. T. Lam, and S. K. Hong, "Adaptive sliding mode control for attitude and altitude system of a

quadcopter uav via neural network," *IEEE Access*, vol. 9, pp. 40 076–40 085, 2021. DOI: 10.1109/ACCESS.2021.3064883.

[93] A. A. Najm, A. T. Azar, I. K. Ibraheem, and A. J. Humaidi, "A nonlinear pid controller design for 6-dof unmanned aerial vehicles," in *Unmanned Aerial Systems*, Elsevier, 2021, pp. 315–343.

[94] J. Zhang, Z. Ren, C. Deng, and B. Wen, "Adaptive fuzzy global sliding mode control for trajectory tracking of quadrotor uavs," *Nonlinear Dynamics*, vol. 97, pp. 609–627, 2019.

[95] S. Ullah, A. Mehmood, Q. Khan, S. Rehman, and J. Iqbal, "Robust integral sliding mode control design for stability enhancement of under-actuated quadcopter," *International Journal of Control, Automation and Systems*, vol. 18, pp. 1671–1678, 2020.

[96] C. Sun, S. A. Agha, Z. Mohamed, and M. H. Shaheed, "Optimised sliding mode control of a hexacopter: Simulation and experiments," *Electronics*, vol. 11, no. 16, p. 2519, 2022.

[97] ROS.org. [Online]. Available: https://wiki.ros.org/ROS/Introduction.

[98] J. Gustave, J. Chahal, and A. Belbachir, "Functional architecture using ros for autonomous uavs.," in *ICINCO*, 2020, pp. 506–512.

[99] ROS.org. [Online]. Available: https://wiki.ros.org/ROS/Concepts.

[100] R. 2. [Online]. Available: https://docs.ros.org/en/rolling/index.html.

[101] T. Indriyanto, A. Rizki, M. Hariyadin, M. Akbar, and A. Syafi, "Centralized swarming uav using ros for collaborative missions," in *AIP conference proceedings*, AIP Publishing, vol. 2226, 2020.

[102] G. Stavrinos, "Landing an autonomous uav on a moving platform using only a front facing camera," *Robot Operating System (ROS) The Complete Reference (Volume 5)*, pp. 157–183, 2021.

[103] J. Cacace, N. Mimmo, and L. Marconi, "An arva sensor simulator," *Robot Operating System (ROS) The Complete Reference (Volume 5)*, pp. 233–266, 2021.

[104] A. Antonopoulos, M. G. Lagoudakis, and P. Partsinevelos, "A ros multi-tier uav localization module based on gnss, inertial and visual-depth data," *Drones*, vol. 6, no. 6, p. 135, 2022.

[105] Y. Yang, W. Meng, and S. Zhu, "A digital twin simulation platform for multi-rotor uav," in *2020 7th International Conference on Information, Cybernetics, and Computational Social Systems (ICCSS)*, 2020, pp. 591–596. DOI: 10.1109/ICCSS52145.2020.9336872.

[106] E. Moréac, E. M. Abdali, F. Berry, D. Heller, and J.-P. Diguet, "Hardware-in-the-loop simulation with dynamic partial fpga reconfiguration applied to computer vision in ros-based uav," in *2020 International Workshop on Rapid System Prototyping (RSP)*, 2020, pp. 1–7. DOI: 10.1109/RSP51120.2020.9244863.

[107] A. Farley, J. Wang, and J. A. Marshall, "How to pick a mobile robot simulator: A quantitative comparison of coppeliasim, gazebo, morse and webots with a focus on accuracy of motion," *Simulation Modelling Practice and Theory*, vol. 120, p. 102 629, 2022, ISSN: 1569-190X. DOI: https://doi.org/10.1016/j.simpat.2022.102629.

[108] X-Plane. [Online]. Available: https://www.x-plane.com/.

[109] M. F. Simulator. [Online]. Available: https://www.flightsimulator.com/.

[110] Webots. [Online]. Available: https://cyberbotics.com/.

[111] U. 3D. [Online]. Available: unity.com.

[112] AirSim. [Online]. Available: https://microsoft.github.io/AirSim/.

[113] Morse. [Online]. Available: https://morse-simulator.github.io/.

[114] J. Collins, S. Chand, A. Vanderkop, and D. Howard, "A review of physics simulators for robotic applications," *IEEE Access*, vol. 9, pp. 51 416–51 431, 2021. DOI: 10.1109/ACCESS.2021.3068769.

[115] Gazebo. [Online]. Available: https://gazebosim.org/home.

[116] A. Zenkin, I. Berman, K. Pachkouski, I. Pantiukhin, and V. Rzhevskiy, "Quadcopter simulation model for research of monitoring tasks," in *2020 26th Conference of Open Innovations Association (FRUCT)*, 2020, pp. 449–457. DOI: 10.23919/FRUCT48808.2020.9087391.

[117] N. Nair, K. Sareth, R. R. Bhavani, and A. Mohan, "Simulation and stabilization of a custom-made quadcopter in gazebo using ardupilot and qgroundcontrol," in *Modeling, Simulation and Optimization: Proceedings of CoMSO 2021*, Springer, 2022, pp. 191–202.

[118] R. K. Megalingam, D. V. Prithvi, N. C. S. Kumar, and V. Egumadiri, "Drone stability simulation using ros and gazebo," in *Advanced Computing and Intelligent Technologies: Proceedings of ICACIT 2021*, Springer, 2022, pp. 131–143.

[119] F. C. S. Xavier, S. R. B. d. Santos, and S. N. Givigi, "Multifixed-wing-uav software-in-the-loop simulation platform for system design," *IEEE Systems Journal*, vol. 17, no. 4, pp. 6724–6735, 2023. DOI: 10.1109/JSYST.2023.3326991.

[120] C. Ma, Y. Zhou, and Z. Li, "A new simulation environment based on airsim, ros, and px4 for quadcopter aircrafts," in *2020 6th International Conference on Control, Automation and Robotics (ICCAR)*, 2020, pp. 486–490. DOI: 10.1109/ICCAR49639.2020.9108103.

[121] PX4. [Online]. Available: https://docs.px4.io/main/en/.

[122] Y. Jing, X. Wang, J. Heredia-Juesas, *et al.*, "Px4 simulation results of a quadcopter with a disturbance-observer-based and pso-optimized sliding mode surface controller," *Drones*, vol. 6, no. 9, 2022, ISSN: 2504-446X. DOI: 10.3390/drones6090261. [Online]. Available: https://www.mdpi.com/2504-446X/6/9/261.

[123] V. Gomez, N. Gomez, J. Rodas, E. Paiva, M. Saad, and R. Gregor, "Pareto optimal pid tuning for px4-based unmanned aerial vehicles by using a multi-objective particle swarm optimization algorithm," *Aerospace*, vol. 7, no. 6, 2020, ISSN: 2226-4310. DOI: 10.3390/aerospace7060071. [Online]. Available: https://www.mdpi.com/2226-4310/7/6/71.

[124] R. Lozano, *Unmanned aerial vehicles: Embedded control*. John Wiley & Sons, 2013.

[125] R. Beard and T. McLain, *Small Unmanned Aircraft: Theory and Practice*. Princeton University Press, 2012, ISBN: 9781400840601.

[126] M. F. d. Santos, "Controle tolerante a falhas de um sistema de propulsão de hexacópteros," 2014.

[127] B. L. Stevens, F. L. Lewis, and E. N. Johnson, *Aircraft control and simulation: dynamics, controls design, and autonomous systems*. John Wiley & Sons, 2015.

[128] G. J. Ducard, *Fault-tolerant flight control and guidance systems: Practical methods for small unmanned aerial vehicles*. Springer Science & Business Media, 2009.

[129] M. F. d. Santos, "Alocação de controle desacoplada rápida em sistemas de controle superatuados," 2020.

[130] N. K. Sinha and N. Ananthkrishnan, *Advanced flight dynamics with elements of flight control*. CRC Press, 2017.

[131] J. Gao, Q. Zhang, J. Chen, and X. Wang, "Take-off trajectory optimization of tilt-rotor aircraft based on direct allocation method," in *IOP Conference Series: Materials Science and Engineering*, IOP Publishing, vol. 768, 2020, p. 042 004.

[132] A. Ahani and M. J. Ketabdari, "Alternative approach for dynamic-positioning thrust allocation using linear pseudo-inverse model," *Applied Ocean Research*, vol. 90, p. 101 854, 2019.

[133] A. K. Venkitaraman and V. S. R. Kosuru, "Electric vehicle charging network optimization using multi-variable linear programming and bayesian principles," in *2022 Third International Conference on Smart Technologies in Computing, Electrical and Electronics (ICSTCEE)*, 2022, pp. 1–5. DOI: 10.1109/ICSTCEE56972.2022.10099649.

[134] Y. Li, Q. Zhu, and A. Elahi, "Sequential convex programming for nonlinear optimal control in uav trajectory planning," *Algorithms*, vol. 17, no. 7, p. 304, 2024.

[135] M. Santos, L. Honório, A. P. G. M. Moreira, P. A. N. Garcia, M. Silva, and V. F. Vidal, "Analysis of a fast control allocation approach for nonlinear over-actuated systems," *ISA transactions*, vol. 126, pp. 545–561, 2022.

[136] M. F. da Silva, L. M. Honorio, A. L. M. Marcato, V. F. Vidal, and M. F. Santos, "Unmanned aerial vehicle for transmission line inspection using an extended kalman filter with colored electromagnetic interference," vol. 100, 2020, pp. 322–333. DOI: https://doi.org/10.1016/j.isatra.2019.11.007.

[137] K. Ogata, *Engenharia de Controle Moderno*. Pearson Universidades, 2010, ISBN: 9788576058106.

[138] S. I. Abdelmaksoud, M. Mailah, and A. M. Abdallah, "Improving disturbance rejection capability for a quadcopter uav system using self-regulating fuzzy pid controller," in *2020 international conference on computer, control, electrical, and electronics engineering (ICCCEEE)*, IEEE, 2021, pp. 1–6.

[139] D. Kingston and R. Beard, "Uav splay state configuration for moving targets in wind," in *Advances in Cooperative Control and Optimization: Proceedings of the 7th International Conference on Cooperative Control and Optimization*, Springer, 2007, pp. 109–128.

[140] MAVLink. [Online]. Available: https://mavlink.io/en/.